SEARCHING FOR ULTRALIGHT DARK MATTER WITH MECHANICAL SENSORS

by

Jack Manley

A dissertation submitted to the Faculty of the University of Delaware in partial fulfillment of the requirements for the degree of Doctor of Philosophy in Electrical and Computer Engineering

Summer 2022

SEARCHING FOR ULTRALIGHT DARK MATTER WITH MECHANICAL SENSORS

by

Jack Manley

Approved: _____

Jamie D. Phillips, Ph.D.
Chair of the Department of Electrical and Computer Engineering

Approved: _____

Levi T. Thompson, Ph.D.
Dean of the College of Engineering

Approved: _____

Louis F. Rossi, Ph.D.
Vice Provost for Graduate and Professional Education and
Dean of the Graduate College

I certify that I have read this dissertation and that in my opinion it meets the academic and professional standard required by the University as a dissertation for the degree of Doctor of Philosophy.

Signed: _____

Swati Singh, Ph.D.
Professor in charge of dissertation

I certify that I have read this dissertation and that in my opinion it meets the academic and professional standard required by the University as a dissertation for the degree of Doctor of Philosophy.

Signed: _____

Matthew Doty, Ph.D.
Member of dissertation committee

I certify that I have read this dissertation and that in my opinion it meets the academic and professional standard required by the University as a dissertation for the degree of Doctor of Philosophy.

Signed: _____

Dennis W. Prather, Ph.D.
Member of dissertation committee

I certify that I have read this dissertation and that in my opinion it meets the academic and professional standard required by the University as a dissertation for the degree of Doctor of Philosophy.

Signed: _____

Daniel Grin, Ph.D.
Member of dissertation committee

ACKNOWLEDGEMENTS

I thank Dr. Swati Singh for providing funding and guidance throughout my time as a PhD student. I am particularly grateful for the opportunities Dr. Singh has given me to present at conferences and collaborate with researchers from different fields. This dissertation could not have been completed without Dr. Singh's ideas and work.

For reviewing this dissertation, I thank the members of my dissertation committee, Dr. Swati Singh, Dr. Matthew Doty, Dr. Dennis Prather, and Dr. Daniel Grin. For additional proofreading and feedback, I thank Dr. Swati Singh, Dr. Dawn Manley, Dr. James Manley, Dr. Matt Konkol, Nick Dow, Joey Betz, Matt Myers, Josh Gable, Dr. Andy Mercante, Tyler McCarthy, Steve Petfield, Tori Carey, and John Goldman.

I thank Dr. Dennis Prather for funding and advising my first year of graduate school. For help and guidance during my first year I thank Dr. Andy Mercante, Dr. Mat Zablocki, Dr. Abu Naim Rakib Ahmed, Dr. Shouyuan Shi, Dr. Peng Yao, Tori Carey, Dr. Matt Konkol, Josh Johnson, and Chris Cullen.

For their work on the papers that form the basis of this dissertation, I thank Mitul Dey Chowdhury, Dr. Dalziel Wilson, Dr. Daniel Grin, Dr. Swati Singh, Russ Stump, and Ryan Petery. I additionally thank collaborators on other projects, Joey Betz, Marvin Hirschel, Dr. Abu Naim Rakib Ahmed, and Dr. John P Davis.

Special thanks to Dr. Dominic Di Toro, who has mentored me since before grad school and given me invaluable advice over the years. I additionally thank Dr. Matt Konkol for his advice and support.

I thank Dr. James Manley and Dr. Dawn Manley for helping me rehearse every presentation I have given during my time as a PhD student.

TABLE OF CONTENTS

Appendix

LIST OF TABLES

LIST OF FIGURES

ABSTRACT

The purpose of this dissertation is to assess the ability of tabletop devices, primarily based on mechanical systems, to serve as detectors for ultralight dark matter.

Dark matter accounts for 85% of the matter in the Universe, yet its composition is unknown. One possibility is that dark matter is composed of ultralight particles with mass less than 10 eV/c^2 ($\sim 10^{-35}$ kg), forming a coherent field. The ultralight dark matter field's non-gravitational interactions with normal matter would produce a weak, yet persistent, narrowband signal at an unknown frequency. This dissertation considers scenarios where dark matter is composed of novel spin 1 (vector) or spin 0 (scalar) particles whose interactions with normal matter result in measurable mechanical effects such as a strain or acceleration. Several prospective tabletop detectors are proposed, providing an avenue for small-scale experiments to contribute to the search for dark matter.

First, various optomechanical resonators are proposed as detectors for ultralight dark matter. Specifically, silicon nitride optomechanical membranes are considered to search for vector ultralight dark matter, and several compact mechanical resonators composed of high quality materials (superfluid and crystalline solids) are considered to search for scalar ultralight dark matter. Through a combination of low mechanical dissipation, cryogenic cooling, and cavity-enhanced optical readout, it is found that optomechanical resonators are capable of performing dark matter searches in the Hz-MHz frequency range, corresponding to particles of mass $10^{-12} - 10^{-6}$ eV/c^2.

As a broadband and low-frequency supplement to optomechanical resonators, whose mechanical resonances have limited bandwidth, an optical fiber-based detector is proposed to perform a broadband search for scalar ultralight dark matter. A case is made that, given sufficient cryogenic cooling and acoustic isolation, optical fiber-based detectors can be used to search for ultralight dark matter at sub-Hz frequencies $\left(10^{-17}\text{ - }10^{-13}\text{ eV}/c^2\right)$.

Chapter 1

INTRODUCTION TO ULTRALIGHT DARK MATTER (UDM)

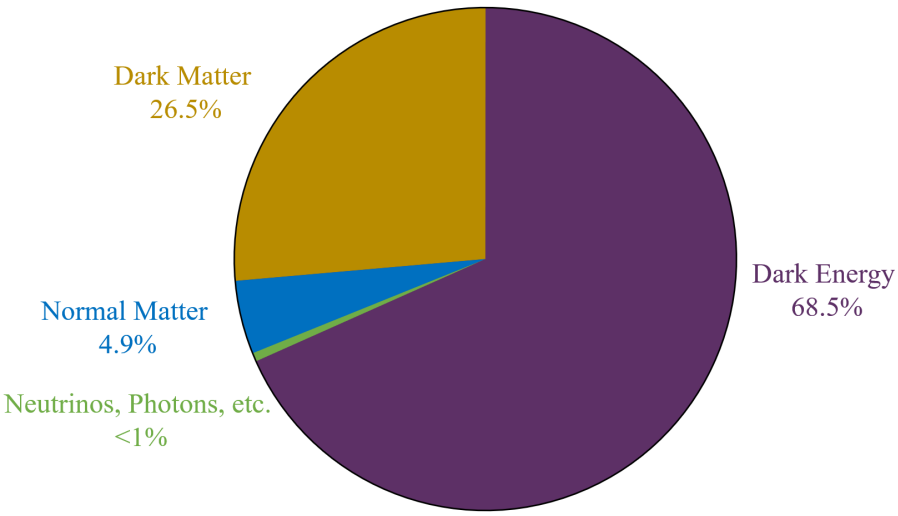

Figure 1.1: Energy budget of the Universe: Normal matter accounts for only 5% of the energy in the Universe, while 27% is dark matter. Percentages from Ref. [3].

1.1 Dark matter (DM)

Five percent of the energy-matter composition of the Universe comes from normal matter. The rest of the Universe's energy budget is attributed to dark energy (68%) and dark matter (27%) [3]. The Standard Model of particle physics can only sufficiently explain normal matter, meaning that 95% of the Universe is poorly understood by the scientific community.

This dissertation is concerned with the detection of dark matter (DM), which accounts for 85% of the *matter* in the Universe. Some of the earliest evidence for dark matter comes from measurements of the rotation curves of galaxies [49] and galaxy clusters [50], and it is

now understood that dark matter forms the dominant component of galaxies,[1] including the Milky Way.

The name "dark matter" describes almost everything that is known about it: dark matter is matter, and it doesn't interact (or interacts only very weakly) with light. Dark matter has mass and interacts gravitationally with normal matter and itself. Observations of dark matter's gravitational effects can be used to determine the quantity (e.g. via measurements of strong gravitational lensing [52]) and distribution (e.g. via measurements of weak gravitational lensing [53]) within galaxies or galaxy clusters. It is also worth noting that dark matter theory is consistent with additional astrophysical and cosmological observations [54, 55], such as measurements of anisotropy in the Cosmic Microwave Background [51].

The spatial distribution of dark matter within the Milky Way is typically estimated with the Standard Halo Model,[2] which assumes dark matter to form a gravitationally-stable and spherically-symmetric density profile that decreases with distance from the center of the galaxy $\rho_{\rm DM}(r) \propto r^{-2}$[3]. In the Solar Neighborhood, the local dark matter energy density (averaged over hundreds of parsecs) is estimated to be $\rho_{\rm DM} \approx 0.4\ {\rm GeV/cm^3}$ [57]. Dark matter is approximated as a collisionless gas [56], resulting in a Maxwellian velocity $\boldsymbol{v}$ distribution given by

$$f_{\boldsymbol{v}} \propto e^{-\boldsymbol{v}\cdot\boldsymbol{v}/2{\Delta v_{\rm DM}}^2} \tag{1.1}$$

below the escape velocity ($\sim 530\ {\rm km\ s^{-1}}$) in the Galactic frame, where $\Delta v_{\rm DM} \approx 10^{-3}c$ is the velocity dispersion [58].

---

[1] Dark energy is spread relatively uniformly throughout the Universe with an energy density of $\sim 10^3\ {\rm eV/cm^3}$ [51], while DM is concentrated within galaxies and galaxy clusters. So dark energy is much less dense than DM within galaxies. For example, the DM density in the vicinity of Earth is $\sim 10^8\ {\rm eV/cm^3}$ [3]

[2] While this simple model for DM is commonly used for analyzing data from direct detection experiments, it is worth mentioning that the DM halo likely has not reached equilibrium and contains additional substructure that would affect the local DM density and velocity distribution [56].

1.2 DM Candidates

Despite the observational evidence for DM, its composition remains a mystery. It could consist of composite or elementary particles, which may be fermions or bosons. Dark matter may be entirely composed of a single particle species, or there may be more than one type of DM particle, as is the case with normal matter. It is also unknown if DM has any non-gravitational interactions with normal matter.

The observations supporting the existence of DM mentioned in Section 1.1 may be considered *indirect* measurements of DM, because DM's existence is inferred through the (gravitational) effects it has on other astrophysical objects being observed. This dissertation is concerned with designing *direct* detection experiments, where DM interacts directly with the detector in the laboratory. Direct detection experiments are often intended to search for DM's non-gravitational interactions, which are not known. Therefore, designing a direct detection experiment typically requires additional assumptions about DM particles and their interactions with normal matter.[3] These assumptions clarify what type of signal to search for, making it possible to design an experiment.

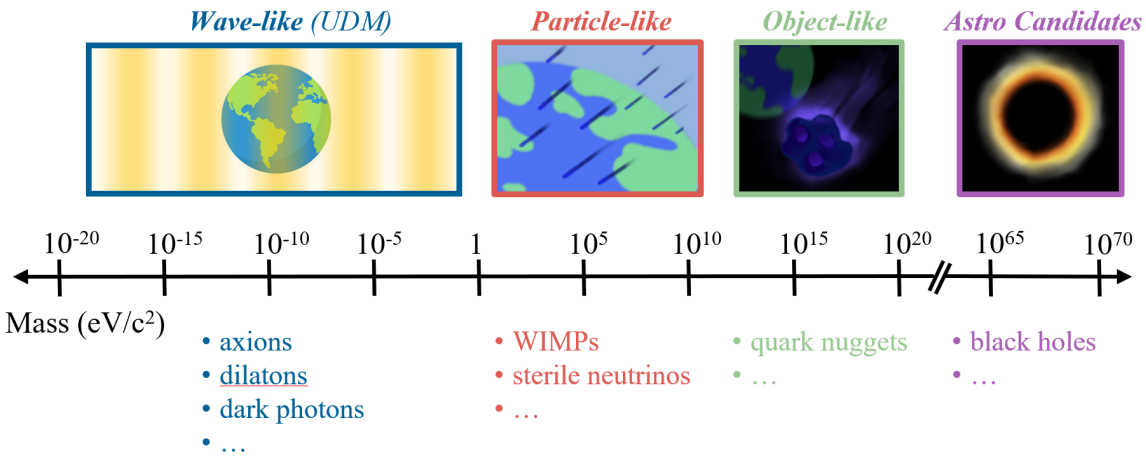

Figure 1.2: DM candidates, sorted by mass: This dissertation is primarily concerned with "wave-like" (ultralight) dark matter. *Note:* 1 eV/c^2 $\approx$ 10^{-36} kg. Image credit: Swati Singh.

[3] It is worth noting that some DM candidates can potentially be detected through a direct gravitational interaction [59].

Because DM has not yet been directly detected, there remains a lot of uncertainty surrounding the composition of DM. Figure 1.2 includes some of the possibilities that have been considered, roughly grouped by particle/object mass. Viable candidates span 90 orders of magnitude in mass, including novel elementary and composite particles as well as heavy objects such as black holes [60]. As a starting point, initial searches have focused on hypothetical new particles whose existence would also solve other open problems in physics. For example, a popular DM candidate is the weakly interacting massive particle (WIMP), which arises in supersymmetric extensions of the Standard Model [3].

Many experiments have been designed to search for WIMPs with particle masses in the GeV/c^2 range [61, 62] using large detectors in low-noise environments to attain high sensitivity to collisions between individual DM particles and target atoms. The absence of direct evidence for DM from these searches has motivated a new generation of detection schemes that broaden the search to a greater variety of candidates, such as ultralight dark matter (UDM) (particles with mass $m_{\mathrm{DM}} \lesssim 10$ eV/c^2). In particular, the quantum chromodynamics axion is a popular candidate for UDM, as its existence would provide a solution to the strong charge-parity problem [63]. However, this dissertation is concerned with scalar (spin-0) and vector (spin-1) UDM candidates, such as dilatons and dark photons [5].

1.3 Properties of UDM

Ultralight particles are distinguished from heavier DM candidates, because UDM forms a coherent field that fills the galaxy. The direct-detection signature of heavier DM candidates such as WIMPs would be transient, due to a random recoil event with the detector. The UDM field, however, is always present in the laboratory, and it would likely produce a coherent signal. The properties of the UDM field are discussed in this section and a brief introduction is given for the different possible UDM signals and the detectors being used to search for them.

1.3.1 Particle mass range

Ultralight dark matter is a class of DM candidates defined by having a particle mass $m_{\mathrm{DM}} \lesssim 10\ \mathrm{eV/c^2}$ [64]. Astrophysical measurements impose a lower bound of $\sim 10^{-22}\ \mathrm{eV}/c^2$ on the particle mass, below which the de Broglie wavelength would be long enough to affect large-scale structure formation [40].

Dark matter particles with $m_{\mathrm{DM}} \lesssim 10\ \mathrm{eV/c^2}$ would have a de Broglie wavelength of $\lambda_{\mathrm{DM}} = h/(m_{\mathrm{DM}} v_{\mathrm{DM}}) \gtrsim 1\,\mathrm{mm}$,[4] so there would be more than 10^6 DM particles within a de Broglie volume $(\lambda_{\mathrm{DM}})^3$, given the local DM energy density $\rho_{\mathrm{DM}} \approx 0.4\ \mathrm{GeV/cm^3}$. The particle wavelength greatly exceeds the inter-particle separation, meaning that UDM is better modeled as a classical field than individual particles. Additionally, the large mode occupation number implies that UDM particles are bosonic (integer spin) [64].

1.3.2 UDM field

Because dark matter does not interact strongly with normal matter, it can be modeled within the Solar Neighborhood simply as a field in vacuum, resulting in plane wave solutions, which will be discussed in more detail in Chapter 2:[5]

$$\varphi(t, \boldsymbol{r}) = \varphi_0 \cos\left(\omega t - \boldsymbol{k} \cdot \boldsymbol{r} + \theta\right). \tag{1.2}$$

As explained in more detail in Chapter 2, ω is the Doppler-shifted angular Compton frequency[6] and $\boldsymbol{k}^2 = \left(\frac{2\pi}{\lambda_{\mathrm{DM}}}\right)^2$, where λ_{DM} is the de Broglie wavelength. For the particle mass ranges considered in this dissertation $\left(10^{-17}\ \mathrm{eV} \lesssim m_{\mathrm{DM}} \lesssim 10^{-6}\ \mathrm{eV}\right)$, the de Broglie wavelength $\left(10^{14}\ \mathrm{m} \gtrsim \lambda_{\mathrm{DM}} \gtrsim 10^{3}\ \mathrm{m}\right)$ would greatly exceed the length span of the proposed experiments. So, as is the case for most terrestrial experiments, the field is considered spatially

[4] The average speed of DM particles in the Solar Neighborhood is approximately equal to the velocity dispersion $v_{\mathrm{DM}} \approx 10^{-3} c$.

[5] For simplicity, UDM is expressed as a scalar field φ, but similar analyses apply to all types of UDM.

[6] The angular Compton frequency is $\omega_{\mathrm{DM}} = m_{\mathrm{DM}} c^2/\hbar$. For particles with non-relativistic speed v_{DM}, the Doppler-shifted angular Compton frequency is $\omega = \omega_{\mathrm{DM}}\left(1 + \frac{1}{2}\frac{{v_{\mathrm{DM}}}^2}{c^2}\right)$

uniform within the laboratory. The field amplitude depends on the local dark matter density, $\varphi_0 \propto \sqrt{\rho_{\rm DM}}$, and the phase θ is unknown.

Figure 1.3: Visualization of the UDM field: The magnitude of the UDM field is displayed in yellow, for a single plane wave solution (Eq. 1.2). The field is nearly monochromatic and it is effectively spatially uniform on laboratory length scales.

As discussed in Section 1.1, dark matter particles do not all have the same velocity. The local speed distribution translates to a frequency distribution via Doppler shifting, resulting in a UDM spectral density with a fractional linewidth of $\frac{\Delta\omega_{\rm DM}}{\omega_{\rm DM}} \approx (\Delta v_{\rm DM}/c)^2 \approx 10^{-6}$ [4] (Fig. 1.4).

To account for the UDM lineshape, the field can be modeled as a superposition of the plane wave solutions [43] (treated as spatially uniform)

$$\varphi(t) = \varphi_0 \sum_i A_i \cos\left(\omega_i t + \theta_i\right), \tag{1.3}$$

where A_i is the amplitude of each frequency component. The frequency distribution of the UDM field is displayed in Fig. 1.4. The phase of each frequency component is considered random; i.e. θ_i is a random variable with a flat distribution from 0 to 2π [43]. The result of this summation is a quasi-monochromatic field, with a coherence time of [4]

$$\tau_{\rm DM} \approx {\Delta\omega_{\rm DM}}^{-1} = \left(\frac{{\Delta v_{\rm DM}}^2}{c^2}\omega_{\rm DM}\right)^{-1} \approx 10^6 \omega_{\rm DM}. \tag{1.4}$$

On timescales less than the coherence time $\tau_{\rm DM}$, the field can be treated as monochromatic, oscillating at the angular Compton frequency $\omega_{\rm DM}$,

$$\varphi(t) \approx \varphi_0 \cos\left(\omega_{\rm DM} t + \theta_{\rm DM}\right), \tag{1.5}$$

with a random phase $\theta_{\rm DM}$. The amplitude φ_0 would be a stochastic variable with a Rayleigh distribution [65],

$$p(\varphi_0) = \frac{2\varphi_0}{{\varphi_{\rm rms}}^2} \exp\left(-\frac{{\varphi_0}^2}{{\varphi_{\rm rms}}^2}\right), \tag{1.6}$$

with a root-mean-square value determined by the local dark matter density $\varphi_{\rm rms} = \sqrt{\frac{8\pi G \rho_{\rm DM}}{c^2 {\omega_{\rm DM}}^2}}$.

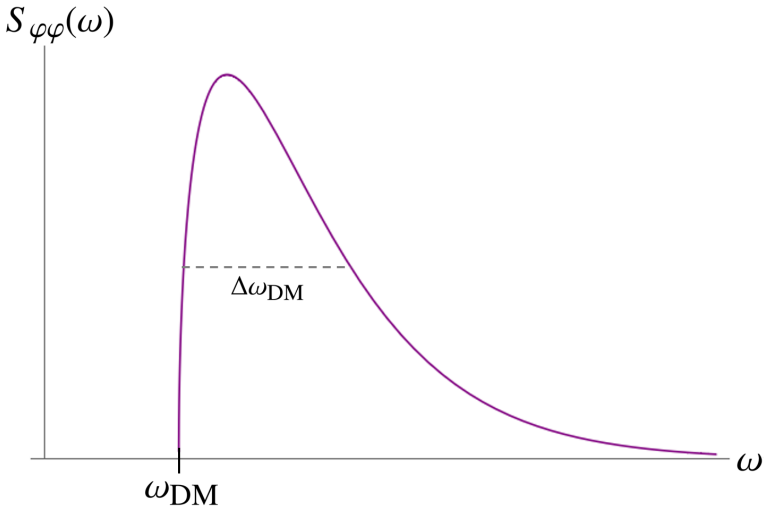

Figure 1.4: UDM frequency distribution: The frequency distribution of the UDM field φ, represented here as a power spectral density $S_{\varphi\varphi}$, is calculated from the DM velocity distribution through Doppler-shifting. The power spectral density of the UDM field is derived in Ref. [4].

1.3.3 Experimental signatures of UDM

Ultralight dark matter forms a coherent, oscillating field that fills the laboratory. There is a large number of experimentally measurable effects, corresponding to the large number of UDM candidates. Ultralight dark matter particles could be pseudo-scalar (spin-0), scalar (spin-0), or vector (spin-1). And within each of these categories there could exist a variety of different couplings to normal matter.

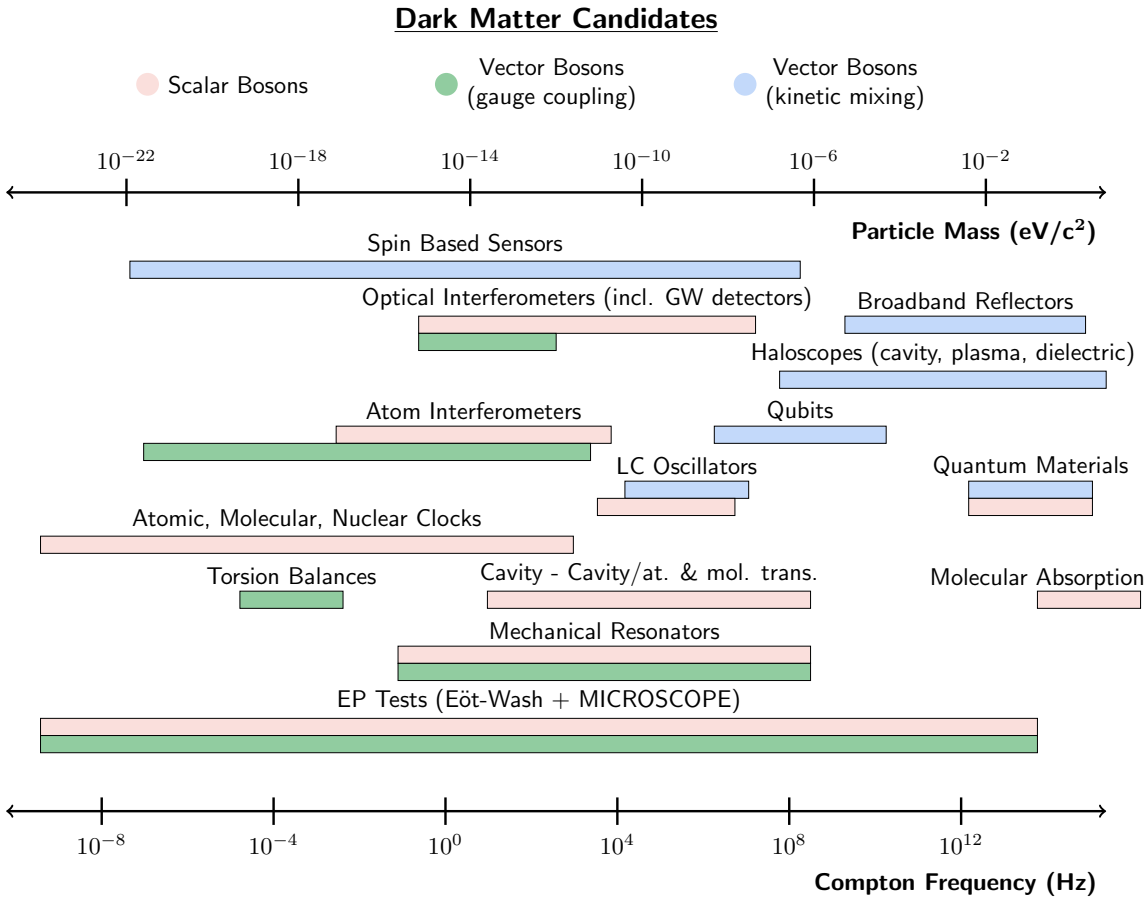

Figure 1.5: Detectors for UDM: Various types of detectors can be used to search for scalar and vector UDM. This dissertation focuses on scalar bosons and vector bosons with gauge couplings; kinetic mixing is beyond the scope of this dissertation. Figure reprinted from Ref. [5] with permission from Swati Singh and Joey Betz.

Some of the possible non-gravitational signatures of UDM include mechanical forces [66], modulation of atomic energy levels [30], mechanical strains [67], gravitational waves [68], precession of nuclear or electron spins [69], production of photons [70], and modulation of the refractive index of optical materials [71]. The multitude of potential UDM signals has motivated a diversity of detector types in the search for UDM. Figure 1.5 presents the categories of UDM detectors, both current and future, for scalar and vector candidates. Given the uncertainty in the frequency of UDM particles, it is important to have experiments spanning a wide frequency range.

1.4 Optomechanical detectors for UDM

This work focuses on UDM candidates that are expected to have mechanical signatures, which would be detectable with mechanical detectors. In particular, vector UDM particles with couplings to atomic matter would exert a material dependent force on a detector [72], and scalar UDM candidates with weak couplings to photons or electrons would produce a mechanical strain signal [67].

In particular, optomechanical systems use light to measure and control mechanical motion. These systems are important for a wide variety of sensing applications, with optomechanical devices spanning many orders of magnitude in size while achieving state-of-the-art sensitivities to mechanical signals. For example, a displacement sensitivity of 10^{-19} m $\mathrm{Hz}^{-1/2}$ and strain sensitivity of 10^{-23} $\mathrm{Hz}^{-1/2}$ has been achieved by LIGO [73], a km-scale gravitational wave detector with 40 kg test masses, while a force sensitivity of 10^{-18} N $\mathrm{Hz}^{-1/2}$ has been achieved with a 10-μm-diameter optically levitated silica sphere with a mass of only $\sim$ 1 ng [74].

Figure 1.6 illustrates a basic optomechanical device, where a mirror is attached to a mechanical oscillator, coupling its motion to light from a laser. Specifically, this is a cavity optomechanical system [75], where a fixed mirror is added to form an optical cavity (resonator) that amplifies the optical field and enhances the coupling between the oscillator and the laser light. Cavity optomechanical systems can be used as mechanical sensors, where a mechanical signal drives the motion of the mechanical oscillator, which can be measured optically.

Optical readout is fundamentally limited by photon shot noise due to the quantum nature of light. Photon shot noise limits the sensitivity of an optomechanical sensor through two mechanisms: imprecision and backaction. Interferometric measurements of the oscillator's position are subject to error from stochastic fluctuations in the measured optical power due to the random arrival times of photons. This error is referred to as readout imprecision, and it can be reduced by increasing the optical power or the cavity's finesse. Backaction refers to the effect an optical measurement has on the system. Through the radiation pressure force exerted on the mirror by the laser light, photons impart random momentum kicks

to the oscillator. The resulting jitter in the oscillator's motion can potentially obscure the motion induced by a signal. Imprecision noise and backaction noise are inversely related, imposing a fundamental limit on an optomechanical sensor's ability to detect weak mechanical signals. This limit is known as the standard quantum limit (SQL), which is achieved by tuning the optical power or cavity finesse to balance the effects of imprecision and backaction [75]. Modern cavity optomechanical systems are capable of performing displacement measurements at the SQL [76], and can even measure displacements below the SQL using squeezed light [77] and backaction evasion techniques [78].

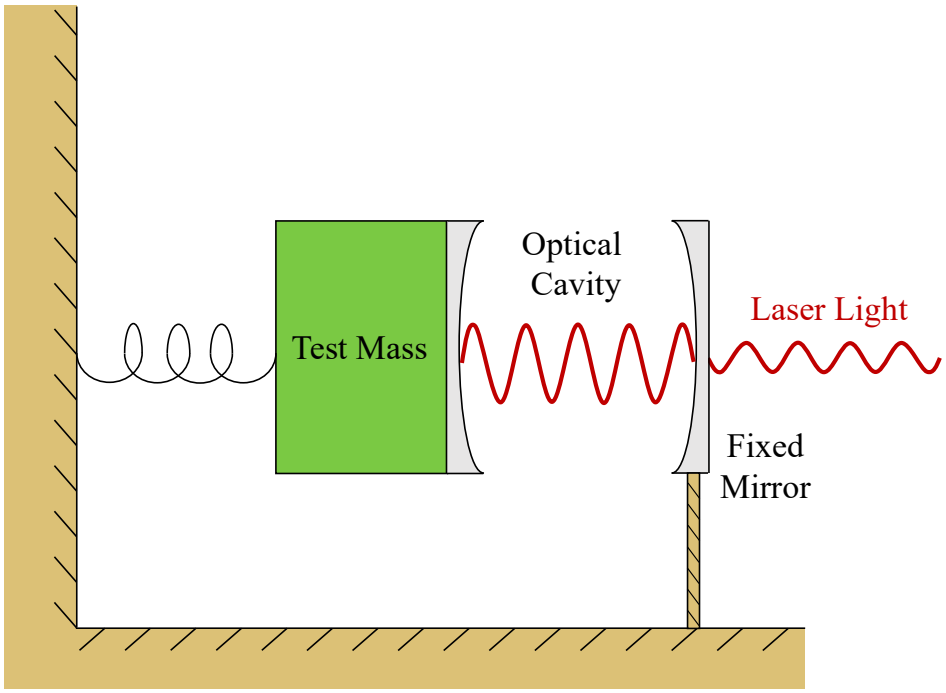

Figure 1.6: General cavity optomechanical sensor: The position of a test mass, generically modeled as a harmonic oscillator, is measured optically (laser light in red) using an optical cavity. For example, the position of the test mass can be inferred from the optical phase using a homodyne interferometer.

An unavoidable limit to the sensitivity of a mechanical sensor comes from thermal noise in the oscillator, which can be the dominant noise source in a sensor with low-noise displacement readout. Furthermore, optomechanical resonators are optomechanical sensors

that utilize the oscillator's mechanical resonances to amplify signals over the optical readout noise, such that the sensitivity may be thermally-limited near the resonance frequencies [79, 80]. Thermal noise can generally be reduced by cooling the system down, which can be accomplished with optical feedback cooling, where radiation pressure is used to damp the resonator's motion based on feedback from the position measurement [75]. However, for sensing experiments, feedback cooling can suppress the mechanical signal equally as the thermal noise [81]. A straightforward alternative is cryogenic cooling, where the system is coupled to a low temperature thermal bath; i.e. placed in a refrigerator. The compact form factors of many optomechanical resonators make them compatible with dilution refrigerators, enabling deep cryogenics.

Mechanical resonators in general are well-suited to the search for UDM, in part because their resonance frequencies typically lie in the Hz-GHz range, a frequency range in which the sensitivity of precision atomic experiments (which dominate the UDM search at lower frequencies) is limited [5]. The drawback is the reduction in bandwidth that naturally accompanies resonant detectors. Given the uncertainty in the UDM field's frequency, narrow detection bandwidths limit the scope of a resonant search for UDM. There are, however, ways to increase the frequency span of resonator-based searches. The mechanical frequencies of optomechanical resonators are often tunable[7] through, for example, stress or pressurization [83], thermal forcing [84], and radiation pressure forcing [85]. A tunable resonator can effectively increase its bandwidth by performing a frequency scan. Additionally, compact form factors enable the use of detector arrays, which can be used to provide coverage of a larger frequency range, enhance sensitivity through correlated measurements [66], or probe for UDM field gradients [4].

1.5 Outline of this dissertation

The purpose of this dissertation is to assess the ability of existing and near-future tabletop devices, primarily based on mechanical systems, to serve as detectors for ultralight

[7] For example, the resonance frequencies of a superfluid helium-based resonator can potentially be tuned by up to ~ 50 % fractional bandwidth via pressurization [82].

dark matter.

Chapter 2 introduces vector and scalar UDM, including an analysis to determine the signals they would produce. An example UDM search is provided to explain generally how UDM experiments are conducted and how to interpret the results. The chapter concludes with a summary of the current status of the search for vector and scalar UDM.

In Chapter 3, optomechanical membranes are proposed as resonant detectors for vector UDM. This chapter is based on the work in Ref. [42].

In Chapter 4, compact mechanical resonators are proposed as detectors to search for scalar UDM. This chapter is based on the work in Ref. [33].

In Chapter 5, an optical fiber-based detector is proposed to perform a broadband, low-frequency search for scalar UDM, supplementing the mechanical resonators discussed in Chapter 4.

Chapter 6 is a summary, including a discussion of future work.

Appendix A provides notation and definitions that may be helpful for understanding the vector and scalar field theory presented in Chapter 2.

Appendix B provides additional technical details supporting the calculations done in this Chapter 5.

1.6 List of Publications

Dissertation Work

1. J. Manley, D. J. Wilson, R. Stump, D. Grin, and S. Singh. Searching for scalar dark matter with compact mechanical resonators. Physical Review Letters **124**, 151301 (2020).

2. J. Manley, M. D. Chowdhury, D. Grin, S. Singh, and D. J. Wilson. Searching for vector dark matter with an optomechanical accelerometer. Physical Review Letters **126**, 061301 (2021).

3. J. Manley, R. Stump, R. Petery, and S. Singh. Optical Fiber-Based Detector for Scalar Ultralight Dark Matter. *To be submitted* (July 2022).

Additional Work

1. D. Carney *et al*. Mechanical quantum sensing in the search for dark matter. Quantum Science and Technology, 6(2), 024002 (2021).

2. V. Vadakkumbatt, M. Hirschel, J. Manley, T. J. Clark, S. Singh, and J. P. Davis. Prototype superfluid gravitational wave detector. Physical Review D **104**, 082001 (2021).

3. J. Betz, J. Manley, E. M. Wright, D. Grin, and S. Singh. Searching for chameleon dark energy with mechanical systems. arXiv:2201.12372 (2022).

4. D. Antypas *et al*. New Horizons: Scalar and Vector Ultralight Dark Matter. arXiv:2203.14915 (2022).

Chapter 2

VECTOR AND SCALAR UDM: SIGNALS AND SEARCHES

The purpose of this chapter is to provide the prerequisite analyses and background information for the UDM searches that will be proposed in Chapters 3, 4, and 5.

In Sections 2.1 and 2.2 derivations are presented for the relevant physical effects induced by non-gravitational interactions between UDM and normal matter, which will determine the types of detectors considered in subsequent chapters. For additional background on the notation and definitions used in these sections along with technical details, see Appendix A.

The capability of a DM detector is determined by how weak a signal it can detect; i.e. how strong the signal must be to overcome the noise. An example UDM search is provided in Section 2.3, considering a simple mechanical detector to demonstrate the calculation of the minimum detectable signal strength in the presence of noise.

An experiment that is sensitive to weaker signal strengths, or different frequencies, than previous experiments has the ability to either detect dark matter or provide novel constraints on the dark matter parameter space. In Section 2.4, fifth forces and equivalence principle (EP) tests are introduced. EP test experiments currently provide some of the broadest constraints on UDM models, setting a benchmark for future experiments. In Section 2.5 presents the full parameter spaces for vector and scalar UDM, summarizing the current state of the UDM search.

2.1 Vector UDM signal

This section considers a scenario where UDM is composed of vector (spin-1) particles with mass[1] m_{DM}. A model for the vector UDM field will be provided in order to quantify the force it exerts on particles.

A variety of possible non-thermal production mechanisms exist for vector UDM in the Universe [86, 88, 89, 90, 91, 92, 93, 94, 95, 96], such as the misalignment mechanism [86, 88, 89], parametric resonance [91], or quantum fluctuations during inflation [89].

Ultralight dark matter (including scalars and pseudo-scalars [97]) can be produced via the misalignment mechanism [98].[2] In an expanding Universe, the equation of motion for the spatial components of a vector field A^i is[3]

$$\ddot{A}^i + 3H(t)\dot{A}^i + \left(\frac{m_{\mathrm{DM}}c^2}{\hbar}\right)^2 A^i = 0 \tag{2.1}$$

where m_{DM} is the DM particle mass and $H(t)$ is the Hubble constant. The equation of motion takes the form of a damped harmonic oscillator, where the damping term is due to the expansion of the Universe. In the early Universe, when $H(t) \gg \left(\frac{m_{\mathrm{DM}}c^2}{\hbar}\right)$, overdamping prevents oscillation, and the field is "stuck" at its initial, random value [86].

At a later time, as $H(t)$ decreases, the field begins to oscillate (in the absence of damping due to decay processes [86]). The field's oscillation modes behave as cold dark matter (and the amount of DM produced depends on the initial field value [88]), which can be seen by the scaling of their energy density ρ with the Universe scale factor a: $\rho \propto a^{-3}$ [86]. The production of vector UDM via the misalignment mechanism is possible for particle masses $m_{\mathrm{DM}} \gtrsim 10^{-34}$ eV$/c^2$ [88], which is less stringent than the lower bounds from astrophysical constraints [40].

---

[1] The mass of vector UDM could come from the Higgs [86] or Stueckelberg mechanisms [87, 88].

[2] See Ref. [88] for more details on the misalignment mechanism for vector fields.

[3] After inflation, the field is approximately spatially uniform within the observable universe, such that spatial derivatives are negligible ($\partial_i A^\mu = 0$) [97]. It can then be shown that the time component of the field can be neglected ($A^0 = 0$) [88].

Alternatively, quantum fluctuations of a vector field during inflation can produce ultralight vector dark matter [89]. While vector UDM production via the misalignment mechanism requires an additional nonminimal coupling to gravity [89, 91], production via inflationary fluctuations only requires the vector particles to have no significant self-interactions [89]. For inflationary quantum fluctuations to produce the entire late-Universe DM abundance, the vector UDM particle masses must be $m_{\rm DM} \gtrsim 10^{-5}\ {\rm eV}/c^2$. However, lighter vector UDM particles produced in this way could still form a subcomponent of the total DM density [89].

Another non-thermal production mechanism, referred to as "parametric resonance," has been recently introduced [91] for vector UDM whose mass arises from a dark Higgs field. If the initial dark Higgs field value (after inflation) is displaced from its minimum, its oscillations produce vector UDM particles via parametric resonance. The vector UDM particle mass must be $m_{\rm DM} \gtrsim 10^{-18}\ {\rm eV}/c^2$ for this production mechanism to account for the majority of the DM density [91].

Vector UDM particles are sometimes referred to as "dark photons," given the similarity to ordinary photons, which can be seen by comparing the theoretical treatment of vector UDM in this section with the treatment of electromagnetism in Appendix A.2. However, vector UDM differs from ordinary photons in that they have nonzero rest mass and may couple to a conserved quantity other than electric charge.

As in the case of photons, vector UDM can be represented by a vector field A'^{ν} with a Proca Lagrangian density:

$$\mathcal{L}' = -\frac{c^2\epsilon'}{4}F'_{\mu\nu}F'^{\mu\nu} + \frac{c^2\epsilon'}{2}\left(\frac{m_{\rm DM}c}{\hbar}\right)^2 A'^{\nu}A'_{\nu} - J'^{\nu}A'_{\nu}. \tag{2.2}$$

The Lagrangian's form is similar to the electromagnetic Lagrangian (Eqs. A.9 and A.13) presented in Appendix A, where the second term is added to account for the mass $m_{\rm DM}$ of the dark matter particles. Primes ($'$) are used to distinguish dark matter quantities from the analogous electromagnetic variables.[4] J'^{ν} is a conserved fermionic 4-current density, $F'^{\mu\nu} \equiv \partial^{\mu}A'^{\nu} - \partial^{\nu}A'^{\mu}$ is the field tensor, and ϵ' is a constant analogous to the vacuum permittivity ϵ_0.

[4] See Appendix A for more details on the definitions of these variables.

A'^{ν} is again a four-potential with components $\left\{\frac{V'}{c}, \boldsymbol{A}'\right\}$, where V' is the scalar potential and $\boldsymbol{A}'$ is the vector potential.

2.1.1 Field solution

The field equations for A'^{μ} are

$$\partial_\mu \left(\partial^\mu A'^{\nu} - \partial^\nu A'^{\mu}\right) + \left(\frac{m_{\mathrm{DM}} c}{\hbar}\right)^2 A'^{\nu} = \frac{J'^{\nu}}{c^2 \epsilon'}, \tag{2.3}$$

which can be found by applying the Euler-Lagrange equations to Eq. (2.2) (see Appendix A.2.2).

Note that the $\partial_\mu A'^{\mu} = 0$, given that J'^{ν} is a conserved current [5]. Also, given that the interaction between A'^{ν} and J'^{ν} is necessarily weak, and that normal matter fills only a small fraction of space in the Galaxy, Eq. (2.3) can be simplified by neglecting the source term. So dark matter is modeled as a vector field in vacuum,

$$\partial_\mu \partial^\mu A'^{\nu} + \left(\frac{m_{\mathrm{DM}} c}{\hbar}\right)^2 A'^{\nu} \approx 0, \tag{2.4}$$

with sinusoidal solutions of the form[6]

$$A'^{\nu} = A'^{\nu}_a \sin\left(\omega t - \boldsymbol{k} \cdot \boldsymbol{r} + \theta\right), \tag{2.5}$$

where, ω is the DM's Doppler-shifted (see Section 1.3.2) angular Compton frequency $\omega_{\mathrm{DM}} = m_{\mathrm{DM}} c^2/\hbar$, and

$$\boldsymbol{k}^2 = \frac{\omega^2}{c^2} - \left(\frac{m_{\mathrm{DM}} c}{\hbar}\right)^2 \approx \left(\frac{2\pi}{\lambda_{\mathrm{DM}}}\right)^2. \tag{2.6}$$

---

[5] For a conserved current J'^{ν} (e.g. the electromagnetic current density) $\partial_\nu J'^{\nu} = 0$, so $\partial_\mu A'^{\mu} = 0$ follows from taking the derivative ∂_ν of (2.3).

[6] The subscript $()_a$ is used to denote the amplitude of each oscillating component. For example:

$$A'^{0} = \frac{V'_a}{c} \sin\left(\omega t - \boldsymbol{k} \cdot \boldsymbol{r} + \theta\right)$$
$$\boldsymbol{A}' = \boldsymbol{A}'_a \sin\left(\omega t - \boldsymbol{k} \cdot \boldsymbol{r} + \theta\right)$$

The DM field oscillates in time at its Compton frequency with spatial variation determined by the de Broglie wavelength $\lambda_{\rm DM} = h/m_{\rm DM}v_{\rm DM}$. The phase factor θ is not significant in this discussion; it will be omitted moving forward.

A realistic UDM model should account for dark matter's velocity distribution (see Section 1.3), which translates to a frequency distribution via Doppler-shifts, resulting in a field solution that is a superposition of sinusoids. For simplicity, UDM will continue to be treated as a monochromatic field throughout this section, but the results can be generalized to account for the true UDM frequency distribution.

2.1.2 Force on particles

Given a vector field A'^{ν}, the force exerted on a particle can be derived in the same manner as in Appendix A.2.4. The fact that the vector field has mass does not change the form of the interaction terms in the total Lagrangian density, so the force exerted by the vector field on a particle with dark charge q' and velocity $\boldsymbol{v}$ is simply

$$\boldsymbol{F} = q' \left(\boldsymbol{E}' + \boldsymbol{v} \times \boldsymbol{B}'\right), \tag{2.7}$$

where the dark electric and dark magnetic fields are defined in analogy to electromagnetics,

$$\boldsymbol{E}' \equiv -\nabla V' - \frac{\partial \boldsymbol{A}'}{\partial t}, \quad \boldsymbol{B}' \equiv \nabla \times \boldsymbol{A}'. \tag{2.8}$$

From (2.5), the dark electric field is[7]

$$\boldsymbol{E}' = \left(\boldsymbol{k}V'_a - \omega \boldsymbol{A}'_a\right) \cos\left(\omega t - \boldsymbol{k} \cdot \boldsymbol{r}\right) \approx -\omega \boldsymbol{A}'_a \cos\left(\omega t - \boldsymbol{k} \cdot \boldsymbol{r}\right) \tag{2.9}$$

and the dark magnetic field is

$$\boldsymbol{B}' = \left(\boldsymbol{A}'_a \times \boldsymbol{k}\right) \cos\left(\omega t - \boldsymbol{k} \cdot \boldsymbol{r}\right). \tag{2.10}$$

[7] It can be shown from $\partial_\nu A'^{\nu} = 0$ that $V'_a \leq v_{\rm DM} \left|\boldsymbol{A}'_a\right|$. And given that $v_{\rm DM} \ll c$, it follows that $|\boldsymbol{k}|\, V'_a \ll \omega \left|\boldsymbol{A}'_a\right|$. So contributions from V'_a are suppressed.

For non-relativistic particles ($v \ll c$), it can be shown that the dark magnetic contribution to the force due to DM is negligible, being suppressed relative to the dark electric contribution by a factor of $\frac{v \cdot v_{\rm DM}}{c^2}$.[8] So we have

$$\boldsymbol{F}_{\rm DM} \approx q' \boldsymbol{E}' \approx -q' \omega \boldsymbol{A}'_a \cos\left(\omega t - \boldsymbol{k} \cdot \boldsymbol{r}\right). \tag{2.11}$$

2.1.3 Field amplitude

The strength of the force signal depends on the field's amplitude. The field amplitude can be expressed in terms of the energy density. And the energy density of dark matter in the Solar Neighborhood is estimated to be $\rho_{\rm DM} \approx 0.4\ {\rm GeV/cm^3}$ [57].

The field's energy density comes from the 00-component of the symmetrized stress-energy tensor $\bar{T}'^{\mu\nu}$. For a vector field with mass, $\bar{T}'^{\mu\nu}$ resembles the massless form derived in Appendix A.2.3, with the addition of a mass term:

$$\bar{T}'^{\mu\nu} = c^2 \epsilon' \left(-F'^{\mu\alpha} F'^{\nu}{}_{\alpha} + \frac{1}{4} \eta^{\mu\nu} F'_{\alpha\beta} F'^{\alpha\beta} - \frac{1}{2} \left(\frac{m_{\rm DM} c}{\hbar} \right)^2 A'^{\alpha} A'_{\alpha} \right). \tag{2.12}$$

The energy density of dark matter is then[9]

$$\rho_{\rm DM} = \bar{T}'^{00} \approx \frac{1}{2} \epsilon' \omega^2 \left| \boldsymbol{A}'_a \right|^2. \tag{2.13}$$

The field amplitude is determined by the cycle-averaged local DM density:

$$\left| \boldsymbol{A}'_a \right| \approx \frac{1}{\omega} \sqrt{2 \frac{\rho_{\rm DM}}{\epsilon'}}. \tag{2.14}$$

Thus, the magnitude of the dark electric force is

$$F_{\rm DM} \approx -q' \omega \left| \boldsymbol{A}'_a \right| \cos\left(\omega t - \boldsymbol{k} \cdot \boldsymbol{r}\right) \approx -q' \sqrt{2 \frac{\rho_{\rm DM}}{\epsilon'}} \cos\left(\omega t - \boldsymbol{k} \cdot \boldsymbol{r}\right) \tag{2.15}$$

---

[8] From Eqs. (2.7) and (2.10), dark magnetic contribution to the force is

$$|\boldsymbol{F}| \leq q' v \left| \boldsymbol{B}' \right| \leq v q' \left| \boldsymbol{A}'_a \right| |\boldsymbol{k}| = v v_{\rm DM} q' \frac{m_{\rm DM}}{\hbar} \left| \boldsymbol{A}'_a \right| = \frac{v v_{\rm DM}}{c^2} q' \omega_{\rm DM} \left| \boldsymbol{A}'_a \right| \approx \frac{v v_{\rm DM}}{c^2} q' \left| \boldsymbol{E}'_a \right|.$$

[9] Equation (2.13) includes the approximations $c \left| \boldsymbol{B}'_a \right| \ll \left| \boldsymbol{E}'_a \right|$ and $\frac{V'^2_a}{c^2} \ll \left| \boldsymbol{A}'_a \right|^2$, which are a result of DM being non-relativistic ($v_{\rm DM} \ll c$).

2.1.4 Coupling strength parameterization

In this dissertation, the strength of the interaction between dark matter and dark charge will be parameterized with the dimensionless "coupling strength" g'. Vector UDM has multiple possible coupling channels. For example, two possibilities often considered in literature are that UDM couples to the baryon minus lepton ($B - L$) number [42, 66, 72] or baryon (B) number [42, 43]. However, to maintain generality, the exact coupling channel will not be specified in this section.

The amount of dark charge in a particle is proportional to the number N' of elementary dark charges within it,[10]

$$q' = e'N', \tag{2.16}$$

where the "elementary dark charge" e' has been introduced in analogy to the elementary electric charge e. Unlike electromagnetism, a vector UDM interaction has not yet been observed experimentally. So the values of constants e' and ϵ' are unknown.

The force in Eq. (2.15) has an unknown magnitude proportional to $e'/\sqrt{\epsilon'}$. The coupling strength g' is defined as

$$g' \equiv \frac{e'}{e}\sqrt{\frac{\epsilon_0}{\epsilon'}}, \tag{2.17}$$

so that the value of g' effectively expresses the strength of the vector UDM interaction with that of electromagnetism. With this convention, the vector UDM force can be written as

$$F_{\mathrm{DM}} \approx -g'N'F_{\mathrm{DM},0}\cos\left(\omega t - \boldsymbol{k}\cdot\boldsymbol{r}\right) \tag{2.18}$$

where

$$F_{\mathrm{DM},0} \equiv \sqrt{2\frac{e^2\rho_{\mathrm{DM}}}{\epsilon_0}} = 6\times10^{-16}\ \mathrm{N}. \tag{2.19}$$

Thus, for vector UDM with couplings to a conserved quantity such as the $B - L$ number, the signal is an oscillating force described by Eq. (2.18). Measurement of an oscillating force by a detector that is sufficiently isolated from extraneous forces (noise) can then be interpreted as evidence for vector UDM.

[10] In the case of $B - L$-coupling, this would be the number of baryons minus the number of leptons within the particle ($N' = N_{B-L} = N_B - N_L$).

2.2 Scalar UDM signal

This section considers a scenario where UDM is composed of scalar (spin-0) particles with mass $m_{\rm DM}$. A model for the scalar UDM field will be provided in order to quantify its effects on particles.

Scalar UDM can be produced non-thermally via the misalignment mechanism [98]. The discussion of scalar UDM production from the misalignment mechanism follows that for vector UDM in Section 2.1, where a scalar field φ is considered instead of the spatial components of a vector field A^i. The energy density of the scalar field again scales as $\propto a^{-3}$ (a is the Universe scale factor), as is expected for cold dark matter [86, 97, 98].

The behavior of a scalar field[11] $\varphi \equiv \varphi(t, \boldsymbol{r})$ in vacuum is described by the Klein-Gordon Lagrangian density [100]

$$\mathcal{L}_\varphi = \frac{c^4}{4\pi G}\left[\frac{1}{2}\partial_\mu\varphi\partial^\mu\varphi - \frac{1}{2}\left(\frac{m_{\rm DM}c}{\hbar}\right)^2\varphi^2\right]. \tag{2.20}$$

2.2.1 Field solution

The field solution for scalar UDM can be obtained with the same procedure used for vector UDM (see Section 2.1.1 for more details).

The equation of motion for the scalar field φ can be obtained from the Lagrangian density using the Euler-Lagrange equations:

$$\partial_\mu\left(\frac{\partial\mathcal{L}_\varphi}{\partial(\partial_\mu\varphi)}\right) = \frac{\partial\mathcal{L}_\varphi}{\partial\varphi}. \tag{2.21}$$

The resulting equation of motion is

$$\partial_\mu\partial^\mu\varphi + \left(\frac{m_{\rm DM}c}{\hbar}\right)^2\varphi = 0, \tag{2.22}$$

which has sinusoidal solutions of the form[12]

$$\varphi = \varphi_0\cos(\omega t - \boldsymbol{k}\cdot\boldsymbol{r}), \tag{2.23}$$

where $\boldsymbol{k}^2 = \left(\frac{2\pi}{\lambda_{\rm DM}}\right)^2$ and ω is the Doppler-shifted angular Compton frequency.

---

[11] Per the convention of Ref. [99], the field φ is chosen to be dimensionless.

[12] Here, the arbitrary phase θ is ignored, just as in Section 2.1.1 for the vector field solution.

2.2.2 Variation of fundamental constants

Chapter 4 considers a scalar UDM field that would cause atomic strains through their interactions with Standard Model particles. Specifically, linear couplings to photons or electrons create a scalar strain signal. These couplings are accounted for by adding interaction terms to the Lagrangian [99]

$$\mathcal{L}_{\text{interaction}} = d_e \varphi \frac{e^2 c}{16\pi\hbar\alpha_0} F_{\mu\nu}F^{\mu\nu} - d_{m_e}\varphi m_{e,0} c^2 \bar{\psi}_e \psi_e, \tag{2.24}$$

where d_e and d_{m_e} parameterize the coupling strength to photons and electrons, respectively.

The Lagrangian for photons in the presence of a scalar field is then[13]

$$\mathcal{L} = -(1 - d_e\varphi(t,\boldsymbol{r}))\frac{e^2 c}{16\pi\hbar\alpha_0} F_{\mu\nu}F^{\mu\nu} = -\frac{e^2 c}{16\pi\hbar\alpha(t,\boldsymbol{r})} F_{\mu\nu}F^{\mu\nu}, \tag{2.25}$$

where

$$\alpha(t,\boldsymbol{r}) \equiv \frac{\alpha_0}{1 - d_e\varphi(t,\boldsymbol{r})}. \tag{2.26}$$

This redefinition of the fine-structure constant to account for the scalar field allows the photon Lagrangian to keep its original form. Similarly, a scalar coupling to electrons can be absorbed by the electron mass:

$$m_e(t,\boldsymbol{r}) \equiv (1 + d_{m_e}\varphi(t,\boldsymbol{r}))m_{e,0}. \tag{2.27}$$

Scalar interactions can generally be modeled as a variation of fundamental constants [99, 101]. For scalar couplings to photons and electrons, the fine-structure constant and electron mass effectively inherit the spatial and temporal dependence of the scalar field. Therefore, scalar UDM produces an effective variation of fundamental constants that results in physically measurable effects.

---

[13] Notation: Throughout this dissertation, the fields' arguments $(t,\boldsymbol{r})$ are often omitted for conciseness. However, the scalar field's arguments have been temporarily reintroduced here, $\varphi \to \varphi(t,\boldsymbol{r})$, to highlight the fact that m_e and α have spatial and temporal dependence.

2.2.3 Field amplitude

As in Section 2.1.3, the field amplitude φ_0 can be related to the DM energy density $\rho_{\rm DM}$ by finding the stress-energy tensor:

$$T^{\mu\nu} = \partial^\nu \varphi \frac{\partial \mathcal{L}_\varphi}{\partial\left(\partial_\mu \varphi\right)} - \eta^{\mu\nu}\mathcal{L}_\varphi. \tag{2.28}$$

Using Eq. (2.20) yields

$$T^{\mu\nu} = \frac{c^4}{4\pi G}\left[\frac{1}{2}\partial^\mu\varphi\partial^\nu\varphi + \frac{1}{2}\left(\frac{m_{\rm DM}c}{\hbar}\right)^2 \eta^{\mu\nu}\varphi^2\right]. \tag{2.29}$$

We can see from Eq. (2.29) that $T^{\mu\nu}$ is already symmetric for a scalar field.[14]

For the sinusoidal field solution in Eq. (2.23)

$$\rho_{\rm DM} = T^{00} \approx \frac{c^4}{8\pi G}\left(\frac{\omega}{c}\right)^2 {\varphi_0}^2, \tag{2.30}$$

where the approximation comes from neglecting the Doppler shift ($\omega \approx m_{\rm DM}c^2/\hbar$).

Therefore, the field amplitude is

$$\varphi_0 = \sqrt{\frac{8\pi G\rho_{\rm DM}}{c^2\omega^2}}. \tag{2.31}$$

This is the amplitude a single plane wave would have if it accounted for the entire UDM field. However, scalar UDM is a stochastic field. It has a frequency distribution (Fig. 1.4) and is a superposition of many such plane waves (Eq. 1.3). Therefore, what has been derived in this section is really the root-mean-square of the field amplitude [65]

$$\varphi_{\rm rms} = \sqrt{\frac{8\pi G\rho_{\rm DM}}{c^2{\omega_{\rm DM}}^2}}, \tag{2.32}$$

and the field's linewidth is narrow enough to approximate $\omega \approx \omega_{\rm DM}$. The stochastic field discussion applies equally to the vector field analysis in Section 2.1.

[14] Symmetrization of stress-energy tensor for a vector field is done in Appendix A.2.3.

2.2.4 Strain signal

The fine-structure constant and electron mass are parameters to the Bohr radius. Oscillation of α or m_e results in oscillation of the Bohr radius:[15]

$$\begin{aligned} a(t,\boldsymbol{r}) &= \frac{\hbar}{m_e(t,\boldsymbol{r})\, c\, \alpha(t,\boldsymbol{r})} \\ &= \frac{\hbar}{m_{e,0} c \alpha_0} \frac{1 - d_e\varphi(t,\boldsymbol{r})}{1 + d_{m_e}\varphi(t,\boldsymbol{r})} \\ &\approx a_0 \left(1 - (d_e + d_{m_e})\, \varphi(t,\boldsymbol{r})\right). \end{aligned}$$

Neglecting higher-order, relativistic corrections, the size of a macroscopic object is proportional to the Bohr radius [102]. Modulation of the Bohr radius results in an isotropic strain h_{DM} in a macroscopic object,[16]

$$h_{\mathrm{DM}}(t,\boldsymbol{r}) \approx -\left(d_e + d_{m_e}\right) h_{\mathrm{DM},0} \cos\left(\omega t - \boldsymbol{k}\cdot\boldsymbol{r}\right), \tag{2.33}$$

where the amplitude is simply the scalar field amplitude from Eq. (2.31)

$$h_{\mathrm{DM},0} \equiv \varphi_0. \tag{2.34}$$

Thus, if scalar UDM couples to photons or electrons, the signal is an oscillating strain described by Eq. (2.33).

2.3 Example: UDM search with a mechanical detector

This section provides an example to explain mechanical UDM detectors and how to assess their capability in the context of a dark matter search.

---

[15] The approximation comes from neglecting higher order terms of $d_i\varphi$. The current constraints on d_e and d_{m_e} (see Section 2.5) ensure that $d_i\varphi_0 \ll 1$ across the particle mass range considered in this dissertation.

[16] $h_{\mathrm{DM}}(t,\boldsymbol{r}) = \frac{\delta a}{a_0}(t,\boldsymbol{r}) \approx -\frac{\delta\alpha}{\alpha_0}(t,\boldsymbol{r}) - \frac{\delta m_e}{m_{e,0}}(t,\boldsymbol{r})$

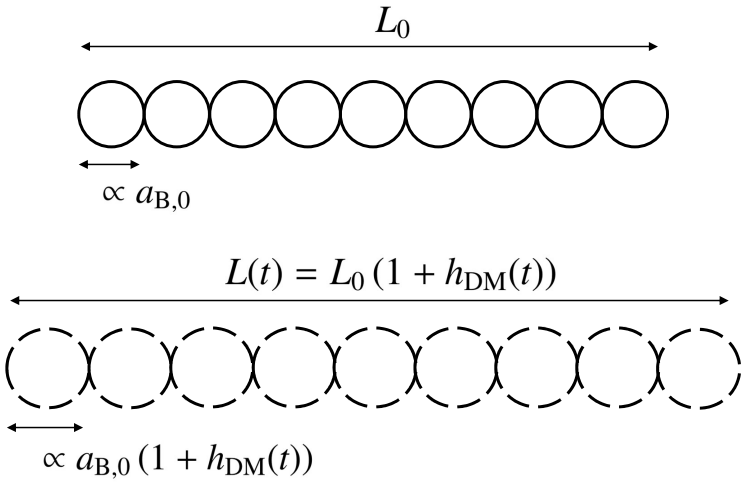

Figure 2.1: Macroscopic strain from scalar UDM: Through modulation of the Bohr radius a_{B}, scalar UDM strains atoms by $h_{\mathrm{DM}}(t)$. Considering a simple model with a 1-dimensional bar of length L_0, it can be seen that the equilibrium position of each atom shifts by an amount $\sim x h_{\mathrm{DM}}(t)$, where x is the atom's equilibrium distance from the center of the bar. This causes the bar to expand to a length of $L(t) = L_0\,(1 + h_{\mathrm{DM}}(t))$.

2.3.1 Harmonic oscillator as a force sensor

Consider a simple force sensor, modeled as a harmonic oscillator, as in Fig. 2.2. Suppose the UDM signal is a coherent, oscillating force acting on the test mass m of the form

$$F_{\mathrm{DM}} = F_0 \cos(\omega_{\mathrm{DM}} t)\,, \tag{2.35}$$

with amplitude

$$F_0 = g' \alpha_m F_{\mathrm{DM},0}, \tag{2.36}$$

where g' is the unknown DM-coupling strength and the force amplitude $F_{\mathrm{DM},0}$ accounts for the UDM field strength. The factor α_m describes the coupling between the DM force and the detector, and generally depends on the detector geometry and composition.

Unwanted external forces F_{ext} (or "force noise"), such as thermomechanical fluctuations, external acoustic vibrations, or measurement backaction, act on the test mass in

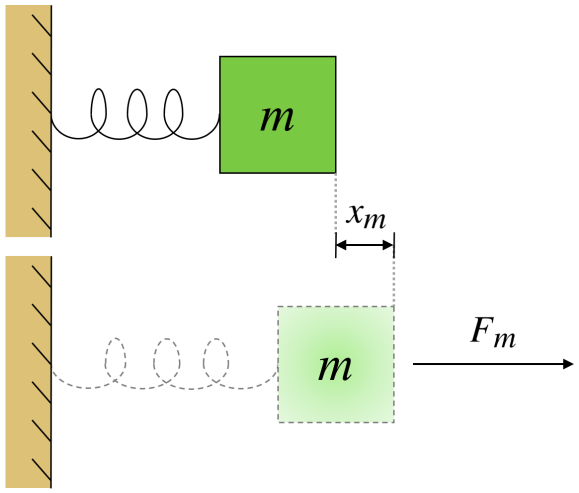

Figure 2.2: Example force sensor: Mechanical force sensors can be generally modeled as harmonic oscillators. A driving force F_m displaces the test mass m a distance x_m from its equilibrium position.

addition to the DM signal. The total force on the test mass is

$$F_m = F_{\mathrm{DM}} + F_{\mathrm{ext}}. \tag{2.37}$$

The position of the test mass obeys the equation of motion for a damped, driven harmonic oscillator

$$m\ddot{x}_m + m\gamma_m\dot{x}_m + m{\omega_m}^2 x_m = F_m, \tag{2.38}$$

where γ_m is the dissipation and ω_m is the oscillator's resonance frequency. The oscillator's mechanical quality factor (Q-factor) is defined in terms of the dissipation as $Q_m \equiv \omega_m/\gamma_m$.

In a dark matter search, the force F_m is measured over time. If the dark matter force signal exists, it would present itself as a spike in the power spectral density (PSD) of the measured force S_{FF}^{m}, exceeding the noise floor S_{FF}^{ext} at a single frequency ω_{DM}.

The force F_m is generally inferred from a measurement of the test mass position x_m.[17] However, due to imprecision x_{imp} in the position measurement, the apparent position of the

[17] In an experiment with an optomechanical detector, for example, the test mass position is inferred from an optical power measurement in an interferometric setup. In this case, the experimental data may be the measured photocurrent at a photodetector, from which the position x_m is inferred based on a calibration of the optical readout system.

test mass is

$$x = x_{\text{imp}} + x_m. \tag{2.39}$$

The Fourier transform of Eq. (2.39) is

$$\tilde{x} = \tilde{x}_{\text{imp}} + \chi_{xF,m}\left(\tilde{F}_{\text{ext}} + \tilde{F}_{\text{DM}}\right) \tag{2.40}$$

where

$$\chi_{xF,m} = m^{-1}\left({\omega_m}^2 - \omega^2 - i\frac{\omega\omega_m}{Q_m}\right)^{-1} \tag{2.41}$$

is the mechanical susceptibility, which is obtained from Fourier transforming Eq. (2.38).

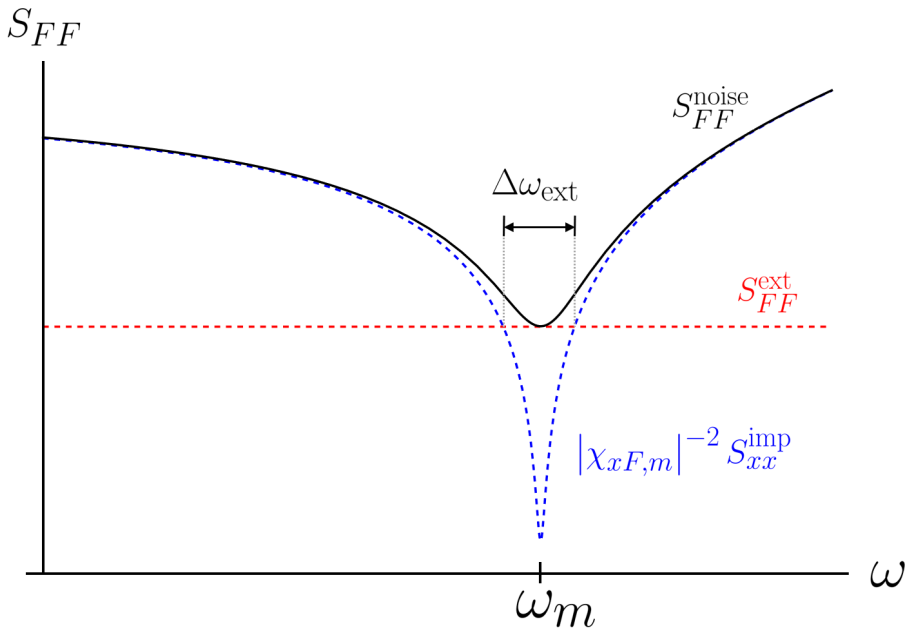

Figure 2.3: Noise curves for example force sensor: Resonant detectors are often limited by measurement imprecision off resonance. On resonance, the actual motion of the test mass may be resolvable, in which case the noise floor is set by external forces. This particular detector has a mechanical quality factor $Q_m = 100$. The plot is on a log-log scale.

If F_{ext}, F_{DM}, and x_{imp} are not correlated, the PSDs of the oscillator's apparent position and apparent force are

$$S_{xx} = S_{xx}^{\text{imp}} + \left|\chi_{xF,m}\right|^2\left(S_{FF}^{\text{ext}} + S_{FF}^{\text{DM}}\right) \tag{2.42}$$

$$S_{FF} = \left|\chi_{xF,m}\right|^{-2} S_{xx}^{\text{imp}} + S_{FF}^{\text{ext}} + S_{FF}^{\text{DM}}. \tag{2.43}$$

The total force noise PSD is defined as

$$S_{FF}^{\text{noise}} \equiv \left|\chi_{xF,m}\right|^{-2} S_{xx}^{\text{imp}} + S_{FF}^{\text{ext}}. \tag{2.44}$$

The force noise for a harmonic oscillator with $Q_m = 100$ is plotted in Fig. 2.3, assuming broadband displacement noise due to readout imprecision $\left(\frac{\partial}{\partial\omega} S_{xx}^{\text{imp}} = 0\right)$ and broadband force noise $\left(\frac{\partial}{\partial\omega} S_{FF}^{\text{ext}} = 0\right)$. The force sensor achieves the best force sensitivity[18] on resonance, where external forces (both noise F_{ext} and signal F_{DM}) are amplified and can overcome the readout imprecision noise. The sensitivity is limited by external forces $\left(S_{FF}^{\text{ext}} \geq \left|\chi_{xF,m}\right|^{-2} S_{xx}^{\text{imp}}\right)$ over a bandwidth $\Delta\omega_{\text{ext}}$.

2.3.2 Standard quantum limit (SQL) for optical readout noise

If the hypothetical force sensor considered so far in this section is a cavity optomechanical sensor like the one depicted in Fig. 1.6, the sensitivity can be limited by photon shot noise. As discussed in Section 1.4, shot noise in the optical readout system encompasses both readout imprecision and measurement backaction

$$S_{FF}^{\text{noise}} \equiv \left|\chi_{xF,m}\right|^{-2} S_{xx}^{\text{imp}} + S_{FF}^{\text{ba}}. \tag{2.45}$$

From the uncertainty relation between photon number N and optical phase θ, it can be shown that the one-sided PSDs of the fluctuations in phase and photon flux $\dot{N}$ of a coherent beam can be related as $\sqrt{S_{\dot{N}\dot{N}} S_{\theta\theta}} = 1$ [103]. The arrival times of photons have a Poisson distribution, so that the shot noise PSD of the photon flux is related to the average photon number flux $\bar{\dot{N}}$ as $S_{\dot{N}\dot{N}} = 2\bar{\dot{N}}$. For a single-sided optical cavity the average photon number flux is related to the laser power P and wavelength λ as $\bar{\dot{N}} = P\lambda/2\pi\hbar c$, assuming the laser wavelength is resonant with the cavity [103].

[18] Sensitivity is typically defined as the square root of the noise floor: $\sqrt{S_{FF}^{\text{noise}}}$.

Given an optical cavity with finesse $\mathcal{F}$, the uncertainty in the optical phase $\theta_{\rm imp}$ produces imprecision in a measurement of the displacement of one of the end mirrors as $x_{\rm imp} = \theta_{\rm imp}\lambda/8\mathcal{F}$ [103],[19] so the imprecision noise displacement PSD is

$$S_{xx}^{\rm imp} = \frac{\pi\hbar c\lambda}{64\mathcal{F}^2 P}. \tag{2.46}$$

To determine the backaction noise, note that each photon exerts a momentum kick of $\Delta p = 4\pi\hbar/\lambda$ on the movable mirror [103]. The radiation pressure force exerted on the mirror is then $F_{\rm ba} = n\Delta p/\tau_{\rm p}$, where $\tau_{\rm p} = 2L/c$ is the cavity's round-trip travel time and n is the number of photons within the cavity [75]. If the laser wavelength is resonant with the cavity, The PSD of fluctuations in photon number is $S_{nn} = 8\bar{n}/\kappa$ and the average cavity photon number is related to the average photon flux of the laser as $\bar{n} = 4\bar{\dot{N}}/\kappa$, where $\kappa = \pi c/\mathcal{F}L$ is the cavity decay rate. It can then be shown that the force noise PSD from backaction is related to $S_{xx}^{\rm imp}$ as

$$S_{FF}^{\rm ba} = \frac{\hbar^2}{S_{xx}^{\rm imp}}. \tag{2.47}$$

From Eq. (2.45), it can be shown that the minimum achievable readout noise floor, referred to as the standard quantum limit (SQL), is

$$S_{FF}^{\rm noise,SQL} \equiv 2\hbar\left|\chi_{xF,m}\right|^{-1}, \tag{2.48}$$

which is achieved at a given frequency by tuning the cavity finesse $\mathcal{F}$, laser power P, or laser wavelength λ, so that $S_{FF}^{\rm ba} = \left|\chi_{xF,m}\right|^{-2} S_{xx}^{\rm imp} = \hbar\left|\chi_{xF,m}\right|^{-1}$.

2.3.3 Minimum detectable coupling strength

The detection capability of a prospective detector is typically characterized by the minimum detectable coupling strength $g'_{\rm min}$, which is often defined as the coupling strength for which the detector would achieve a signal-to-noise ratio (SNR) of one. To determine $g'_{\rm min}$, first one must calculate the minimum detectable force $F_{\rm min}$, which is defined as the force signal amplitude required to achieve SNR= 1.

[19] This relationship between $x_{\rm imp}$ and $\theta_{\rm imp}$ applies under the assumptions that the laser wavelength is resonant with the optical cavity and that the mechanical oscillations are slow compared to the inverse of the average photon lifetime within the cavity: $f \ll c/2L\mathcal{F}$.

The PSD of a signal is defined as[20]

$$S_{FF}(f) \equiv \lim_{\tau\to\infty} \frac{\left\langle \left|\tilde{F}_\tau(f)\right|^2 \right\rangle}{\tau} \tag{2.49}$$

where $\langle . \rangle$ is an expectation value and

$$\tilde{F}_\tau(f) \equiv \int_{-\tau/2}^{\tau/2} dt F(t) e^{-2\pi i f t} \tag{2.50}$$

is the finite-time Fourier transform.

In an experiment that involves measurement over a finite time $\tau_{\rm int}$, one cannot calculate the PSD directly. Instead, one calculates a periodogram, which is a finite-time estimate of the PSD, defined as

$$S_{FF,\tau_{\rm int}}(f) \equiv \frac{\left|\tilde{F}_{\tau_{\rm int}}(f)\right|^2}{\tau_{\rm int}}. \tag{2.51}$$

The SNR is defined as a ratio of the signal periodogram to the standard deviation in the noise periodogram SNR $= S^{\rm DM}_{FF,\tau_{\rm int}}/\Delta S^{\rm noise}_{FF,\tau_{\rm int}}$. However, for Gaussian noise statistics, the standard deviation in the noise floor is approximately as large as its mean [104], so the SNR can be approximated as

$$\text{SNR} \approx \frac{S^{\rm DM}_{FF,\tau_{\rm int}}}{S^{\rm noise}_{FF,\tau_{\rm int}}}. \tag{2.52}$$

Given the coherent signal from Eq. (2.35), the periodogram's magnitude at the signal frequency would be $S^{\rm DM}_{FF,\tau_{\rm int}} \approx {F_0}^2 \tau_{\rm int}/2$, which is calculated from Eqs. (2.51) and (2.50).

Prior to building a detector and making a measurement, the noise periodogram is not known. But one can construct a noise model and calculate the noise PSD, which then approximates the expected periodogram. Setting $S^{\rm noise}_{FF,\tau_{\rm int}} \approx S^{\rm noise}_{FF}$, the minimum detectable force is

$$F_{\rm min}(f) \approx \sqrt{\frac{2S^{\rm noise}_{FF}(f)}{\tau_{\rm int}}}. \tag{2.53}$$

---

[20] PSDs and Fourier transforms have so far been expressed in terms of angular frequency ω. It is sometimes more convenient to use frequency f. The amplitude of the PSD will then differ by 2π: $S(\omega) = S(f)/2\pi$. This doesn't affect the final result, which depends only of the ratio of PSDs.

Thus, given a coherent signal, $F_{\text{min}} \propto {\tau_{\text{int}}}^{-1/2}$, suggesting that longer measurement times grant access to weaker signals. However, this analysis applies only to a coherent, deterministic signal. As explained in Section 1.3.2, UDM is a stochastic field with a finite coherence time τ_{DM}. For measurement times less than the UDM coherence time, the field is coherent but has a stochastic amplitude, which can be accounted for in Eq. (2.53) by multiplying by a factor of 3 [65]. For measurement times longer than the UDM coherence time, the field can be treated as deterministic because the stochastic amplitude is effectively sampled many times, averaging out the randomness. However, the signal is no longer coherent, and it can be shown that $F_{\text{min}} \propto (\tau_{\text{DM}}\tau_{\text{int}})^{-1/4}$ [104]. To summarize,

$$F_{\text{min}}(f) \approx \sqrt{2S_{FF}^{\text{noise}}(f)} \times \begin{cases} 3{\tau_{\text{int}}}^{-1/2} & \tau_{\text{int}} \ll \tau_{\text{DM}} \\ (\tau_{\text{DM}}\tau_{\text{int}})^{-1/4} & \tau_{\text{int}} \gg \tau_{\text{DM}} \end{cases} \tag{2.54}$$

To bridge the two time-scaling regimes ($\tau_{\text{int}} \ll \tau_{\text{DM}}$ and $\tau_{\text{int}} \gg \tau_{\text{DM}}$) with a smooth function, the following expression is used for the minimum detectable force:

$$F_{\text{min}}(f) \approx \sqrt{2S_{FF}^{\text{noise}}(f)}\left[3{\tau_{\text{int}}}^{-1/2} + (\tau_{\text{DM}}\tau_{\text{int}})^{-1/4}\right]. \tag{2.55}$$

From Eq. (2.36), the minimum detectable coupling strength is

$$g'_{\text{min}}(f) = \frac{F_{\text{min}}(f)}{\alpha_m F_{\text{DM},0}}. \tag{2.56}$$

The minimum detectable coupling strength g'_{min} from this example UDM search using a resonant mechanical system is plotted in Fig. 2.4, assuming that $F_{\text{DM},0}$ is frequency independent,[21] and that $\tau_{\text{int}} \gg \tau_{\text{DM}}$. The red shading represents the regions of UDM parameter space that would be probed by such an experiment, or have been ruled out if the experiment had already been conducted and not detected a UDM signal.

2.4 Fifth Forces

In this dissertation, it is assumed that dark matter is composed of hypothetical scalar or vector particles beyond the Standard Model. But it is important to note that these particles

[21] $F_{\text{DM},0}$ is not generally frequency independent. For example, the amplitude of the vector UDM force in Eq. (2.19) doesn't depend on the DM frequency ω_{DM}. However, the amplitude of the scalar UDM strain in Eq. (2.34) does depend on ω_{DM}.

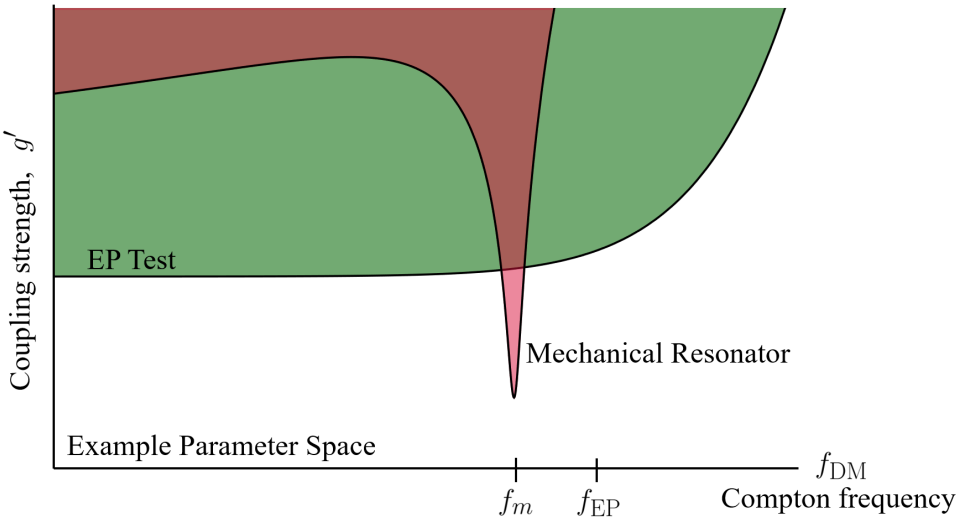

Figure 2.4: Example UDM parameter space with constraints: The g'_{min} curves are included from the example UDM search with a mechanical resonator in Section 2.3 and the example EP test in Section 2.4.3. The resonance frequency f_m of the mechanical resonator is marked; also marked is the frequency f_{EP}, which is the Compton frequency for which the interaction length equals the EP test length scale. The plot is on a log-log scale. In an experiment, g'_{min} is not measured directly, but is inferred from an experimental observable. For example, the experimental observable in an optomechanical experiment with an interferometric readout system would be the measured photocurrent.

may exist even if they are not dark matter. Their existence can be tested with experiments searching for fifth forces, without considering dark matter at all. The term "fifth force" refers to a fundamental force, like the strong, weak, electromagnetic, and gravitational forces, that has not yet been discovered. If any of these scalar or vector particles exist, they would mediate a fifth force (analogous to how photons mediate the electromagnetic force between electrically charged objects).

The parameter space for the UDM candidates considered in this dissertation is most strongly constrained by fifth force experiments (often referred to as EP tests[22]). These experiments seek to measure a fifth force between stationary objects. The corresponding analogy

[22] These experiments are often called equivalence principle (EP) tests. The stated purpose of EP tests is to test the equivalence principle by searching for a material-dependence in the acceleration due to gravity. Another paradigm is to view these experiments as searches for

to electromagnetism is a measurement of the Coulomb force between electrically charged objects. To better understand these constraints, it will be shown how scalars and vectors mediate a force between charged particles.

In Section 2.4.1 the static field sourced by a stationary point particle is derived. In Section 2.4.2 an explanation is given for how this field results in a force between point particles. In Section 2.4.3 EP tests and their constraints on the UDM parameter space are discussed.

The analyses presented in this section are more general than the dark matter models in Sections 2.1 and 2.2. Although the fields are not being considered as dark matter, the subscripts $()_{\rm DM}$ continue to be used to maintain consistent notation.

2.4.1 Static field sourced by stationary point charge

As an example, consider a scalar field φ which couples to electrons. From Eqs. (2.20) and (2.24), the relevant terms in the Lagrangian density are

$$\mathcal{L} \supset \frac{c^4}{4\pi G}\left[\frac{1}{2}\partial_\mu\varphi\partial^\mu\varphi - \frac{1}{2}\left(\frac{m_{\rm DM}c}{\hbar}\right)^2\varphi^2\right] - d_{m_e}\varphi m_{e,0}c^2\bar{\psi}_e\psi_e. \tag{2.57}$$

To calculate the scalar field sourced by an electron, the Euler-Lagrange equations (2.21) can be applied with respect to φ while treating the electron as a point charge that is stationary at the origin: $\bar{\psi}_e\psi_e = \delta(\boldsymbol{r})$. The resulting field will also be stationary, so time derivatives of φ can be ignored. The equation of motion is found to be

$$-\nabla^2\varphi + \left(\frac{m_{\rm DM}c}{\hbar}\right)^2\varphi = -d_{m_e}\frac{4\pi G m_{e,0}}{c^2}\delta(\boldsymbol{r}). \tag{2.58}$$

This differential equation can be solved by applying the Fourier transform, yielding the solution [23]

$$\varphi(\boldsymbol{r}) = -d_{m_e}\frac{G m_{e,0}}{c^2}\frac{e^{-r/\lambda\!\!\!^{-}{}^{\rm C}_{\rm DM}}}{r}. \tag{2.59}$$

material-dependent fifth forces, as they would not be able to distinguish between a material-dependent fifth force and an EP violation.

[23] $\lambda\!\!\!^{-}{}^{\rm C}_{\rm DM} = \hbar/m_{\rm DM}c$ is the reduced Compton wavelength. The Yukawa potential decreases rapidly with r when $r > \lambda\!\!\!^{-}{}^{\rm C}_{\rm DM}$, which is why $\lambda\!\!\!^{-}{}^{\rm C}_{\rm DM}$ is also frequently referred to as the "interaction length."

For the vector field described by Eq. (2.3), the field can be solved for in the same way by assuming the four-current to be described by[24] $J^0 = cq'\delta(\boldsymbol{r})$ and $J^i = 0$, which results in

$$V'(\boldsymbol{r}) = \frac{q'}{4\pi\epsilon'}\frac{e^{-r/\lambda\!\!\!^{-\,\mathrm{C}}_{\mathrm{DM}}}}{r}. \tag{2.60}$$

Generally, a potential of the form $V(\boldsymbol{r}) \propto \frac{e^{-r/\lambda\!\!\!^{-\,\mathrm{C}}_{\mathrm{DM}}}}{r}$ is called a "Yukawa potential." Note that for massless fields ($\lambda\!\!\!^{-\,\mathrm{C}}_{\mathrm{DM}} \to \infty$), a Yukawa potential will reduce to the form of a Coulomb potential. However, in the scalar case, it remains to be shown that φ exerts a force on another charged particle.

2.4.2 Force exerted on charged objects

The fact that a vector field exerts a force on a charged particle is not surprising given the strong analogy to electromagnetism. Using the Yukawa potential from Eq. (2.60) with Eqs. (2.8) and (2.7), the force between two stationary point particles is found to be

$$\boldsymbol{F}(\boldsymbol{r}) = \frac{q'_1 q'_2}{4\pi\epsilon'}\left(1 + \frac{r}{\lambda\!\!\!^{-\,\mathrm{C}}_{\mathrm{DM}}}\right)\frac{e^{-r/\lambda\!\!\!^{-\,\mathrm{C}}_{\mathrm{DM}}}}{r^2}\hat{\boldsymbol{r}}.$$

or, using Eqs. (2.16) and (2.17),

$$\boldsymbol{F}(\boldsymbol{r}) = g'^2\frac{N'_1 N'_2 e^2}{4\pi\epsilon_0}\left(1 + \frac{r}{\lambda\!\!\!^{-\,\mathrm{C}}_{\mathrm{DM}}}\right)\frac{e^{-r/\lambda\!\!\!^{-\,\mathrm{C}}_{\mathrm{DM}}}}{r^2}\hat{\boldsymbol{r}}. \tag{2.61}$$

Scalar fields can also exert a force on charged particles. The scalar force can be explained by considering the effect of a scalar field on a particle's rest energy. From Eq. (2.27), the rest energy of an electron in the presence of a static scalar field is

$$E_{\mathrm{rest}}(\boldsymbol{r}) = m_e(\boldsymbol{r})c^2 = \left(1 + d_{m_e}\varphi(\boldsymbol{r})\right)m_{e,0}c^2. \tag{2.62}$$

The energy has a spatial dependence, which means the electron experiences an external force

$$F(\boldsymbol{r}) = -\nabla E_{\mathrm{rest}}(\boldsymbol{r}) = -d_{m_e}m_{e,0}c^2\nabla\varphi(\boldsymbol{r}). \tag{2.63}$$

[24] See Appendix A.2.1 for the definition of the four-current density components.

Given the field solution of Eq. (2.59), the force between two stationary electrons due to a scalar field is

$$\boldsymbol{F}(\boldsymbol{r}) = -{d_{m_e}}^2 {m_{e,0}}^2 G \left(1 + \frac{r}{\lambda\!\!\!^{-}{}^{\mathrm{C}}_{\mathrm{DM}}}\right) \frac{e^{-r/\lambda\!\!\!^{-}{}^{\mathrm{C}}_{\mathrm{DM}}}}{r^2} \hat{\boldsymbol{r}}. \tag{2.64}$$

To get the force between macroscopic objects, multiply Eq. (2.64) by the number of electrons in each object, resulting in a force with form similar to Eq. (2.61).

2.4.3 EP tests in the search for UDM

Figure 2.5 illustrates a general EP test, where a test mass M sources a static field, resulting in a Yukawa potential and exerting a static force on the test masses m_1 and m_2, which are made of different materials.[25] An EP test is designed to detect material-dependent fifth forces, which would manifest as a differential force $\Delta F = F_1 - F_2$. As in Section 2.3, a vector field is assumed. But this analysis can be easily applied to scalar fields.

Treating the test and source masses as point particles, the force between them due to the vector field is given by Eq. (2.61). If the minimum detectable differential force in this experiment is ΔF_{min}, and $\Delta N'_m$ is the difference in the number of charges in the test masses, the minimum detectable coupling strength for the experiment is

$$g'_{\mathrm{min}} = \sqrt{\frac{4\pi\epsilon_0}{e^2} \frac{\Delta F_{\mathrm{min}}}{N'_M \Delta N'_m}} \left[\left(1 + \frac{r}{\lambda\!\!\!^{-}{}^{\mathrm{C}}_{\mathrm{DM}}}\right) \frac{e^{-r/\lambda\!\!\!^{-}{}^{\mathrm{C}}_{\mathrm{DM}}}}{r^2}\right]^{-1/2}. \tag{2.65}$$

This can be re-expressed in terms of the Compton frequency $f_{\mathrm{DM}} = c/2\pi\lambda\!\!\!^{-}{}^{\mathrm{C}}_{\mathrm{DM}}$ as

$$g'_{\mathrm{min}} = \sqrt{\frac{4\pi\epsilon_0}{e^2} \frac{\Delta F_{\mathrm{min}}}{N'_M \Delta N'_m}} \left[\left(1 + \frac{f_{\mathrm{DM}}}{f_{\mathrm{EP}}}\right) \frac{e^{-f_{\mathrm{DM}}/f_{\mathrm{EP}}}}{r^2}\right]^{-1/2}, \tag{2.66}$$

where $f_{\mathrm{EP}} \equiv c/2\pi r$ is defined as the Compton frequency at which the interaction length equals the separation distance $\left(\lambda\!\!\!^{-}{}^{\mathrm{C}}_{\mathrm{DM}} = r\right)$.

Figure 2.4 includes the minimum detectable coupling strength, in terms of the Compton frequency, for an example EP test. The shape of the curve is noticeably different from

[25] In an actual EP test, the position of the source mass will be modulated at a known frequency, resulting in an oscillating force, as opposed to the static force assumed in this idealized example. However, this won't impact the analysis.

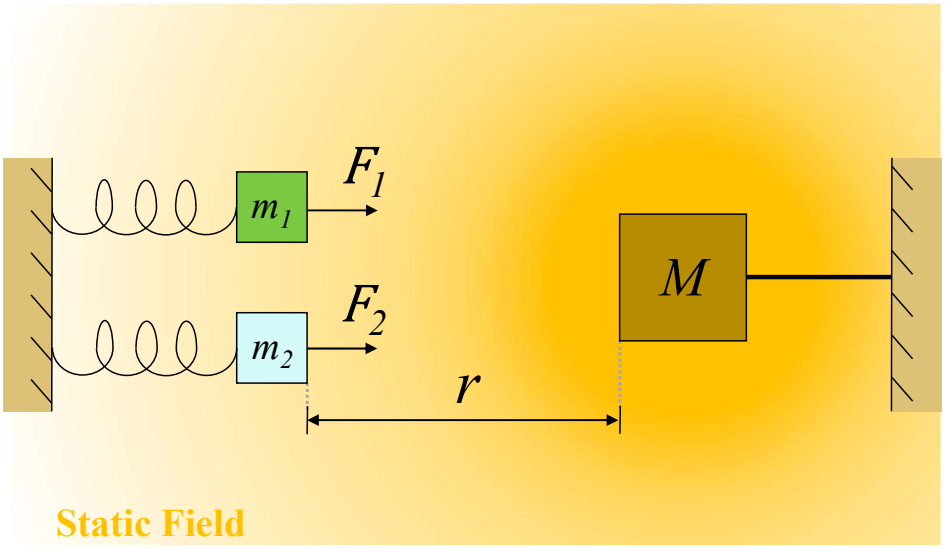

Figure 2.5: Example EP test experiment: A source mass M establishes a static field (in yellow), which exerts fifth forces F_1 and F_2 on the (typically much smaller) test masses m_1 and m_2. The test masses are composed of different materials to search for material-dependent fifth forces.

the mechanical resonator-based direct UDM search example from Section 2.3. When the interaction length greatly exceeds the separation distance,[26] the expression simplifies to

$$g'_{\rm min} \approx \sqrt{\frac{4\pi\epsilon_0}{e^2}\frac{\Delta F_{\rm min}}{N'_M \Delta N'_m}}\, r, \tag{2.67}$$

which is independent of $\lambda\!\!\!^{-}{}^{\rm C}_{\rm DM}$ (or $f_{\rm DM}$). So EP test constraints are constant at low Compton frequencies. At small interaction lengths, $g'_{\rm min}$ increases rapidly. These properties of EP test constraints are illustrated in Fig. 2.4, where it can be seen that $g'_{\rm min}$ increases rapidly at frequencies above $f_{\rm EP}$.

Here, the test and source masses have been treated as point particles. However, the shape of all EP test constraints generally resembles that of this simple example. Even for extended and more complicated charge distributions, $g'_{\rm min}$ is constant at low Compton frequencies, and increases as the interaction length becomes shorter than the relevant experimental length scales.

[26] $\lambda\!\!\!^{-}{}^{\rm C}_{\rm DM} \gg r$ or, equivalently, $f_{\rm DM} \ll f_{\rm EP}$

2.5 Current status of the UDM search

The status of any UDM search can be summarized with a parameter space plot, like the example plot in Fig. 2.4. In this section, the parameter space is presented for each of the specific UDM candidates considered in this dissertation:

- Figure 2.6: Vector particles coupled to $B - L$ (baryon minus lepton number)
- Figure 2.7: Vector particles coupled to B (baryon number)
- Figure 2.8: Scalar particles coupled to photons
- Figure 2.9: Scalar particles coupled to electrons

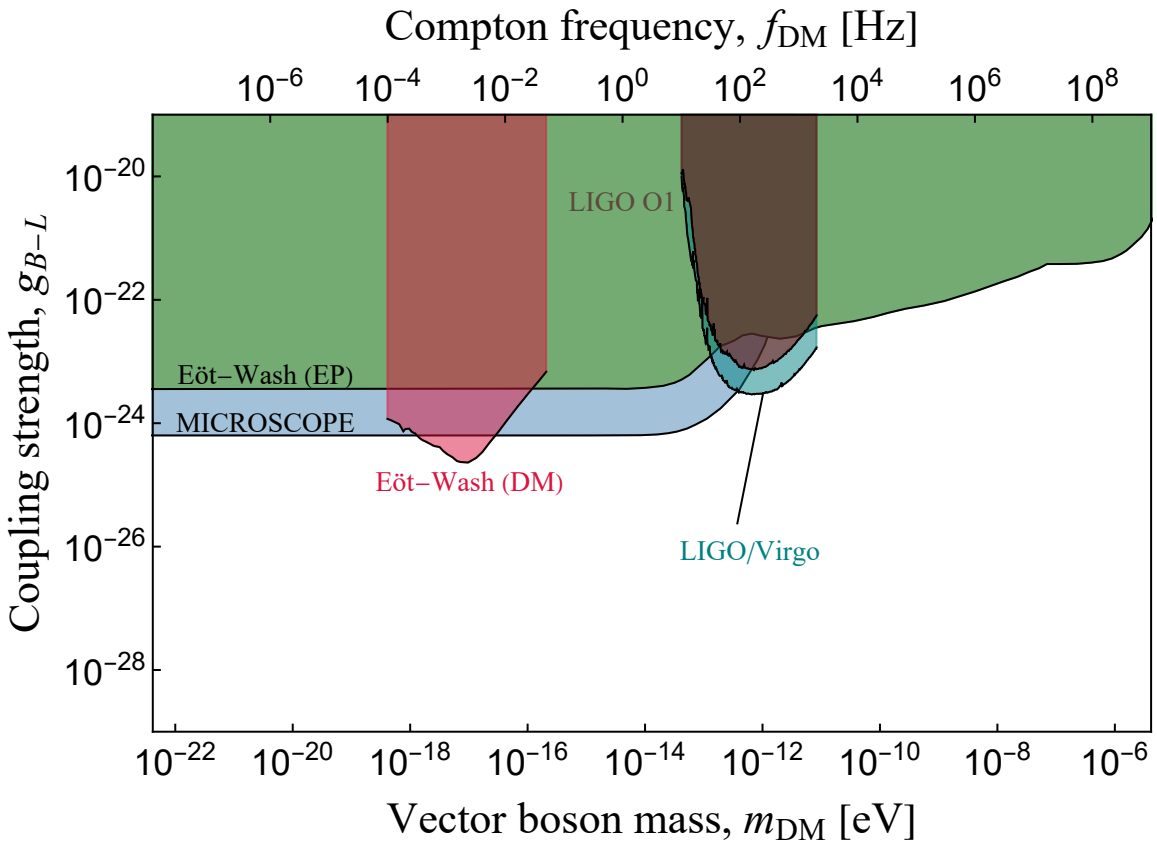

Figure 2.6: Vector $B - L$ parameter space: Upper bounds on g_{B-L} come from EP tests [6, 7, 8] and UDM direct detection experiments [9, 10, 11]. The parameter space that has been explored by each experiment is denoted by the shaded regions. Figure adapted from Ref. [5].

2.5.1 Vector UDM parameter space

As discussed in Section 2.1, vector UDM with direct couplings $B - L$ or B charge is described by the Lagrangrian density term

$$\mathcal{L}_{\text{interaction}} = -J'^{\nu} A'_{\nu},$$

where the current J'^{ν} corresponds to either $B - L$ or B.

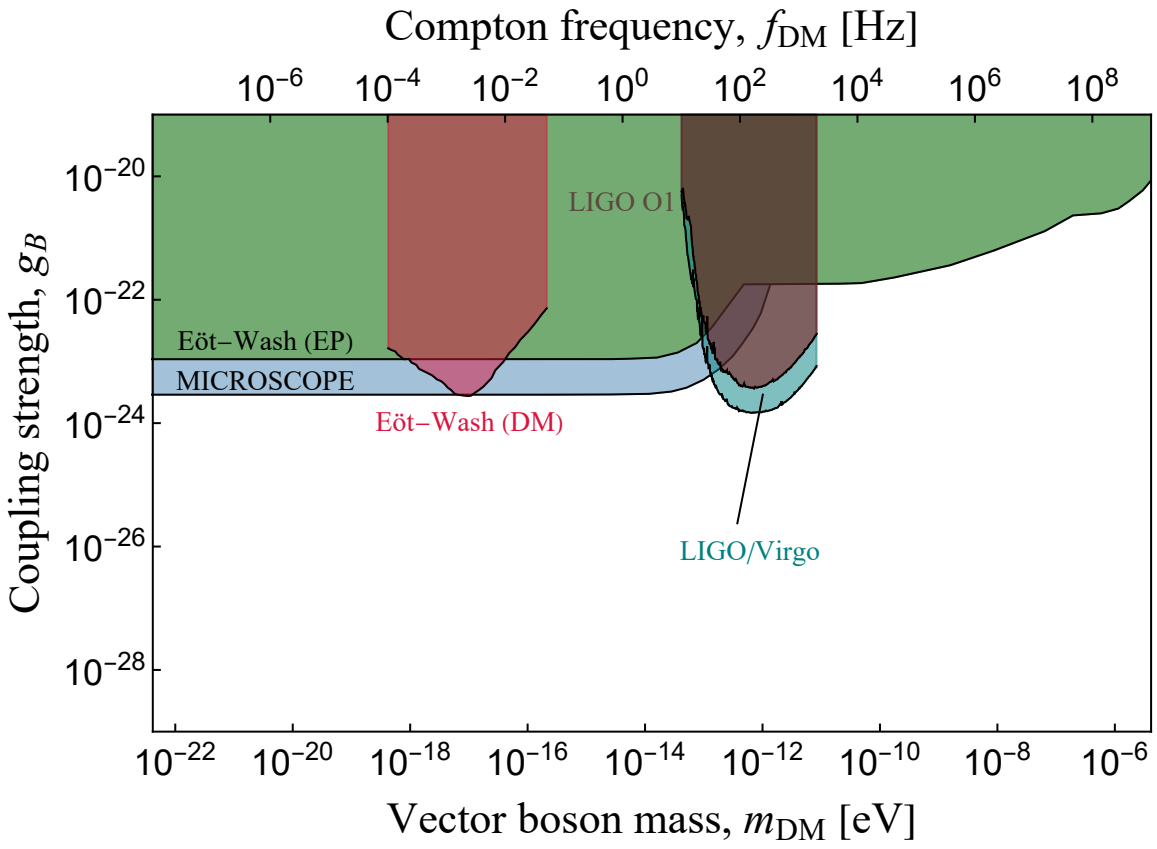

Figure 2.7: Vector B parameter space: Upper bounds on g_B come from EP tests [6, 7, 8] and UDM direct detection experiments [9, 10, 11].

The parameter spaces of both vector $B - L$ (Fig. 2.6) and vector B (Fig. 2.7) UDM are constrained by the same experiments. The broadest constraints come from EP tests, including the MICROSCOPE satellite mission [6, 7] and torsion balance experiments from the Eöt-Wash Group [8]. Additional constraints come from DM direct-detection experiments, including the Eöt-Wash torsion balance DM search [9], repurposed data from LIGO's first

observing run [10], and combined constraints from the data taken during the third observing run of LIGO and VIRGO [11].

In Chapter 3, silicon nitride optomechanical membranes are proposed to search for vector $B-L$ and B UDM in the 10^{-11} – 10^{-9} eV/c^2 mass range (frequency: 10^3 – 10^5 Hz).

2.5.2 Scalar UDM parameter space

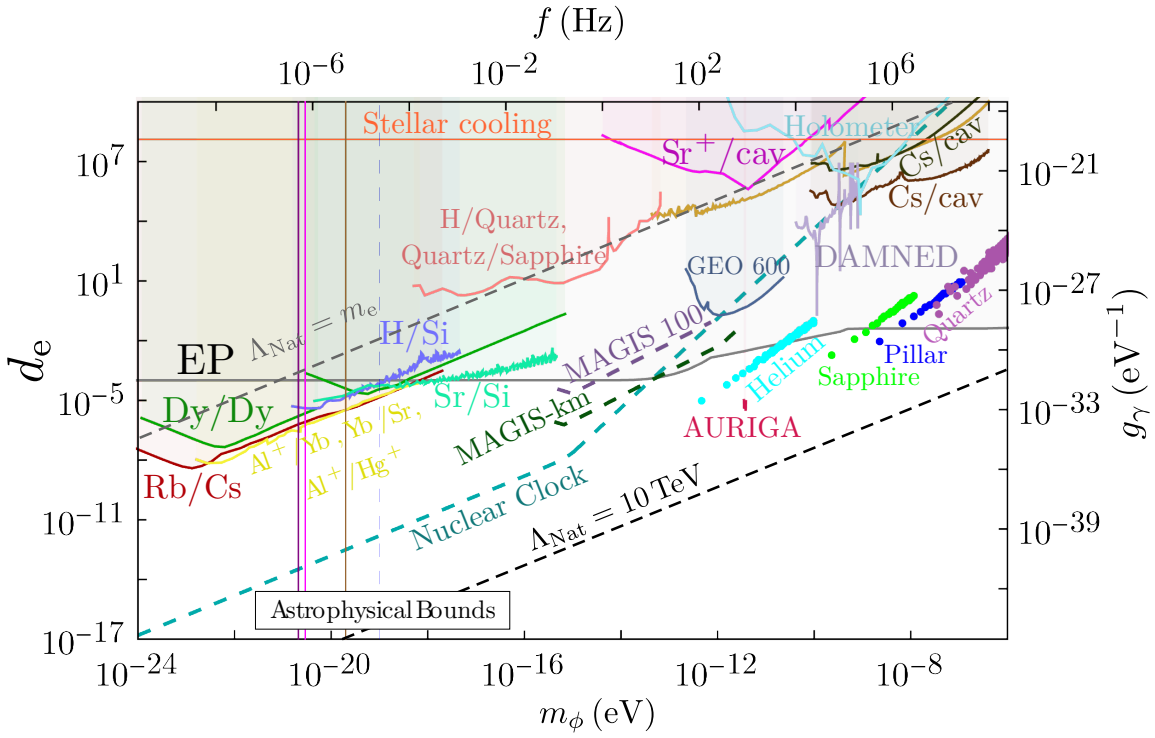

Figure 2.8: Scalar d_e parameter space: Solid lines indicate upper bounds on d_e, which come from EP tests [6, 7, 8, 12, 13, 14], UDM direct-detection experiments [15, 16, 17, 18, 19, 20, 21, 22, 23, 24, 25, 26, 27], and measurements of stellar cooling [28]. Dashed lines indicate proposed experiments [19, 29, 30, 31, 32, 33] and natural values for d_e [5, 34]. Vertical lines indicate astrophysical lower bounds on the DM mass [35, 36, 37, 38, 39, 40, 41]. Figure from Ref. [5]. Image credit: Abhishek Banerjee.

As discussed in Section 2.2, scalar UDM with a direct coupling to photons is described by the Lagrangrian density term

$$\mathcal{L}_{\rm interaction} = d_e \varphi \frac{e^2 c}{16\pi\hbar\alpha_0} F_{\mu\nu}F^{\mu\nu},$$

and a direct coupling to electrons is described by the term

$$\mathcal{L}_{\text{interaction}} = -d_{m_e}\varphi m_{e,0}c^2\bar{\psi}_e\psi_e.$$

Scalar UDM with these couplings would effect an oscillation in fine-structure constant α and electron mass m_e, respectively (see Section 2.2.2). Oscillations in α and m_e produce measurable effects such as modulation of atomic energy levels [30], mechanical strains [67], and modulation of the refractive index of optical materials [71]. These effects can be searched for with a wide variety of detector types from atomic experiments to gravitational wave interferometers [5]. The parameter spaces for scalar UDM coupling to photons d_e and electrons d_{m_e} are plotted in Figs. 2.8 and 2.9.

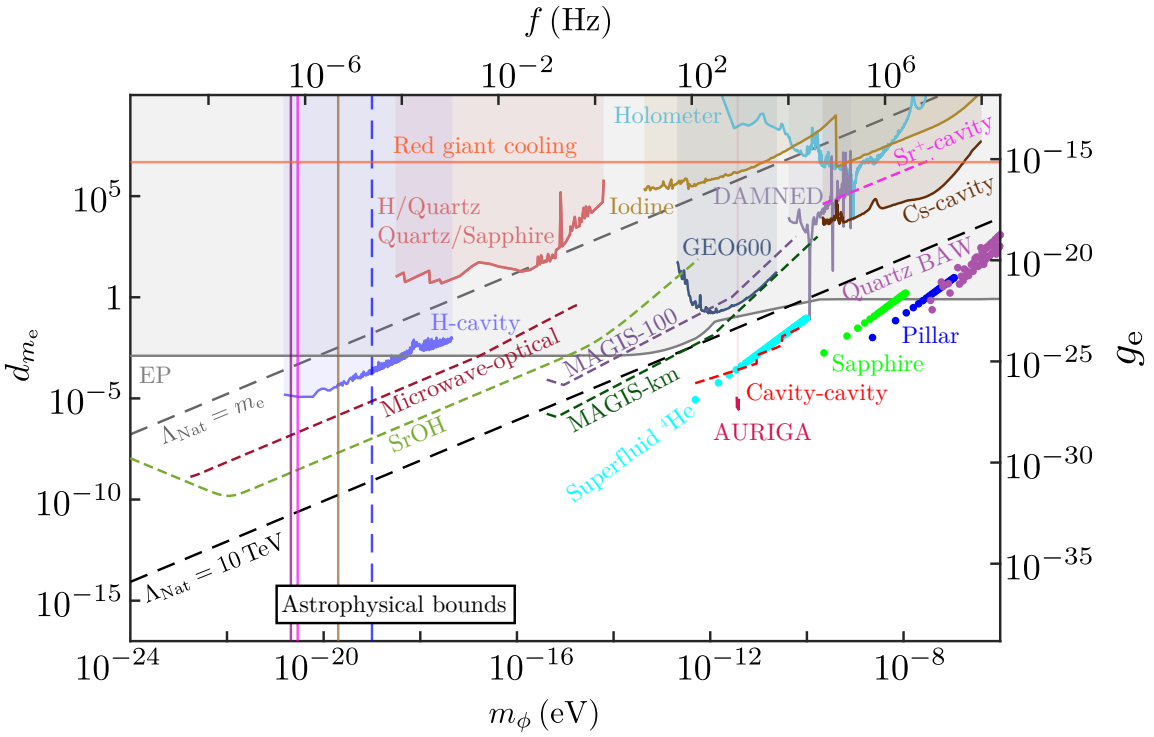

Figure 2.9: Scalar d_{m_e} parameter space: Solid lines indicate upper bounds on d_{m_e}, which come from EP tests [6, 7, 8, 12, 13, 14], UDM direct-detection experiments [18, 20, 22, 23, 24, 25, 26, 27], and measurements of red giant cooling [28]. Dashed lines indicate proposed experiments [29, 33] and natural values for d_{m_e} [5, 34]. Vertical lines indicate astrophysical lower bounds on the DM mass [35, 36, 37, 38, 39, 40, 41]. Figure from Ref. [5]. Image credit: Tejas Deshpande.

As with vector UDM, significant constraints come from the MICROSCOPE [6, 7, 14] and Eöt-Wash [8, 12, 13] EP tests. Additional constraints come from the diverse set of existing UDM direct-detection experiments, including atomic clocks [16, 17, 18], comparisons of atomic clocks with optical cavities [18, 19, 21, 22], acoustic cavities [20], atomic and molecular spectroscopy [15, 23], repurposed gravitational wave detectors [24, 25, 27], and optical interferometry [26].

Also included in Figs. 2.8 and 2.9 are projected constraints from proposed future experiments, such as atom interferometry [29], nuclear clocks [5], mechanical resonators (covered in this dissertation) [33], comparison of microwave and optical atomic clocks [30], molecular spectroscopy [31], comparison of atomic clocks with optical cavities [19], and comparison of two different optical cavities [32].

In Chapter 4, compact mechanical resonators are proposed to search for scalar UDM in the 10^{-12} – 10^{-6} eV/c^2 mass range (frequency: 10^{2} – 10^{8} Hz). Results from this proposal are also included in Figs. 2.8 and 2.9 as: "Superfluid ^{4}He," "Sapphire," "Pillar," and "Quartz BAW." In Chapter 5, an optical fiber-based detector is proposed to search for scalar UDM in the 10^{-17} – 10^{-13} eV/c^2 mass range (frequency: 10^{-3} – 10^{1} Hz).

Chapter 3

PROPOSAL OF A VECTOR UDM SEARCH WITH AN OPTOMECHANICAL ACCELEROMETER

In this chapter, silicon nitride (Si_3N_4) membrane optomechanical accelerometers are proposed as detectors for vector UDM. The material in this chapter was adapted from Ref. [42], *Searching for vector dark matter with an optomechanical accelerometer*, Jack Manley and others; Phys. Rev. Lett. **126**, 061301 (2021). Reproduced here with permission, ©2021 American Physical Society.

Vector UDM coupled to the $B - L$ ("baryon minus lepton") or B (baryon) charge exerts an oscillating force on normal matter, as described in Section 2.1. The force on an object is generally proportional to its mass, with the constant of proportionality being determined by the object's material composition. Thus, the signal in a vector UDM experiment is a material-dependent acceleration. Here, the prospect of searching for vector UDM with optomechanical accelerometers is considered. The concept of accelerometer-based UDM detection is well-established [66, 72, 105], forming the basis for searches based on gravitational wave interferometer [43], atom interferometer [106], and precision torsion-balance experiments [9, 72]. However, this chapter emphasizes that optomechanical accelerometers can also be operated resonantly, enabling high sensitivity at frequencies (1 - 100 kHz) where current broadband UDM searches are limited, with a compact form-factor that is amenable to array-based detection [66].

A detector is proposed based on a Si_3N_4 membrane fixed to a beryllium (Be) mirror, forming a Fabry-Pérot cavity. The use of different materials enables sensitivity to DM-induced accelerations. Through a combination of high mechanical quality factor, cryogenic cooling, and cavity-enhanced optical readout, it is found that this detector can begin improving upon the current bounds on the vector UDM coupling strength in an integration time of

minutes, over a fractional bandwidth of $\sim 0.1\%$. Addressing challenges such as frequency tunability (to increase bandwidth) and scalability could enable these and similar optomechanical detectors to cover a large frequency range in the vector UDM parameter space.

This chapter is outlined as follows:

- Section 3.1 focuses on the vector UDM signal and how it excites vibrations in a membrane. The result is Eq. (3.18), which describes the membrane's displacement (PSD) due to the force exerted on it by UDM.
- The purpose of Section 3.2 is to explain Figs. 3.2 and 3.3, which can be considered the result of this work. The figures show the expected sensitivity to vector UDM from the proposed optomechanical membranes in comparison to constraints from previous experiments.
- Section 3.3 briefly summarizes the chapter.

3.1 Optomechanical membranes as DM detectors

3.1.1 Material-dependent acceleration signal

As discussed in Section 2.1, vector UDM coupled to $B-L$ or B charge[1] exerts a force on an object[2]

$$F_{\mathrm{DM}}(t) \approx g' N' F_{\mathrm{DM},0} \cos\left(\omega_{\mathrm{DM}} t\right), \tag{3.1}$$

where g' is the coupling strength, N' is the number of dark charges within the object, and the amplitude $F_{\mathrm{DM},0}$ is a stochastic quantity with root-mean-square value

$$F_{\mathrm{DM,rms}} = \sqrt{2\frac{e^2\rho_{\mathrm{DM}}}{\epsilon_0}}. \tag{3.2}$$

In the case of $B-L$-coupling, the number of charges within a single atom is the difference in the mass number A and atomic number Z. For a homogeneous object k of total mass m_k, the number of $B-L$ charges is

$$N_{B-L,k} = \frac{A_k - Z_k}{m_{\mathrm{amu},k} m_n} m_k, \tag{3.3}$$

[1] Atomic matter is composed of protons (baryon), neutrons (baryon), and electrons (leptons).

[2] Over timescales less than the coherence time τ_{DM} and length scales less than the de Broglie wavelength λ_{DM}; see Section 1.3.2. The omitted phase θ_{DM} does not impact the final result.

where $m_{\rm amu}$ is the atomic mass in atomic mass units, and m_n is the mass of a nucleon. It is evident from Eq. (3.3) that the UDM force on an object is proportional to its mass, and the proportionality depends on the atomic or molecular species. Thus, the signal is best characterized as a material-dependent acceleration

$$a_{{\rm DM},k}(t) \approx g_{\text{B-L}} \frac{A_k - Z_k}{m_{{\rm amu},k}} a_{\rm DM,0} \cos\left(\omega_{\rm DM} t\right), \tag{3.4}$$

where $a_{\rm DM,0} \equiv F_{\rm DM,0}/m_n$ ($a_{\rm DM,rms} \equiv F_{\rm DM,rms}/m_n$). Experiments are not often sensitive to an object's absolute acceleration, but rather a differential acceleration between a test object and a reference object. It is important for a vector UDM experiment to use two objects made of different materials. A simple optomechanical accelerometer is illustrated in Fig. 3.1, where an optical cavity is formed by end mirrors on a reference mass with charge q_1 and a test mass with charge q_2, which are attached by a spring to form a mechanical resonator. The differential acceleration signal is

$$\Delta a_{\rm DM}(t) \equiv a_{\rm DM,2}(t) - a_{\rm DM,1}(t) \approx g' \Delta_{12} a_{\rm DM,0} \cos\left(\omega_{\rm DM} t\right). \tag{3.5}$$

The differential acceleration is suppressed relative to the absolute acceleration of either mass by a dimensionless factor Δ_{12}, which represents the difference in charge-to-mass ratio of the reference and test masses. For coupling to $B - L$,

$$\Delta_{12} = \frac{A_2 - Z_2}{m_{\rm amu,2}} - \frac{A_1 - Z_1}{m_{\rm amu,1}}, \tag{3.6}$$

so Δ_{12} is primarily due to the difference in relative neutron fraction.

The acceleration due to B-coupling is also material dependent, where the charge is proportional to the mass number A_k, so that

$$\Delta_{12} = \frac{A_1}{m_{\rm amu,2}} - \frac{A_2}{m_{\rm amu,1}}. \tag{3.7}$$

Here, Δ_{12} comes primarily from the difference in nuclear binding energy. Generally, the reference and test mass materials are chosen to maximize the quantity Δ_{12} for a given vector coupling, in order to maximize the differential acceleration signal $\Delta a_{\rm DM}$.

Note that the polarization of the vector UDM field may not always align with the detector's preferred axis. The differential acceleration in Eq. (3.5) can be modified to account

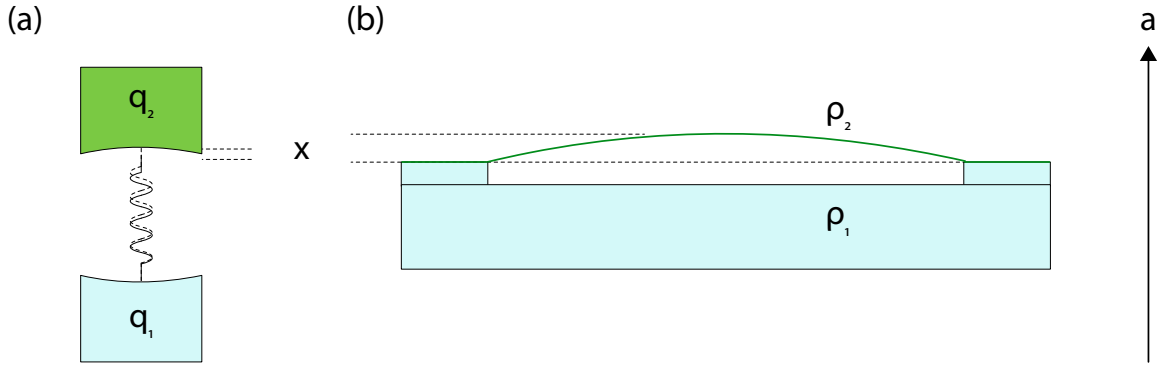

Figure 3.1: Concept for an optomechanical accelerometer sensitive to vector UDM: (a) Lumped mass model. (b) Membrane-mirror example. Colors represent masses (materials) with different B or B-L charge (charge density), q_k (ρ_k). Differential acceleration leads to a measurable relative displacement between the masses. Figure from Ref. [42] ©2021 American Physical Society.

for the random polarization of the vector UDM field, which will vary on timescales comparable to the UDM coherence time $\tau_{\rm DM}$ [72]. In the Supplemental Material from Ref. [42] it is shown that, for a sufficiently long measurement, this can be accounted for by dividing by a factor of $\sqrt{3}$:

$$\Delta a_{\rm DM}(t) \approx \frac{g' \Delta_{12} a_{\rm DM,0}}{\sqrt{3}} \cos\left(\omega_{\rm DM} t\right). \tag{3.8}$$

This polarization-averaged differential acceleration is the signal in a vector UDM search.

3.1.2 Optomechanical membrane accelerometer

The subject of this work is the system sketched in Fig. 3.1b, which consists of a Si_3N_4 membrane rigidly attached to a beryllium mirror.[3] The use of different materials is necessary to ensure that the suppression factor Δ_{12} is non-zero.[4] The system must also be placed in free-fall. This can be simulated, for example, by suspending the device from a pendulum with resonance frequency much below the mechanical resonance frequency of the detector.

[3] Beryllium mirrors have been used in cryogenic settings, for example, in the James Webb Space Telescope [107].

[4] For a Si_3N_4-Be system, $(\Delta_{12})_{B-L} = 0.053$ and $(\Delta_{12})_B = 0.0018$.

Optomechanical systems [75] provide numerous platforms for realizing sensitive accelerometers, such as levitated particles [108] or whispering gallery mode resonators [109]. Here, the use of Si_3N_4 membranes as resonant optomechanical accelerometers is motivated by their ability to achieve high mechanical quality factors [110, 111], frequency-tunable mechanical resonances [84, 85, 112, 113], and high reflectivity in order to function as the end mirror of an optical cavity [114, 115].

In order to determine how the vector UDM signal will couple to a membrane, one first needs to determine the membrane's mechanical vibration modes. Consider a homogeneous square membrane on the y-z plane with side lengths L and thickness h. The membrane is centered on the origin so that its edges lie at $y = \pm L/2$ and $z = \pm L/2$. Let $u(t, y, z)$ be the transverse (in the x-direction) displacement field of the membrane with respect to its frame. The displacement field obeys a 2D wave equation

$$\ddot{u} = {v_s}^2 \nabla^2 u, \tag{3.9}$$

where v_s is the speed of transverse waves. The total displacement field can be expanded in terms of the eigenmodes $u(t, y, z) = \sum_{ij} x_{ij}(t) u_{ij}(y, z)$, where x_{ij} gives the amplitude and temporal phase of the oscillation while u_{ij} is the dimensionless, normalized spatial distribution (or modeshape). The modeshape can be further decomposed as $u_{ij}(y, z) = u_i(y) u_j(z)$. The modes are orthogonal $\left(\iint dy dz\, u_{ij} u_{mn} \propto \delta_{im}\delta_{jn}\right)$ with normalization chosen such that $\left|u_{ij}\right|_{\max} = 1$. The membrane is attached to its frame, imposing rigid boundary conditions on the displacement field: $u_i(\pm L/2) = u_j(\pm L/2) = 0$. The mode solutions are

$$\begin{aligned} u_i(y) &= \cos\left(\frac{i\pi y}{L} - \frac{\pi}{4}\left(1 + (-1)^i\right)\right) \\ u_j(z) &= \cos\left(\frac{j\pi z}{L} - \frac{\pi}{4}\left(1 + (-1)^j\right)\right), \end{aligned} \tag{3.10}$$

with (angular) resonance frequencies

$$\omega_{ij} = \frac{\pi v_s}{L}\sqrt{i^2 + j^2}. \tag{3.11}$$

Each mode can be further characterized by an effective mass, defined as $\mu_{ij} \equiv \iiint dV\rho \left(u_{ij}\right)^2$ [116]. For a membrane with uniform mass density ρ and the modes given by Eqs. (3.10), the effective mass ends up being mode-independent,

$$\mu_{ij} = \frac{\rho h L^2}{4} \equiv \mu_m \tag{3.12}$$

3.1.3 DM-coupling to membrane mechanical modes

The DM signal manifests as a spatially uniform acceleration, affecting the displacement field as $\ddot{u}_{\rm DM}(t, y, z) = \Delta a_{\rm DM}(t)$. This driving term can be included into the wave equation (3.9) to get the equation of motion for a membrane that is driven by the vector UDM field

$$\ddot{u} - {v_s}^2 \nabla^2 u = \Delta a_{\rm DM}. \tag{3.13}$$

Expanding the displacement field in terms of its eigenmodes yields

$$\sum_{ij} \left(\ddot{x}_{ij} u_{ij} + \omega_{ij}^2 x_{ij} u_{ij}\right) = \Delta a_{\rm DM}. \tag{3.14}$$

Multiplying both sides of Eq. (3.14) with the operator $\iiint dV u_{ij}$, one can reduce the equation of motion to the form of a driven harmonic oscillator[5] for each mechanical mode[6]

$$\ddot{x}_{ij} + \gamma_{ij}\dot{x}_{ij} + \omega_{ij}^2 x_{ij} = \alpha_{ij}\Delta a_{\rm DM}. \tag{3.15}$$

The strength of the coupling between the acceleration signal and the ij mode is characterized by the overlap factor,

$$\alpha_{ij} \equiv \frac{\iiint dV\, u_{ij}}{\iiint dV\, u_{ij}^2}. \tag{3.16}$$

From the mode solutions in Eqs. (3.10), the overlap factors are found to be

$${\alpha_{ij}}^2 = \left(\frac{4}{\pi}\right)^4 (ij)^{-2} \sin^2\left(\frac{i\pi}{2}\right) \sin^2\left(\frac{j\pi}{2}\right), \tag{3.17}$$

---

[5] Mechanical dissipation $\gamma_{ij} = \omega_{ij}/Q_m$ has been introduced a posteriori, assuming a mode-independent quality factor $Q_{ij} \equiv Q_m$.

[6] Frequency degeneracies exist for different sets of (i, j), and are implicit in the summations $\sum_{ij}$. The existence of these degeneracies improves the sensitivity (see Eq. (3.24)) at degenerate resonances. However, in practice, true degeneracies are difficult to achieve in high-Q sensors due to local inhomogeneities in density and stress.

which is zero when either i or j is even. Thus, vector UDM only excites modes where both i and j are odd.

The total displacement PSD S_{xx}^{DM} due to UDM can be expressed in terms of the UDM-induced acceleration PSD S_{aa}^{DM} (PSD of the differential acceleration Δa_{DM}) as[7]

$$\begin{aligned} S_{xx}^{\mathrm{DM}} &= \left| \sum_{ij} \chi_{xa,ij} \alpha_{ij} \right|^2 S_{aa}^{\mathrm{DM}} \\ &\approx \sum_{ij} \left| \chi_{xa,ij} \right|^2 \alpha_{ij}^2 S_{aa}^{\mathrm{DM}} \end{aligned} \tag{3.18}$$

where

$$\left| \chi_{xa,ij} \right|^2 = \left(\left({\omega_{ij}}^2 - \omega^2 \right)^2 + \frac{\omega^2 {\omega_{ij}}^2}{{Q_m}^2} \right)^{-1} . \tag{3.19}$$

3.2 Potential of a DM search with optomechanical membranes

3.2.1 Sensitivity requirements

The Eöt-Wash torsion balance EP tests have set strong constraints on vector UDM coupling strengths g_{B-L} and g_B in the kHz to GHz UDM frequency range, imposing stringent requirements on the minimum detectable differential acceleration $\Delta a_{\mathrm{DM,min}}$ and DM-strain sensitivity $\sqrt{S_{aa}^{\mathrm{DM}}}$ of next-generation mechanical detectors.

For coupling to $B - L$, the detector requirements to improve upon EP test constraints are roughly

$$\begin{aligned} & g_{B-L} \lesssim 10^{-23} \left(\frac{f}{1\ \mathrm{kHz}} \right)^{1/4} \\ \rightarrow \quad & \Delta a_{\mathrm{DM,min}} \lesssim 10^{-13} \left(\frac{\Delta_{12}}{0.053} \right) \left(\frac{f}{1\ \mathrm{kHz}} \right)^{1/4} \frac{\mathrm{m}}{\mathrm{s}^2} \\ \rightarrow \quad & \sqrt{S_{aa}^{\mathrm{DM}}} \lesssim 10^{-11} \left(\frac{\Delta_{12}}{0.053} \right) \left(\frac{\tau_{\mathrm{int}}}{1\ \mathrm{year}} \right)^{1/4} \frac{\mathrm{m}}{\mathrm{s}^2} \mathrm{Hz}^{-1/2}. \end{aligned} \tag{3.20}$$

[7] The effective susceptibilities $\chi_{xa,ij}\alpha_{ij}$ for each mode can be approximately added in quadrature because the high quality factor Q_m gives sharp resonances in $\chi_{xa,ij}$, so that cross terms are negligible.

For coupling to B, the requirements are roughly

$$\begin{aligned} g_B &\lesssim 10^{-22}\left(\frac{f}{1\text{ kHz}}\right)^{1/4} \\ \rightarrow\quad \Delta a_{\text{DM,min}} &\lesssim 10^{-14}\left(\frac{\Delta_{12}}{0.0018}\right)\left(\frac{f}{1\text{ kHz}}\right)^{1/4}\frac{\text{m}}{\text{s}^2} \\ \rightarrow\quad \sqrt{S_{aa}^{\text{DM}}} &\lesssim 10^{-11}\left(\frac{\Delta_{12}}{0.0018}\right)\left(\frac{\tau_{\text{int}}}{1\text{ year}}\right)^{1/4}\frac{\text{m}}{\text{s}^2}\text{Hz}^{-1/2}. \end{aligned} \tag{3.21}$$

In practice, these figures of merit are difficult to achieve with a cm-scale, sub-gram mass detector like the membrane proposed here. However, these requirements can be met by utilizing high-Q mechanical resonances to amplify the signal, reducing readout requirements for a thermally-limited measurement. On-resonance, the detector's compact form factor becomes a benefit, facilitating cryogenic cooling to reduce the thermal noise floor and enhance sensitivity.

3.2.2 Sensitivity and noise

Classical optomechanical systems are fundamentally limited by thermomechanical (thermal) noise, which refers to the thermal motion of a membrane at finite temperature T, and imprecision and backaction noise, which comes from photon shot noise introduced by the optical readout. Imprecision and backaction noise are described by displacement PSD S_{xx}^{imp} and acceleration PSD S_{aa}^{ba}, respectively.[8] Each mechanical mode experiences thermal noise with acceleration PSD given by [79, 80]

$$S_{aa,ij}^{\text{th}} = \frac{4k_{\text{B}}T\omega_{ij}}{\mu_m Q_m}. \tag{3.22}$$

The total displacement noise in the measurement, including contributions from each mode, is

$$S_{xx}^{\text{noise}} = S_{xx}^{\text{imp}} + \sum_{ij}|\chi_{xa,ij}|^2\left(S_{aa,ij}^{\text{th}} + S_{aa}^{\text{ba}}\right). \tag{3.23}$$

[8] See Section 1.4 for an explanation of measurement imprecision and backaction. See Section 2.3.2 for expressions for S_{xx}^{imp} and S_{aa}^{ba}.

Equating S_{xx}^{DM} (from Eq. 3.18) with S_{xx}^{noise}, the membrane system's acceleration sensitivity is

$$\sqrt{S_{aa}^{\mathrm{DM}}} = \left(\sum_{ij} |\chi_{xa,ij}|^2 {\alpha_{ij}}^2 \right)^{-1/2} \sqrt{S_{xx}^{\mathrm{noise}}}. \tag{3.24}$$

3.2.3 Minimum detectable coupling strength

The minimum detectable differential acceleration[9] over an integration time $\tau_{\mathrm{int}} \gg \tau_{\mathrm{DM}}$ depends on the acceleration sensitivity in Eq. (3.24) as

$$\Delta a_{\mathrm{DM,min}} \approx \sqrt{2 S_{aa}^{\mathrm{DM}}} \, (\tau_{\mathrm{DM}} \tau_{\mathrm{int}})^{-1/4} \tag{3.25}$$

and the minimum detectable coupling strength is

$$g'_{\mathrm{min}} = \frac{\sqrt{3}}{\Delta_{12} a_{\mathrm{DM,rms}}} \Delta a_{\mathrm{DM,min}}. \tag{3.26}$$

The expected minimum detectable coupling strengths $g_{B-L,\mathrm{min}}$ and $g_{B,\mathrm{min}}$ are plotted in Figs. 3.2 and 3.3, respectively, for square membranes ranging from 2.5 – 20 cm wide. It is assumed that the membranes have thickness $h = 200$ nm, mechanical quality factor $Q_m = 10^9$, and temperature $T = 10$ mK. It is further assumed that the membranes form an optical cavity with finesse $\mathcal{F} = 100$, and that the measurement of the membrane's motion is performed using a laser with wavelength $\lambda = 1\,\mu$m and power $P = 0.3$ mW.

It can be seen in Figs. 3.2 and 3.3 that cryogenically-cooled optomechanical membrane-based detectors are capable of reaching new regions of the vector UDM parameter space, potentially improving upon the current bounds by over an order of magnitude, over narrow bandwidths around the resonance frequencies. The proposed Si_3N_4-Be optomechanical system achieves better sensitivity to $B - L$ coupling ($\Delta_{12} = 0.053$) than for B coupling ($\Delta_{12} = 0.0018$). Superior sensitivity to $B - L$ coupling is typical for heterogeneous, vector

[9] The discussion in Section 2.3.3 about the minimum detectable force applies to any type of signal, such as acceleration, displacement, or strain. For the optomechanical membrane-based detectors proposed here, whose motion would cause a phase shift of the light exiting the optical cavity that is measured interferometrically, the experimental observable is the optical power at the interferometer output. The membrane's acceleration is inferred from the measured optical power.

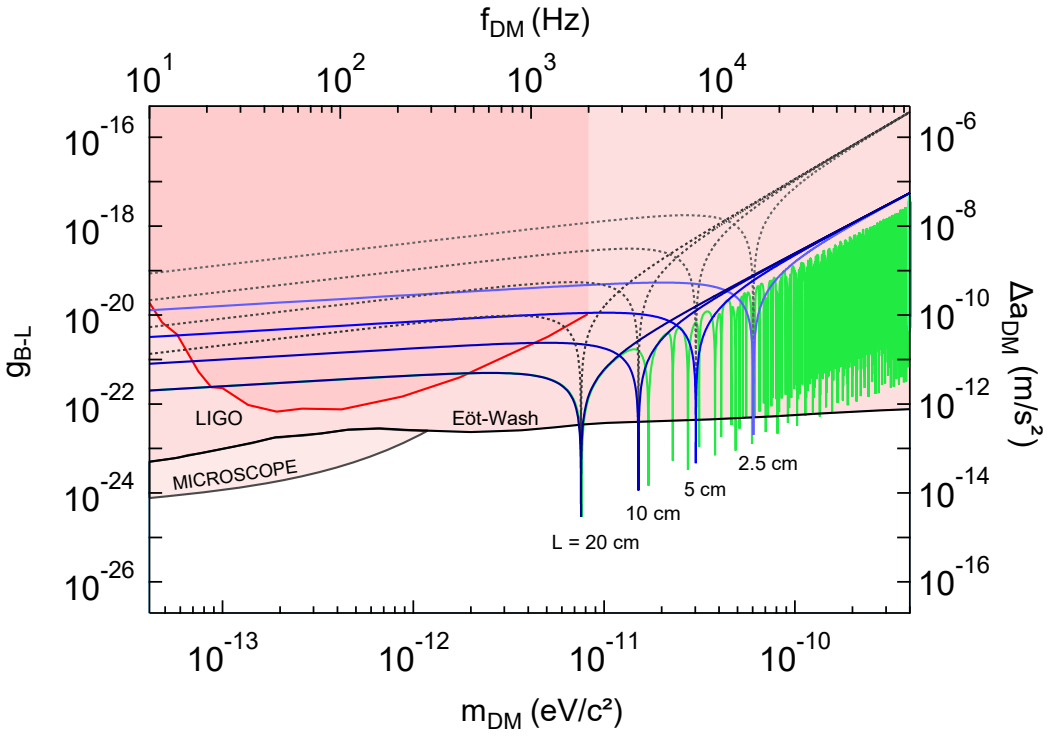

Figure 3.2: Centimeter-scale Si_3N_4 membranes as vector B-L dark matter detectors: Solid blue (dashed gray) curves indicate the minimum detectable coupling strength for square membranes with side lengths ranging from 2.5-20 cm, assuming an integration time of $\tau_{\text{int}} = 1$ year ($\tau_{\text{int}} = \tau_{\text{DM}}$) and accounting for only the fundamental mechanical mode. The green curve results from a multimode analysis for a 20 cm membrane. Shaded regions indicate constraints from EP tests [6, 8] and LIGO [43]. The right axis indicates the differential acceleration assuming $\Delta_{12} = 0.053$. Figure adapted from Ref. [42] ©2021 American Physical Society.

UDM detectors, as differences in relative neutron fraction are typically greater than differences in atomic binding energy.

While the frequencies of the fundamental modes span from 2 – 25 kHz, higher-order modes can extend the frequency range of a single membrane.[10] Comparing the multimode

[10] In theory, a membrane has an infinite number of modes and the frequency range of the detector is limited by the bandwidth of the optical measurement. For example, a $\sim$ 1 mm long optical cavity has a readout bandwidth of $c/(2L\mathcal{F}) \sim 1$ GHz, encompassing $\sim 10^{11}$ modes of a 10 cm membrane.

(green) curve and the single mode (blue) curves in Fig. 3.2, it can be seen that the performance of a single membrane with higher-order modes is similar to an array of (single mode) membranes of varying size.

Generally, the acceleration sensitivity is limited by backaction and thermal noise near the mechanical resonances; the sensitivity is limited by imprecision noise off resonance. For example, consider a square membrane with side lengths of 10 cm. Near the fundamental resonance frequency at $\sim$ 4 kHz, thermal noise and backaction noise are roughly equal, contributing a combined $\sim 10^{-12}$ m·s^{-2}·Hz$^{-1/2}$ to the acceleration noise floor, while the contribution from imprecision noise is $\sim 10^{-17}$ m·s^{-2}·Hz$^{-1/2}$ (from $S_{xx}^{\mathrm{imp}} \approx 10^{-17}$ m·Hz$^{-1/2}$). Therefore, the total motion of the membrane is resolved ($S_{xx}^{\mathrm{imp}} < S_{xx}^{\mathrm{th}} + S_{xx}^{\mathrm{ba}}$) on resonance, and the detector achieves $g_{B-L,\mathrm{min}} \approx 10^{-24}$ over a fractional bandwidth of $\sim 10^{-4}$.

3.2.4 Search strategies

In the search for vector UDM, optomechanical membranes are able to compete with larger detectors like LIGO [43] and torsion balances [13] because of their high mechanical Q-factors for resonant amplification of the acceleration signal (producing a greater phase shift in light exiting the optical cavity) and their compatibility with cryogenic cooling to reduce thermal noise on resonance. However, the exceptional sensitivity of resonant sensors comes at the price of reduced bandwidth, as evident in the blue single-mode curves in Figs. 3.2 and 3.3. As a result, a more complete vector UDM search with resonant optomechanical membranes will require frequency scanning[11] or an array of detectors [42].

3.3 Conclusion

In this chapter, the prospect of performing a search for $B-L$- or B-coupled vector UDM using resonant, heterogeneous, optomechanical accelerometers is discussed. As an example, detectors based on centimeter-scale, cryogenically-cooled Si_3N_4 membranes have been considered. It has been demonstrated that such detectors, operating on resonance, are

[11] The resonance frequencies of Si_3N_4 membranes are tunable [84, 85, 112, 113], enabling frequency scans to increase the effective bandwidth of a single membrane mode.

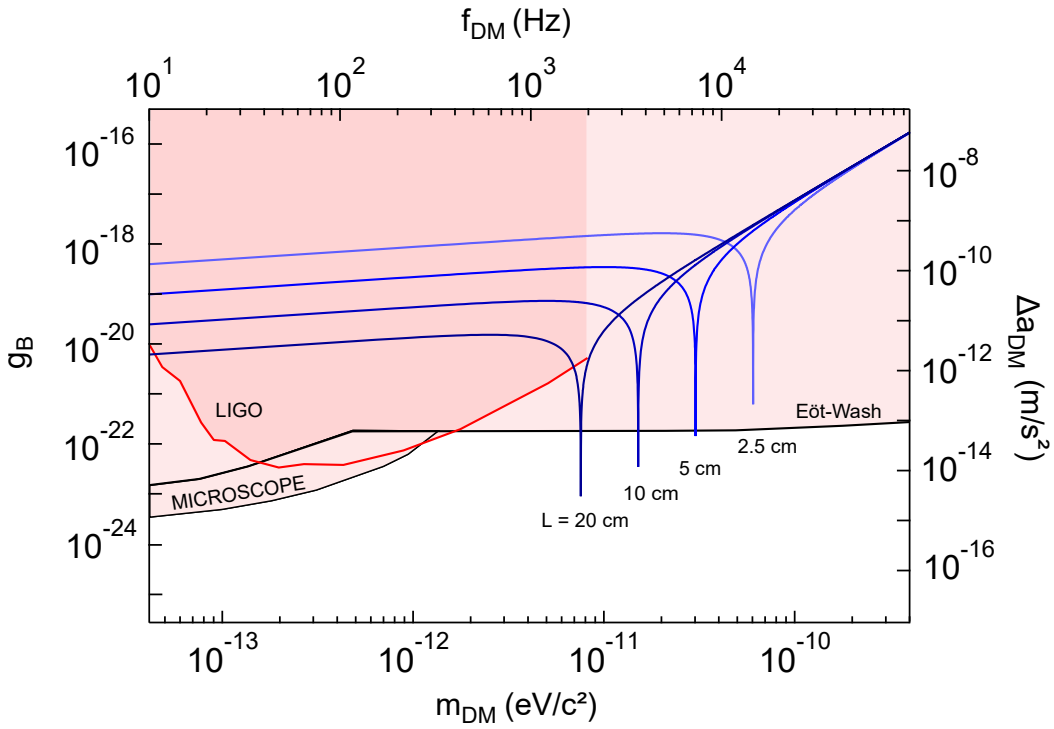

Figure 3.3: Projected constraints on B coupling by Si_3N_4 membranes: Blue curves are for centimeter-scale membranes as in Fig. 3.3, with the suppression factor Δ_{12} adjusted for B coupling. Shaded regions indicate constraints from EP tests [6, 13] and LIGO [43]. The right axis indicates the differential acceleration assuming $\Delta_{12} = 0.0018$. Figure adapted from Ref. [42] ©2021 American Physical Society.

capable of improving upon the current bounds set on the vector UDM coupling strength by over an order of magnitude. By utilizing higher-order mechanical modes and implementing detector arrays and frequency-scanning techniques, optomechanical membranes are capable of performing searches for vector UDM spanning the frequency range $1 - 100$ kHz.

In light of the technical challenges that will arise as optomechanical membrane-based UDM detectors are pursued experimentally [117], the theoretical treatment presented here will need to be adapted to match experimental constraints. In particular, this analysis for $g'_{\rm min}$ applies for square, homogeneous membranes. However, the analysis will need to be adapted to include different geometries, such as a trampoline resonator [118] with photonic crystal patterning [119] (to increase the optical cavity's finesse), for which mode-dependent

parameters (e.g. u_{ij}, μ_{ij}, ω_{ij}, α_{ij}) would need to be recalculated.

Additionally, a greater region of parameter space can be reached by performing a frequency scan than simply measuring for a longer integration time [117]. To optimize a frequency scan to address of the largest parameter space possible, a theoretical treatment that considers the relative contributions of each noise source (which determines the on-resonance detection bandwidth) is necessary. This treatment can also be used to chose (potentially) tunable experimental parameters, such as the membrane geometry and cavity finesse (prior to detector construction) or the optical power and wavelength (after detector construction).

Chapter 4

PROPOSAL OF A SCALAR UDM SEARCH WITH COMPACT MECHANICAL RESONATORS

In this chapter, compact mechanical resonators are proposed as detectors for scalar UDM. The material in this chapter was adapted from Ref. [33], *Searching for scalar dark matter with compact mechanical resonators*, Jack Manley and others; Phys. Rev. Lett. **124**, 151301 (2020). Reproduced here with permission, ©2020 American Physical Society.

As described in Section 2.2.2, scalar UDM coupled to photons and electrons produces an oscillating strain signal. This strain produces a measurable displacement in a body composed of many atoms, and it can be resonantly enhanced in an elastic body with acoustic modes at the dark matter frequency. Recently it has been suggested to search for this *acoustic* DM signature using resonant-mass antennae [34], such as re-purposing Weber-bar [120] gravitational wave (GW) detectors. In fact, data from AURIGA–a resonant-mass GW detector–has been reanalyzed in the context of scalar UDM to put bounds on scalar DM coupling [24]. Traditional resonant-mass GW detectors, like AURIGA, are typically very large ($\sim 10^3$ kg), with frequencies around ~ 1 kHz. Given the uncertainty in the UDM frequency, a more complete search using resonant mass detectors will require many resonators operating across a large frequency range.

In this chapter, the resonant-mass approach is extended to a broader class of mechanical resonators with compact form factors. The compactness of the devices makes them better-suited to small-scale laboratories, enabling more UDM searches to cover the large frequency range of the UDM parameter space. With masses spanning from a few kilograms to less than a gram, the resonators considered in this chapter can provide access to a broad frequency (mass) range of 100 Hz – 100 MHz (10^{-12} – 10^{-6} eV/c^2). Owing to their small dimensions and crystalline material, these devices can be operated at dilution refrigerator

temperatures with quality factors as high as 10^{10} [46], thereby substantially reducing thermal noise and potentially achieving constraints on dark matter coupling strength that are orders of magnitude below the current bounds.

The organization of this chapter is similar to that of Chapter 3:

- Section 4.1 focuses on the scalar UDM strain signal and how it excites vibrations in bar-type mechanical resonators. The result is Eq. (4.14), which is an expression for a resonator's displacement PSD due to a DM-induced strain.
- The purpose of Section 4.2 is to explain Figs. 4.3 and 4.4, which are the result of this work. Figures 4.3 and 4.4 are plots of the minimum detectable coupling strength for the proposed resonators in comparison to constraints from previous experiments.
- Section 4.3 contains concluding remarks.

4.1 Mechanical resonators as DM detectors

4.1.1 Strain signal

As discussed in Section 2.2.4, scalar UDM coupled to photons or electrons produces an isotropic and nearly material-independent strain signal that is well-described by

$$h_{\mathrm{DM}}(t) \approx (d_e + d_{m_e})\, h_{\mathrm{DM},0} \cos(\omega_{\mathrm{DM}} t), \tag{4.1}$$

where d_e (d_{m_e}) is the strength of the coupling to photons (electrons). The total coupling strength is defined as $d_{\mathrm{DM}} \equiv d_e + d_{m_e}$. The amplitude $h_{\mathrm{DM},0}$ is a stochastic quantity with root-mean-square value

$$h_{\mathrm{DM,rms}} \equiv \sqrt{\frac{8\pi G \rho_{\mathrm{DM}}}{c^2 {\omega_{\mathrm{DM}}}^2}}. \tag{4.2}$$

In the presence of scalar UDM, atoms are strained according to Eq. (4.1), resulting in the deformation of a macroscopic solid (rather, any form of condensed matter). Deformation is characterized by the displacement vector $\boldsymbol{u}(t, \boldsymbol{r})$, a field describing the displacement of a volume element from its equilibrium position within the solid. The UDM strain signal acts as a perturbation to the displacement field. In an isotropic elastic medium, the effect can be modeled as an isotropic perturbation [34, 121]

$$\boldsymbol{u}(t, \boldsymbol{r}) \to \boldsymbol{u}(t, \boldsymbol{r}) - \boldsymbol{r} h_{\mathrm{DM}}(t), \tag{4.3}$$

where $\boldsymbol{r}$ is the position relative to a stationary reference such as the object's center of mass or a rigid boundary.

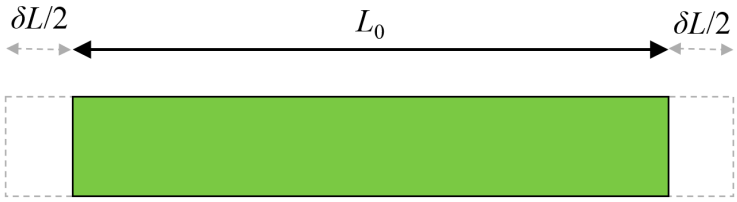

Figure 4.1: Scalar UDM strain in a rigid rod: A quasi-static UDM strain signal results in a change in length of $\delta L = L_0 h_{\rm DM}$.

Considering a simple 1-dimensional rigid rod in the presence of a quasi-static[1] scalar UDM field, the perturbed displacement field in Eq. (4.3) simply results in a change in length of the rod, such that $\delta L/L_0 = h_{\rm DM}$. However, if the DM frequency matches the resonance frequency of one of the rod's mechanical oscillation modes, the resulting displacement will be amplified so that $\delta L/L_0 \sim Q_m h_{\rm DM}$, where Q_m is the quality factor of the mechanical mode. In particular, for the mechanical resonators that will be considered in this chapter, scalar UDM will only excite breathing (or dilation) modes, where the total length of the resonator oscillates.

4.1.2 Compact mechanical resonators

This chapter is concerned with resonant detectors, which are capable of amplifying the DM-induced strain signal in proportion to their mechanical Q-factor. Under consideration are four compact mechanical resonators that are composed of high-quality materials (superfluid helium, crystalline sapphire, and crystalline quartz), making them inherently capable of attaining high Q-factors. Due to their differences in size, each of the proposed detectors operates in a different frequency range, affording access to a large region of the scalar UDM parameter space from 100 Hz to 100 MHz.

[1] In the quasi-static scenario, the DM frequency is far below the frequency of any mechanical resonances, so that the oscillation of the UDM field is significantly slower than the response time of the rod.

For DM frequencies $100\,\mathrm{Hz} \lesssim f_{\mathrm{DM}} \lesssim 25\,\mathrm{kHz}$, we consider a superfluid helium bar resonator, which is probed optomechanically as discussed in Ref. [122] [rendered in Fig. 4.2(a)]. The detector would consist of a rigid cylindrical shell that houses the superfluid helium. The detector's design follows that of Ref. [123], with dimensions given in the caption of Fig. 4.2. To aid in cavity optomechanical readout, one of the end faces of the cylindrical shell is assumed to be a movable boundary. In practice, this can be approximately realized by using a flexible membrane as the end face. The resonant medium is the 2.7 kg volume of superfluid, which is inherently low loss. A mechanical quality factor of $Q_m = 10^9$ is assumed, which would be limited by doping and clamping loss [122].

For DM frequencies $50\,\mathrm{kHz} \lesssim f_{\mathrm{DM}} \lesssim 2.5\,\mathrm{MHz}$, we consider a 0.3 kg HEM® sapphire cylinder intended for use as an end-mirror in future cryogenic GW detectors [44] [rendered in Fig. 4.2(b)]. The resonator dimensions provided in the caption of Fig. 4.2 are motivated by the design in Ref. [44]. Crystalline sapphire is a high-quality acoustic material capable of attaining a Q-factor of $Q_m = 10^9$ [124, 125].

For DM frequencies $550\,\mathrm{kHz} \lesssim f_{\mathrm{DM}} \lesssim 27\,\mathrm{MHz}$, we consider a cm-scale sapphire pillar resonator, which is similar in character to the sapphire cylinder, though significantly reduced in size [rendering in Fig. 4.2(c)]. This design is based on a quartz "micropillar" resonator developed by Neuhaus et al [126, 127], where the pillar is suspended in the middle of a thin quartz membrane for acoustic isolation (illustrated by the gray triangle in Fig. 4.2(c)). The pillar is assumed to be re-scaled to the dimensions given in the caption of Fig. 4.2 and reconstructed of sapphire, whose higher density and sound velocity produces larger strain coupling in order to begin setting new constraints in the MHz regime with only ~ 0.3 grams of mass and an assumed $Q_m = 10^9$.

Finally, for DM frequencies $10\,\mathrm{MHz} \lesssim f_{\mathrm{DM}} \lesssim 350\,\mathrm{MHz}$, a quartz bulk acoustic wave (BAW) resonator [46] is considered [rendering in Fig. 4.2(d), with dimensions given in the caption]. A scalar UDM search with BAWs was initially proposed in Ref. [34] and has been included in this analysis for completeness. Quartz BAWs can achieve $Q_m = 10^{10}$ [46], enabling a UDM search at the relatively unprobed MHz frequencies (see Figs. 2.8 and 2.9).

In order to determine how strongly the scalar UDM strain signal couples to each

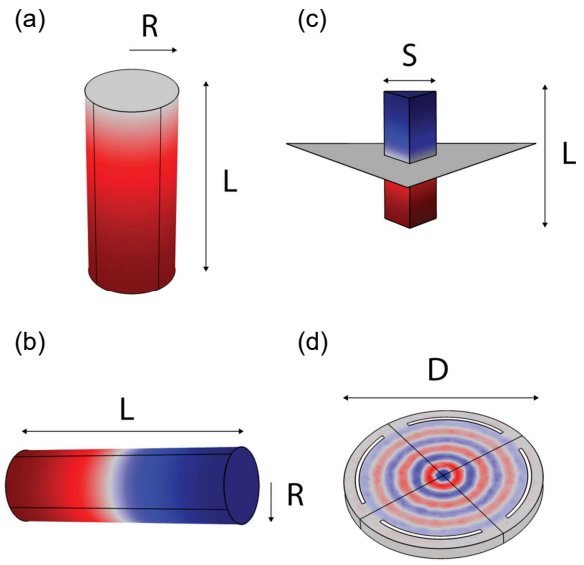

Figure 4.2: Resonator acoustic modes: Renderings of each of the proposed resonators, with a simulated acoustic mode displayed in red-blue scale. **(a)** Superfluid helium detector; $R = 10.8$ cm, $L = 50$ cm. **(b)** Sapphire cylinder; test mass. From Ref. [44] $R = 15$ mm, $L = 10$ cm. **(c)** Rendering of sapphire pillar. $s = 4$ mm, $L = 1$ cm. **(d)** Rendering of quartz BAW resonator. From Ref. [45, 46] $L = 1$ mm, $D = 30$ mm, $R = 300$ mm, where L is the thickness and R is the radius of curvature of the top surface. Figure adapted, with permission from Russell Stump, from Ref. [33] ©2020 American Physical Society.

resonator, one first needs to determine their acoustic modes. For this analysis each resonator is treated as isotropic, homogeneous, and linearly elastic. Considering only longitudinal modes, the equation of motion for the displacement field $\boldsymbol{u}(t, \boldsymbol{r})$ is then [128]

$$\ddot{\boldsymbol{u}} = {v_s}^2 \nabla^2 \boldsymbol{u}, \tag{4.4}$$

where v_s is the sound speed. The total displacement field can be expanded in terms of its eigenmodes, $\boldsymbol{u}(t, \boldsymbol{r}) = \sum_i x_i(t)\boldsymbol{u_i}(\boldsymbol{r})$, where $x_i(t)$ gives the amplitude and phase of the oscillation while $\boldsymbol{u_i}(\boldsymbol{r})$ is the dimensionless spatial distribution, or modeshape. The modes are orthogonal $\left(\iiint dV \boldsymbol{u_i} \cdot \boldsymbol{u_j} \propto \delta_{ij}\right)$ with normalization chosen such that $|\boldsymbol{u_i}|_{\max} = 1$. Each mode

can be further characterized by an effective mass μ_i, defined as[2]

$$\mu_i \equiv \iiint dV \rho \, |\boldsymbol{u_i}|^2 \, . \tag{4.5}$$

Three of the resonators (superfluid helium, test mass, and pillar) can be treated effectively as 1D rods oriented along the x-axis with longitudinal modes $\boldsymbol{u_i}(\boldsymbol{r}) = u_i(x)\hat{\boldsymbol{x}}$. The mode solutions are simply

$$u_i(x) = \cos\left(\frac{\omega_i}{v_s} x + \theta_i\right) \tag{4.6}$$

where ω_i is the mode's angular frequency and θ_i is the phase, both of which will be determined by the boundary conditions. Figure 4.2 displays a basic rendering of each device with an acoustic mode. At free acoustic boundaries, the motion of the edge of the bar is unconstrained, reaching maximum displacement $|u_i(x_{\text{free}})| = 1$. At fixed acoustic boundaries, the oscillator's motion is restricted, so that $|u_i(x_{\text{fixed}})| = 0$.

The test mass and pillar can be treated as 1D bars with length L, cross-sectional area A, and free acoustic boundaries. If the end faces are located at $x = 0$ and $x = L$. The spatial modes are described by Eq. (4.6), with $\theta_i = 0$ and $\omega_i = i\pi v_s/L$. From Eq. (4.5), the effective mass is found to be mode independent, $\mu_i = \rho AL/2$, which is just half the total mass of the resonator.

The geometry of the proposed superfluid helium cylinder differs only in that the end face at $x = 0$ is assigned a rigid acoustic boundary condition. The spatial modes are described by Eq. (4.6), with $\theta_i = -\pi/2$ and $\omega_i = (2i-1)\pi v_s/2L$. The effective mass is again $\mu_i = \rho AL/2$.

The geometry of BAWs is slightly more complicated due to their rounded end face. However, the displacement modes for BAWs are characterized in Ref. [45]. The displacement modes are quasi-longitudinal with the dominant component's modeshape given by

$$u_i(x) \approx \sin\left[\frac{i\pi x}{L}\right] \exp\left[-\frac{i\pi}{2}\sqrt{\frac{2}{5RL^3}}\left(y^2 + z^2\right)\right], \tag{4.7}$$

with frequency $\omega_i \approx i\pi v_s/L$ and effective mass

$$\mu_i \approx \frac{\rho L}{2i}\sqrt{\frac{5RL^3}{2}}, \tag{4.8}$$

[2] The mass density ρ of each resonator will be considered spatially uniform.

where R is the radius of curvature of the curved end face of the BAW resonator.

4.1.3 DM-coupling to acoustic modes of an arbitrary resonator

To include the DM signal into the equations of motion for the resonator, replace the displacement field in Eq. (4.4) with the perturbed displacement field described by Eq. (4.3) to get

$$\ddot{\boldsymbol{u}} - {v_s}^2 \nabla^2 \boldsymbol{u} = \boldsymbol{r}\ddot{h}_{\rm DM}. \tag{4.9}$$

Considering a resonator with non-degenerate acoustic modes, each mode can be treated independently,[3] such that

$$\ddot{x}_i \boldsymbol{u_i} + {\omega_i}^2 x_i \boldsymbol{u_i} = \boldsymbol{r}\ddot{h}_{\rm DM}. \tag{4.10}$$

Multiplying both sides of Eq. (4.10) with the operator $\iiint dV \boldsymbol{u_i}\cdot$, one can reduce the equations of motion to the form of a driven harmonic oscillator[4]

$$\ddot{x}_i + \gamma_i \dot{x}_i + {\omega_i}^2 x_i = \alpha_i \ddot{h}_{\rm DM}. \tag{4.11}$$

The strength of the coupling between the scalar strain signal and the ith mode is characterized by the overlap factor

$$\alpha_i \equiv \frac{\iiint dV\,(\boldsymbol{u_i}\cdot\boldsymbol{r})}{\iiint dV\,|\boldsymbol{u_i}|^2}. \tag{4.12}$$

From the mode solutions detailed in Section 4.1.2, the overlap factors are found to be

$${\alpha_i}^2 = \begin{cases} 8L^2(i\pi)^{-4}\left(1-(-1)^i\right) & \text{test mass and pillar} \\ 64L^2(2i-1)^{-4}\pi^{-4} & \text{superfluid helium} \\ 64L^2\,(i\pi)^{-4} & \text{BAWs} \end{cases} \tag{4.13}$$

Evidently, for the sapphire cylinder and pillar, only odd-ordered modes couple to the scalar strain signal. For the superfluid helium and BAW resonators, both even and odd modes are excited by scalar UDM.

---

[3] The UDM strain $h_{\rm DM}$ is (nearly) monochromatic, so it will excite a mode only if the DM frequency is near the mode frequency.

[4] Mechanical dissipation $\gamma_i = \omega_i/Q_m$ has been introduced a posteriori, assuming a mode-independent quality factor $Q_i \equiv Q_m$.

The displacement PSD due to UDM S_{xx}^{DM} can be expressed in terms of the DM strain PSD S_{hh}^{DM}, adding the modal susceptibilities $\chi_{xa,i}\alpha_i$ in quadrature (see Section 3.1.3),

$$S_{xx}^{\mathrm{DM}} = \left[\omega^4 \sum_i \left|\chi_{xa,i}\right|^2 {\alpha_i}^2\right] S_{hh}^{\mathrm{DM}}, \tag{4.14}$$

where

$$\left|\chi_{xa,i}\right|^2 = \left(\left({\omega_i}^2 - \omega^2\right)^2 + \frac{\omega^2 {\omega_i}^2}{{Q_m}^2}\right)^{-1}. \tag{4.15}$$

4.2 Potential of a DM search with compact mechanical resonators

4.2.1 Sensitivity requirements

As in Chapter 3 with vector UDM, EP tests [8] have set constraints on scalar UDM coupling strengths d_e and d_{m_e}. As described in Section 3.2.1, compact detectors can overcome the requirements on minimum detectable strain h_{min} and DM-strain sensitivity $\sqrt{S_{hh}^{\mathrm{DM}}}$ with cryogenic cooling and resonant amplification.

For coupling to photons, the requirements are

$$\begin{aligned} & d_e \lesssim 10^{-3}\left(\frac{f}{1\ \mathrm{Hz}}\right)^{1/4} \\ \rightarrow \quad & h_{\mathrm{min}} \lesssim 10^{-21}\left(\frac{1\ \mathrm{kHz}}{f}\right)^{3/4} \\ \rightarrow \quad & \sqrt{S_{hh}^{\mathrm{DM}}} \lesssim 10^{-19}\left(\frac{1\ \mathrm{kHz}}{f}\right)\left(\frac{\tau_{\mathrm{int}}}{1\ \mathrm{year}}\right)^{1/4} \mathrm{Hz}^{-1/2}. \end{aligned} \tag{4.16}$$

For coupling to electrons, the requirements are

$$\begin{aligned} & d_{m_e} \lesssim 10^{-2}\left(\frac{f}{1\ \mathrm{Hz}}\right)^{1/4} \\ \rightarrow \quad & h_{\mathrm{min}} \lesssim 10^{-20}\left(\frac{1\ \mathrm{kHz}}{f}\right)^{3/4} \\ \rightarrow \quad & \sqrt{S_{hh}^{\mathrm{DM}}} \lesssim 10^{-18}\left(\frac{1\ \mathrm{kHz}}{f}\right)\left(\frac{\tau_{\mathrm{int}}}{1\ \mathrm{year}}\right)^{1/4} \mathrm{Hz}^{-1/2}. \end{aligned} \tag{4.17}$$

4.2.2 Sensitivity and noise

In Chapter 3, detailed consideration was given to imprecision, backaction, and thermal noise. The resonators in this chapter have significantly larger effective mass than an

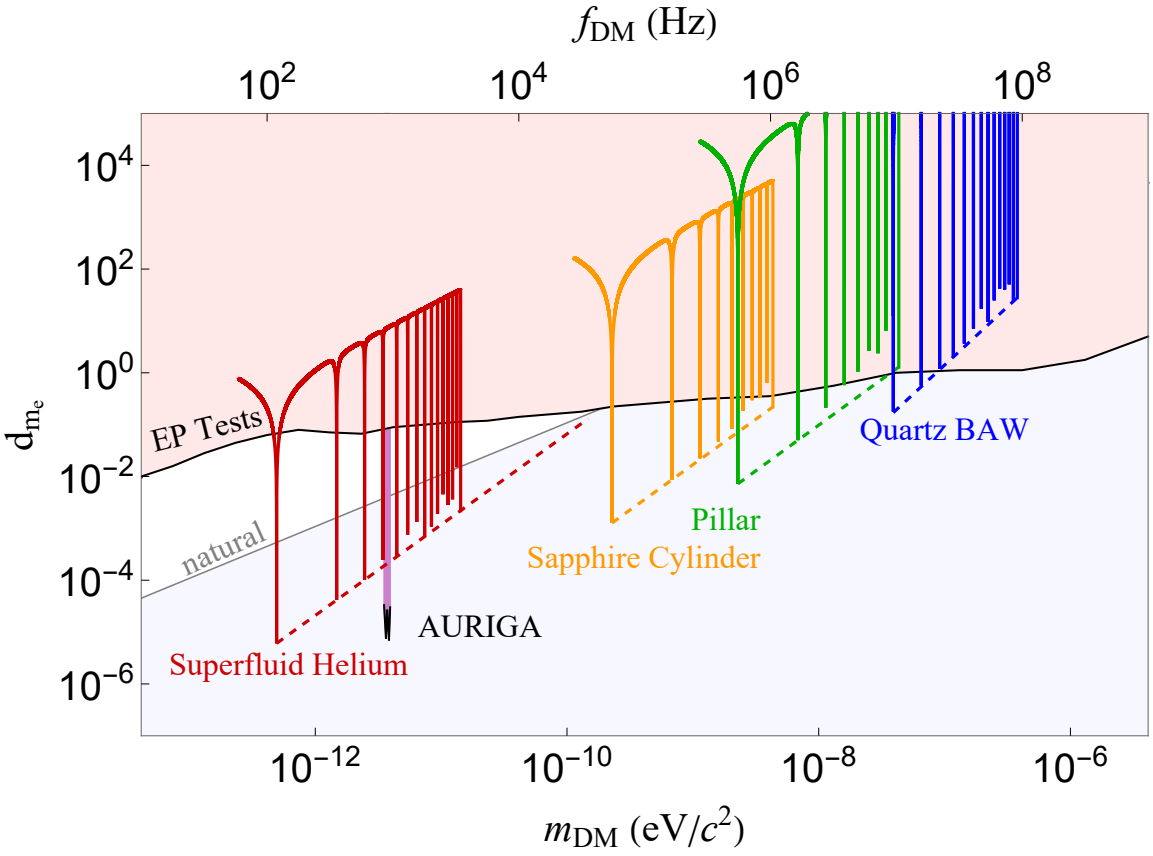

Figure 4.3: Projected constraints on d_{m_e} from compact mechanical resonators: Solid lines indicate the minimum detectable coupling strength across several low-order modes for each proposed resonator. For each resonator, multiple resonances achieve sensitivity below constraints set by EP tests[8] and AURIGA [24]. Dashed lines indicate the ultimate thermal limit to detection. The thermal limit is achieved at every resonance, although the plot's limited resolution gives the appearance that some of the resonances are less deep. The integration time is $\tau_{\mathrm{int}} = 1$ year. Also included is a region satisfying the naturalness criterion for a scalar field [47], which is defined to be consistent with other work [34, 47, 48]. The naturalness criterion is not a constraint, but can be considered a region with additional theoretical motivation. Figure adapted from Ref. [33] ©2020 American Physical Society.

optomechanical membrane, reducing the effects of measurement backaction. Thus, on resonance, thermal noise sets the limit on detection sensitivity (dashed lines in Figs. 4.3 and 4.4), although measurement imprecision will still limit the detection bandwidth for each mechanical mode.

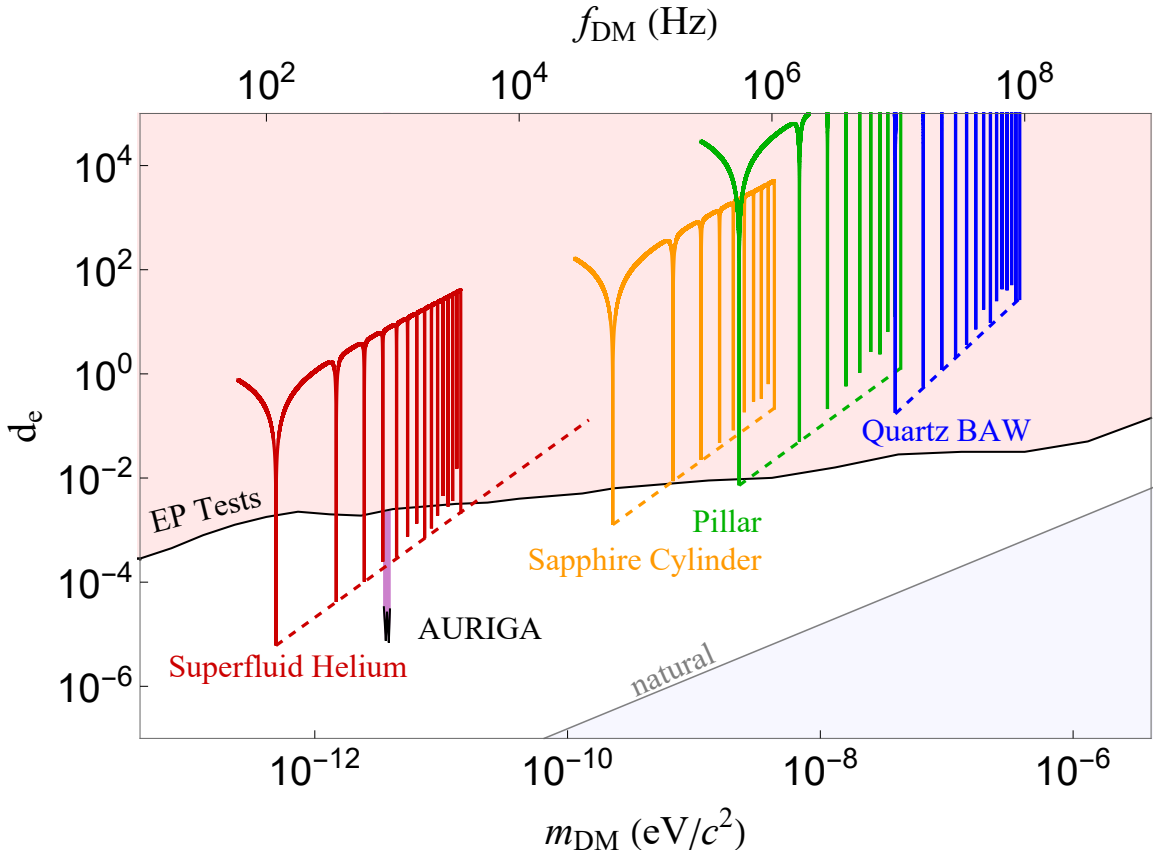

Figure 4.4: Projected constraints on d_e from compact mechanical resonators: The projected constraints from resonators are the same as in Fig. 4.3. The natural region and EP test constraints and have shifted, reducing the region of new parameter space that can be probed by each resonator. For example, the projected constraints from quartz BAWs do not improve upon EP test constraints on d_e. Figure adapted from Ref. [33] ©2020 American Physical Society.

Thermomechanical noise drives each mechanical mode into Brownian motion [129] with acceleration PSD given by

$$S^{\rm th}_{aa,i} = \frac{4k_{\rm B}T\omega_i}{\mu_i Q_m}. \tag{4.18}$$

Readout imprecision $S^{\rm imp}_{xx}$ can be generically included, so that the total measured displacement noise PSD for each resonator is given by

$$S^{\rm noise}_{xx} = S^{\rm imp}_{xx} + \sum_i \left|\chi_{xa,i}\right|^2 S^{\rm th}_{aa,i}. \tag{4.19}$$

Equating S_{xx}^{DM} (from Eq. 4.14) with S_{xx}^{noise}, the DM-induced strain sensitivity of a detector is

$$\sqrt{S_{hh}^{\mathrm{DM}}} = \left[\omega^4 \sum_i \left|\chi_{xa,i}\right|^2 {\alpha_i}^2\right]^{-1/2} \sqrt{S_{xx}^{\mathrm{noise}}}. \tag{4.20}$$

In the absence of readout noise, thermal noise determines the broadband strain sensitivity of a resonator. However, a high-Q resonator's thermal motion typically exceeds the readout imprecision only over narrow bandwidths around the mechanical resonance frequencies, where the thermal noise is resonantly amplified. The "bandwidth" of a single mechanical resonance is considered the frequency range over which $S_{xx}^{\mathrm{imp}} \leq \left|\chi_{xa,i}\right|^2 S_{aa,i}^{\mathrm{th}}$, and the on-resonance thermally-limited strain sensitivity for each mode is

$$\sqrt{S_{hh,i}^{\mathrm{DM,th}}} = \sqrt{\frac{4k_{\mathrm{B}}T}{\mu_i Q_m {\alpha_i}^2 {\omega_i}^3}}. \tag{4.21}$$

While high-Q resonators generally favor on-resonance sensitivity over bandwidth, the resonators discussed here permit high-sensitivity optomechanical readout. Sapphire cylinders and pillars can be mirror-coated (e.g. using crystalline coatings [130]) and coupled to a Fabry-Pérot cavity. The thermal displacements of the end-faces are on the order of $10^{-14}\,\mathrm{m}/\sqrt{\mathrm{Hz}}$ (cylinder) and $10^{-16}\,\mathrm{m}/\sqrt{\mathrm{Hz}}$ (pillar) near the fundamental mode, implying a fractional bandwidth of 10^{-5} (cylinder) and 10^{-7} (pillar) for a shot-noise-limited displacement sensitivity of $\sqrt{S_{xx}^{\mathrm{imp}}}10^{-18}\,\mathrm{m}/\sqrt{\mathrm{Hz}}$ (achievable with mW of optical power for a cavity finesse of 1000).

Superfluid helium and quartz BAW resonators have been probed non-invasively with low-noise microwave circuits. Low-noise readout of BAWs is typically achieved through capacitive-coupling to a superconducting quantum interference device (SQUID) amplifier, enabling fractional bandwidths of 10^{-6} at 10 MHz for a device at 10 mK with $Q_m \sim 10^8$ [131]. Here, readout noise is assumed at the level $\sqrt{S_{xx}^{\mathrm{imp}}} = 10^{-19}\,\mathrm{m}/\sqrt{\mathrm{Hz}}$, based on the BAW devices characterized in Ref. [45]. Similarly, superfluid helium resonators can be capacitively-coupled to superconducting microwave cavities. Imprecision noise is assumed at the level $\sqrt{S_{xx}^{\mathrm{imp}}} = 10^{-16}\,\mathrm{m}/\sqrt{\mathrm{Hz}}$, which has been achieved in a similar superfluid helium resonator that had been designed to perform a resonant gravitational wave search [83].

4.2.3 Minimum detectable coupling strength

For an integration time $\tau_{\rm int} \gg \tau_{\rm DM}$, the minimum detectable strain for a detector can be expressed in terms of the strain sensitivity (Eq. 4.20) is

$$h_{\rm DM,min} \approx \sqrt{2S_{hh}^{\rm DM}}(\tau_{\rm DM}\tau_{\rm int})^{-1/4}, \tag{4.22}$$

and the minimum detectable coupling strength is

$$d_{\rm DM,min} = \frac{h_{\rm DM,min}}{h_{\rm DM,rms}}. \tag{4.23}$$

While the strain signal depends on the total coupling strength $d_{\rm DM}$, it is conventional to consider each coupling separately, as is done in Figs. 2.8, 2.9, 4.3, and 4.4.

Figures 4.3 and 4.4 plot the estimated minimum detectable coupling strength for each proposed detector, including readout imprecision at the levels discussed in Section 4.2.2, over the first several mechanical modes. The dashed lines indicate the ultimate thermal limit on detection, in the absence of measurement imprecision, assuming a temperature of $T = 10$ mK for the superfluid helium, sapphire pillar, and quartz BAW detectors. For the sapphire cylinder, $T = 10$ K is assumed as an experimental constraint due to the low thermal conductance of the test mass suspensions [132]. Note that while the mode shapes u_i (indicated by color-coding) in Fig. 4.2 are rendered numerically in COMSOL® [133], the results plotted in Fig. 4.3 and Fig. 4.4 are analytical.

The superfluid helium detector is capable of achieving a thermally-limited strain sensitivity of $\sqrt{S_{hh,1}^{\rm DM,th}} = 2.5{\cdot}10^{-21}$ Hz$^{-1/2}$ on its first mechanical mode at $f_1 \approx 120$ Hz, improving upon the current bounds on both d_{m_e} and d_e by more than an order of magnitude. The first mode of the sapphire cylinder is also capable of setting new constraints on both couplings, with $\sqrt{S_{hh,1}^{\rm DM,th}} = 2.4 \cdot 10^{-22}$ Hz$^{-1/2}$ at $f_1 \approx 54$ kHz. The sapphire pillar is capable of reaching the current bounds on d_e, and improving upon the bounds on d_{m_e} by an order of magnitude, with $\sqrt{S_{hh,1}^{\rm DM,th}} = 7.7 \cdot 10^{-23}$ Hz$^{-1/2}$ at $f_1 = 550$ kHz.

Typical $h_{\rm min}$ values derived for the devices in this work are $\sim 10^{-24} - 10^{-23}$. Despite the upward trend of the Eöt-Wash constraints with frequency, it is evident in Eqs. (4.16) (4.17) that higher frequency detectors require a lower $h_{\rm min}$ in order to maintain the same

minimum detectable coupling. This scaling arises from the inverse relationship between the DM field amplitude φ_0 and Compton frequency $f_{\rm DM}$. High-frequency searches are further challenged by the shorter signal coherence time $\tau_{\rm DM}$ (Eq. 1.4) and smaller dimensions of the resonators, which decreases the DM-mode coupling factor α_i, as evident in Eq. (4.13). Therefore, designing mechanical resonators to beat limits set by EP tests is difficult above MHz frequencies. Despite these challenges, some lower-order mechanical modes of quartz BAWs can set new constraints on d_{m_e} at around $\sim$ 10 MHz with a sensitivity of $\sim 5 \cdot 10^{-23}$ Hz$^{-1/2}$, owing largely to the elevated Q-factor of 10^{10}.

4.2.4 Search strategies

As with the resonant detector proposed to search for vector UDM in Chapter 3, compact mechanical resonators are capable of probing the scalar UDM parameter space orders of magnitude below the current bounds because of their ability to achieve high mechanical Q-factors and their compatibility with cryogenic cooling. These two factors permit access to very small UDM signals, but require a sacrifice in bandwidth. As can be seen Figs. 4.3 and 4.4, the total frequency coverage of a single detector is enhanced by simultaneously monitoring multiple mechanical modes. And the gaps between mechanical modes can, in theory, be filled using an array of detectors with different resonance frequencies. An alternate route to increasing the bandwidth of a resonant UDM search is to perform a frequency scan, where an experiment is decomposed into a series of shorter measurements at different frequencies.

A detector's ability to perform a frequency scan is limited by its tunability. While the sound speed of quartz and sapphire are both thermally tunable, ultra-cryogenic operation limits the utility of this approach. Superfluid helium-based resonators, however, are well-suited to perform frequency scans, as their resonance frequencies can be tuned via pressurization (which has been used to change the sound speed of superfluid helium by 50% [82]).

4.3 Conclusion

Considering compact mechanical resonators, with cm-scale dimensions and sub-kg mass, it has been shown that small-scale mechanical experiments have the ability to probe

novel regions of the scalar UDM parameter space over a large frequency range from 100 Hz-100 MHz, corresponding to 10^{-12} – 10^{-6} eV scalar mass range. Exceptional on-resonance strain sensitivities are made possible by the naturally high-quality materials (superfluid and crystalline solids) and compatibility with cryogenic cooling. The reduced bandwidth inherent to resonant detection schemes can compensated for by the small size of the individual devices, which facilitates bandwidth-enhancing techniques such as detector arrays and frequency tuning.

Looking forward to the prospect of performing an experiment to search for scalar UDM with mechanical resonators, it is worth noting that a prototype resonant GW detector using a superfluid helium resonator (similar to that discussed in this chapter) has been built at the University of Alberta [83]. Such a detector is coincidentally sensitive to scalar UDM, and efforts are underway to construct a similar device with the intention of performing a scalar UDM search following the analyses presented here [134]. Additional theoretical treatment will be necessary to conduct a UDM search and interpret the results, such as recalculating mode-dependent parameters (e.g. u_i, μ_i, ω_i, α_i) for the specific detector geometry and optimizing a frequency scan while accounting for the on-resonance detection bandwidth of the detector (as discussed in Section 3.3).

Chapter 5

PROPOSAL OF A SCALAR UDM SEARCH WITH AN OPTICAL FIBER-BASED DETECTOR

The optomechanical detectors proposed in Chapters 3 and 4 resonantly amplify the UDM signal to achieve exceptional sensitivities over narrow bandwidths. However, given the large uncertainty in the UDM frequency, it is desirable to have a detector with broadband sensitivity. The purpose of this chapter is to design a tabletop experiment that is inherently broadband.

Consider the scalar UDM candidates addressed in Chapter 4, which cause a mechanical strain, or a *fractional* oscillation in the length of a detector. The resulting *total* change in length (displacement) can be resonantly amplified by a high-Q mechanical mode to produce a measurable displacement. Without resonance, the same displacement can in theory be achieved simply by using a larger detector. Optical fibers can be kilometers in length while maintaining a compact form factor. In this chapter, an optical fiber-based detector for scalar UDM is investigated.

Lacking high-Q mechanical resonances, spooled fibers are inherently broadband strain sensors that can be many kilometers in length with a small cross-sectional area, resulting in measurable displacements while maintaining a small volume. However, simple designs for a fiber-based detector of the UDM strain signal encounter a problem: scalar UDM will strain everything in the lab equally. A fiber's length is typically measured interferometrically using a laser whose center wavelength is determined by the length of the laser cavity. As dark matter strains the laser cavity, the laser's resonant wavelength is strained in proportion to the fiber length, canceling any UDM-induced phase shift in an interferometric measurement. This example enforces an important concept for UDM searches, which is that experiments must be designed to perform differential measurements. In Chapter 3, this was accomplished

by comparing different materials, which are differentially-accelerated by vector UDM. In Chapter 4, this was accomplished through resonance, where the amplified strain signal in the resonator would exceed the strain in experimental components that are not resonating.

The scalar UDM-induced strain signal is best considered material-independent, making it difficult to detect simply using optical fibers. However, there is another, typically smaller, signal arising from scalar UDM: modulation of refractive indices. Unlike the mechanical strain signal, refractive index modulation is a material-dependent effect. It can be searched for by comparing optical fibers in which the light travels through different materials, such as solid core and hollow core fibers, where the optical mode is confined to silica and air/vacuum, respectively.

In this chapter an optical fiber-based detector is proposed that consists of a 10 km solid core fiber and a 15 km hollow core fiber. By comparing the fibers' refractive indices over time, the detector achieves broadband sensitivity to scalar UDM at frequencies too low ($\lesssim$ 100 Hz) for mechanical resonators. It is found that, by implementing cryogenic cooling and vibration suppression techniques, optical fibers are capable of performing a broadband search for scalar UDM couplings to photons at sub-Hz frequencies. A fiber-based detector is additionally well-suited to constrain Solar halo UDM models (introduced in Section 5.3.2) for 10^{-3} Hz $\lesssim f_{\rm DM} \lesssim 10^{1}$ Hz.

This chapter is outlined as follows:

- The purpose of Section 5.1 is to describe how a fiber-based detector can be used to search for scalar UDM via its modulation of refractive indices.
- Section 5.2 provides quantitative models of the expected sources of noise, which are summarized in Fig. 5.2.
- Section 5.3 discusses the results in terms of the minimum detectable coupling strength of fiber-based detectors, which can be found in Figs. 5.4 and 5.5 for two different DM models.
- Section 5.4 briefly summarizes the chapter.

Appendix B provides details on the calculations done in this chapter, including a derivation of expressions for the detector's signal and noise, detail on the modulation of refractive

indices by scalar UDM, and an estimate of the mechanical properties of optical fibers that are needed to estimate the thermomechanical noise floor.

5.1 Optical fibers as DM detectors

As discussed in Section 2.2.2, scalar UDM coupled to photons causes an oscillation in fine-structure constant. Fractional fluctuations in α can be expressed in terms of the coupling strength d_e as

$$\frac{\delta\alpha}{\alpha_0}(t) \approx d_e\varphi(t) \approx d_e\varphi_0 \cos(\omega_{\rm DM} t)\,. \tag{5.1}$$

In Chapter 4, the effect this would have on the size of an object through modulation of the Bohr radius was considered. However, the proposed fiber-based detector would be sensitive to scalar UDM through its effect on an optical fiber's refractive index.

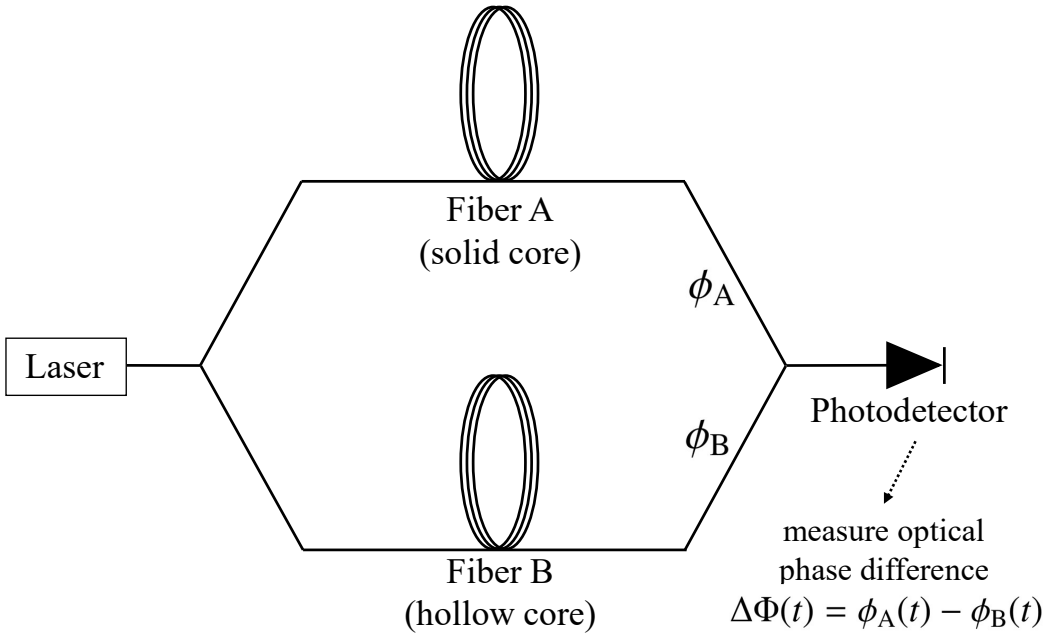

Figure 5.1: Conceptual model for an optical fiber-based detector: Relative oscillations in the refractive indices of two fibers can be detected using a balanced Mach-Zehnder interferometer. Scalar UDM affects the refractive index of the solid core fiber, shifting the optical phase and resulting in an oscillation in output optical power at the UDM frequency. The fiber lengths are chosen to be $L_{0,\rm A} = 10$ km and $L_{0,\rm B} \approx 15$ km.

The refractive index of an optical material generally depends on the fine-structure constant [71, 135], and for small fluctuations in α, the resulting fractional fluctuation in refractive index is[1]

$$\frac{\delta n}{n_0} = \epsilon_{n\alpha} \frac{\delta \alpha}{\alpha_0}. \tag{5.2}$$

While the coefficient $\epsilon_{n\alpha}$ may not be directly measurable, it can be related to a material's optical dispersion[2] as [71, 135]

$$\epsilon_{n\alpha} = -2\epsilon_{n\omega_{\mathrm{L}}}. \tag{5.3}$$

Here it is proposed to search for scalar UDM by comparing the refractive indices of two different types of fibers, solid core and hollow core fibers, which are differentially affected by oscillations in the fine-structure constant. In solid core fibers, the optical mode is contained within silica, for which $\epsilon_{n\omega_{\mathrm{L}},\mathrm{silica}} = 0.013$ at an optical wavelength of 1550 nm (see Appendix B.2.1). In hollow core fibers, the optical mode is mostly contained within air (or vacuum), for which $\epsilon_{n\omega_{\mathrm{L}},\mathrm{air}} \ll \epsilon_{n\omega_{\mathrm{L}},\mathrm{silica}}$ [136, 137].

A simple model for a fiber-based scalar UDM detector is a balanced[3] Mach-Zehnder interferometer, as depicted in Fig. 5.1, where the length of the solid core fiber ($n_{\mathrm{A}} \approx n_{\mathrm{silica}} \approx 1.5$) is 10 km, and the length of the hollow core fiber ($n_{\mathrm{B}} \approx n_{\mathrm{air}} = 1$ [138]) is then ~ 15 km. Oscillations in the relative optical lengths of the fibers can be measured interferometrically using a laser with central wavelength $\lambda_{0,\mathrm{L}} = 1550$ nm.

Generally, both lengths[4] and refractive indices are affected by oscillations in the fine-structure constant. However, both fibers have nearly the same material composition, and the scalar UDM-induced strain signal is nearly material-independent [102], so the strain is common mode to both fibers and does not affect the optical phase difference at the interferometer

---

[1] $\epsilon_{n\alpha} \equiv \frac{\alpha_0}{n_0} \frac{\partial n}{\partial \alpha}\Big|_{\alpha=\alpha_0}$. See Appendix B.1.1 for the definition of the ϵ-coefficients used throughout this chapter to relate fractional changes in various quantities.

[2] $\epsilon_{n\omega_{\mathrm{L}}} \equiv \frac{\omega_{0,\mathrm{L}}}{n_0} \frac{\partial n}{\partial \omega_{\mathrm{L}}}\Big|_{\omega_{\mathrm{L}}=\omega_{0,\mathrm{L}}}$, where $\omega_{0,\mathrm{L}}$ is the laser's center (angular) frequency.

[3] "Balanced" in this context means the time delays introduced by each fiber $\tau_{0,i} = n_{0,i} L_{0,i}/c$ are equal $\tau_{0,\mathrm{A}} = \tau_{0,\mathrm{B}} \equiv \tau_0$.

[4] See Section 2.2.4 for a description of the scalar UDM-induced strain signal.

output. The strain of the laser cavity, however, has an effect on the experiment, as a shift in the laser's central wavelength will affect the fibers' refractive indices via optical dispersion. Therefore, the detector effectively compares the refractive indices of the two fibers, which are differentially influenced by scalar UDM. Small fluctuations in α due to scalar UDM result in a phase difference signal with magnitude[5]

$$\Delta\Phi^{\mathrm{DM}} = \omega_{0,\mathrm{L}}\tau_0\epsilon_{n\omega_{\mathrm{L}},\mathrm{silica}}\frac{\delta\alpha}{\alpha_0}, \tag{5.4}$$

which includes both the direct modulation of the solid core fiber's refractive index by UDM as well as the change in index from optical dispersion (due to UDM shifting the laser wavelength).

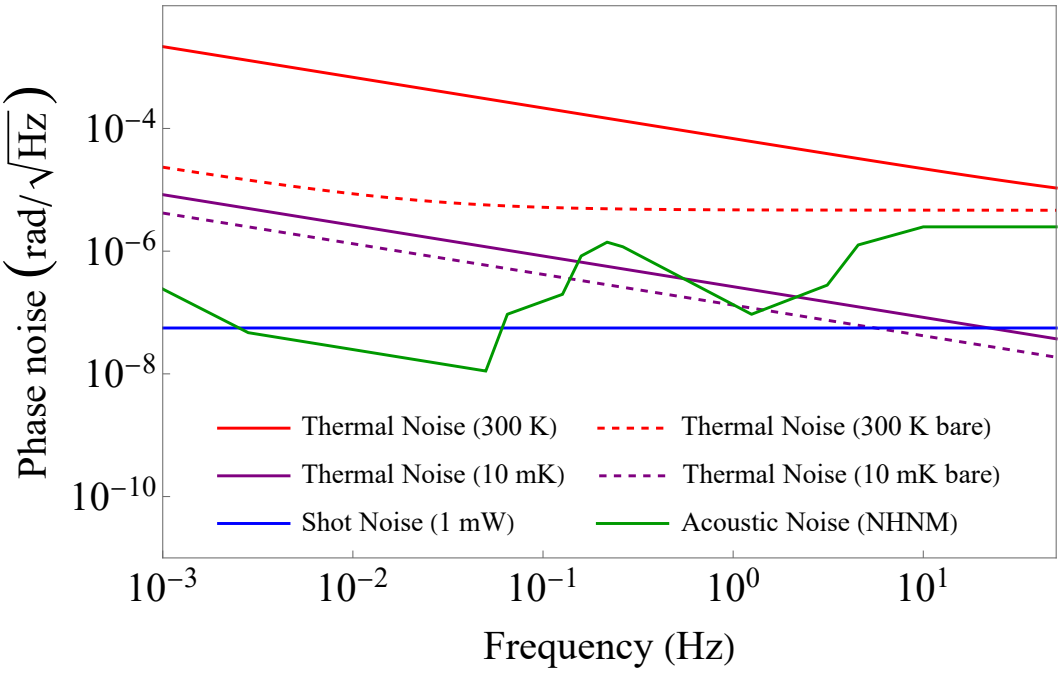

Figure 5.2: Estimated phase noise for the fiber-based detector: Contributions are included from each of the noise sources detailed in Section 5.2. Several thermal noise curves are included, corresponding to fibers with (solid lines) and without (dashed lines) polymer coatings at temperatures of 300 K and 10 mK.

[5] See Appendix B for a detailed treatment of the UDM-induced phase difference.

5.2 Noise analysis

This section provides a discussion of the potential sources of noise that would act to obscure the DM-induced phase difference. The effect of each noise source is quantified by a one-sided phase noise power spectral density (PSD) $S_{\Delta\Phi}(f)$.

5.2.1 Thermal noise in fibers

For the frequency range considered in this chapter ($\sim 10^{-3} - 10^{2}$ Hz), the dominant noise source will likely be thermal noise in the optical fibers, which will induce optical phase fluctuations $\delta\phi$ at the fiber outputs. Thermal noise in fibers includes contributions from two effects, often referred to as "thermomechanical" noise $S_{\delta\phi}^{\mathrm{TM}}$ and "thermoconductive" noise $S_{\delta\phi}^{\mathrm{TC}}$ [139].

Thermomechanical noise refers to spontaneous thermal fluctuations of a fiber's length. The fluctuation-dissipation theorem provides an accurate model for thermomechanical noise in fibers, resulting in a phase noise PSD given by [140]

$$S_{\delta\phi,i}^{\mathrm{TM}}(f) = \left(\frac{2\pi n_{0,i}}{\lambda_{0,\mathrm{L}}}\right)^{2} \frac{2k_{\mathrm{B}}TL_{0,i}\xi_i}{3\pi E_i A_i}\frac{1}{f}, \tag{5.5}$$

where T is the temperature, $L_{0,i}$ is the physical length, ξ_i is the mechanical loss tangent, E_i is the Young's modulus, and A_i is the cross-sectional area of Fiber i.[6] Several experiments have directly measured thermomechanical noise in single mode fibers [141, 142], and the thermomechanical noise model described by Eq. (5.5) has been verified down to frequencies as low as 0.05 Hz [143].

While thermomechanical noise accounts for the spontaneous fluctuations in fiber length due to internal friction, thermoconductive noise results from local temperature fluctuations within an optical fiber [144, 145]. Spontaneous local temperature fluctuations affect the fiber's length and refractive index via thermal expansion and the thermo-optic effect, respectively [139]. Thermoconductive noise is approximately frequency-independent at lower frequencies ($\lesssim 1$ kHz), and scales with temperature and fiber length as $S_{\delta\phi}^{\mathrm{TC}} \propto T^2 L$ [146].

[6] The exact values of the parameters used in this work are discussed in more detail in Appendix B.3.

Thermomechanical noise, scaling as $S_{\delta\phi}^{\mathrm{TC}} \propto TL/f$, dominates at lower frequencies and temperatures. In solid core fibers, $S_{\delta\phi}^{\mathrm{TC}}$ has been estimated using the parameters (for SMF28 [1]) and Eq. (1) from Ref. [142]. Thermoconductive noise in hollow core fibers will be lower than that of solid core fibers due to the reduced thermo-optic effect.

The thermal noise for each fiber is not correlated, so the total differential phase noise at the detector's output due to fiber thermal noise is roughly just the sum of the thermal phase noise in each fiber,

$$S_{\Delta\Phi}^{\mathrm{thermal}} = \sum_i \left(S_{\delta\phi,i}^{\mathrm{TM}} + S_{\delta\phi,i}^{\mathrm{TC}} \right), \tag{5.6}$$

and the thermomechanical contribution will be more significant for the experimental parameters considered here.

The thermal noise floor can be reduced by lowering the temperature. The total thermal noise in the detector is plotted in Fig. 5.2 for both room temperature (300 K) and cryogenic temperature (10 mK).[7] Thermomechanical noise can be further reduced by reducing the fibers' mechanical loss tangents ξ. Mechanical loss in fibers likely comes primarily from the polymer coatings that protect the silica cladding, and there is some evidence suggesting that reducing the thickness of the coatings reduces the thermomechanical noise floor in optical fibers [142], although further investigation is needed to quantify the effect. Fibers with coatings as thin as 10 μm have been demonstrated, without significantly affecting the mechanical strength of the fiber within a laboratory setting [138]. To reduce thermomechanical noise, the use of thinner coatings is suggested. Thermal noise estimates for bare (without coating) fibers[8] are included in Fig. 5.2 as an approximation for thinly-coated fibers. However, it should be noted that bare fibers may be difficult to manufacture and handle due to fragility.

---

[7] Cooling ~25 km of fiber (weighing 1 – 2 kg) to 10 mK is a technical challenge that may require advances in cryogenic technology.

[8] See Appendix B.3 for a discussion of mechanical dissipation in optical fibers.

5.2.2 Laser noise

Interferometric experiments are subject to noise from the driving laser, due to random fluctuations in the optical frequency and intensity.

Laser frequency noise can produce differential phase noise in a balanced interferometer where each arm has different levels of optical dispersion. For the sensitivity of a balanced interferometer to reach the thermal noise floor at 10 mK temperature, laser frequency noise needs to be limited to less than $\sim 10^{-1}\,(\mathrm{Hz}/f)^{1/2}$ Hz·Hz$^{-1/2}$; this would require an ultrastable laser [147].

An alternative approach is presented in Fig. 5.3, where the laser is stabilized to Fiber B, which acts as a delay line in a Mach-Zehnder interferometer. As a result, the laser's frequency noise PSD takes the form of the fiber delay line's (FDL)[9] phase noise PSD:[10] $S_{\delta\nu,\mathrm{L}} = (2\pi\tau_0)^{-2}\, S_{\delta\phi,\mathrm{FDL}}$ [148]. This procedure effectively eliminates laser frequency noise from the analysis, replacing it with phase noise from Fiber B (which would have been present to the same level in a balanced interferometer).

For the detector depicted in Fig. 5.1, the "observable" is the phase difference $\Delta\Phi_\mathrm{A}$. At low frequencies $\left(f_\mathrm{DM} \ll {\tau_0}^{-1}\right)$, this is simply $\Delta\Phi_\mathrm{A} = 2\pi n_\mathrm{A} L_\mathrm{A}/\lambda_\mathrm{L}$ (prior to receiving corrections from the phase modulator). Because the laser is stabilized to Fiber B, the laser wavelength is proportional to the optical path length of Fiber B: $\lambda_\mathrm{L} \propto n_\mathrm{B} L_\mathrm{B}$. Therefore, the detector's function is to compare the optical path lengths of Fibers A and B, as $\Delta\Phi_\mathrm{A}$ is proportional to the ratio $n_\mathrm{A} L_\mathrm{A}/n_\mathrm{B} L_\mathrm{B}$. The balanced interferometer displayed in Fig. 5.1 is still a reasonable conceptual model for the detector, and it can be seen from the derivation for $\Delta\Phi_\mathrm{A}$ in Appendix B that the DM signal from Eq. (5.4) only changes in sign ($\Delta\Phi_\mathrm{A}^\mathrm{DM} = -\Delta\Phi^\mathrm{DM}$) and the phase difference PSD from thermal noise in Eq. (5.6) still holds ($S_{\Delta\Phi,\mathrm{A}}^{\mathrm{thermal}} = S_{\Delta\Phi}^{\mathrm{thermal}}$).

In addition to laser frequency noise, random fluctuations of the laser's optical intensity would limit the sensitivity of a detector like that depicted in Fig. 5.3. Experiments for

[9] Ultra-stable lasers have been demonstrated using FDL-stabilization. For example, a linewidth of 200 mHz has been achieved with a 5 km FDL at room temperature [143].

[10] This relationship holds for low frequencies, as the bandwidth of the control loop is limited by the time delay in the FDL [148]: $f \ll {\tau_0}^{-1} \approx 20$ kHz.

measuring thermal noise in fibers have successfully minimized laser intensity noise to below the thermal noise floor with methods such as heterodyne detection [142] or with the use of differential amplifiers [141]. Assuming these methods are implemented, laser intensity noise is neglected in this analysis.

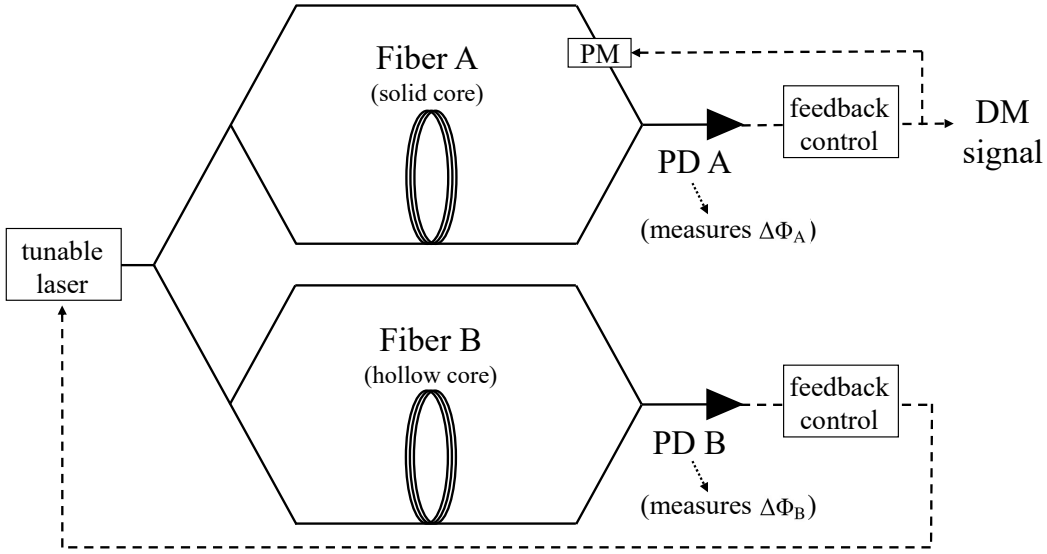

Figure 5.3: Detector model with FDL-stabilized laser: Fiber B serves as a delay line in an interferometer to stabilize a tunable laser. Using feedback from the measurement at Photodetector B (PD B), the laser frequency is tuned such that $\Delta\Phi_B$ remains constant. The phase difference $\Delta\Phi_A$ would then contain the DM signal. The phase difference $\Delta\Phi_A$ depends linearly on the optical power when the recombining beams are kept near quadrature bias ($\Delta\Phi_A \bmod 2\pi = \pi/2$). In the presence of noise and long term instabilities, quadrature bias can be maintained by including a phase modulator (PM) that is driven by feedback from Photodetector A (PD A). The DM signal is then present in the feedback signal supplied to the phase modulator. A derivation for $\Delta\Phi_A$ due to both scalar UDM and noise can be found in Appendix B.1.

5.2.3 Acoustic noise in fibers

Mechanical vibrations, which may originate from a variety of sources such as human activity, natural seismic activity, or local weather, often pose a challenge for terrestrial experiments at low frequencies. Such accelerations deform fibers, altering their optical path

lengths and resulting in phase noise. Here an estimate is provided for the amplitude of mechanical vibrations, which will be generically refered to as "acoustic noise," and techniques will be discussed to potentially reduce the resulting phase noise to a subdominant level.

The USGS New High Noise Model (NHNM) for seismic noise, which can be found in Table 4 in Ref. [149], is used to estimate the effects of mechanical vibrations. The NHNM provides an estimate of seismic acceleration noise S_{aa}^{seismic} for a hypothetical, relatively noisy location on Earth. The estimate is obtained by overlaying spectral measurements of seismic activity from various locations around the world and fitting a piecewise function to the high-noise points of the composite spectrum, ignoring narrow, location-specific peaks. For the frequency range considered in this work ($\sim 10^{-3} - 10^{2}$ Hz), the NHNM roughly predicts an upper bound of

$$S_{aa}^{\text{seismic}} \lesssim 10^{-9} \left(\frac{\text{m}}{\text{s}^2}\right)^2 \text{Hz}^{-1}, \tag{5.7}$$

where both the horizontal and vertical components of the acceleration are approximately equal in magnitude [149, 150]. The NHNM in Ref. [149] extends from 10^{-5} Hz to 10 Hz, which is extrapolated to frequencies above 10 Hz by assuming white acceleration noise $\sim 10^{-9} \left(\frac{\text{m}}{\text{s}^2}\right)^2 \text{Hz}^{-1}$. As a first estimate, it is assumed that seismic noise accounts for all of the vibrations the fibers will experience: $S_{aa}^{\text{acoustic}} \approx S_{aa}^{\text{seismic}}$

To quantify how an acceleration a^{acoustic} affects a strain h^{acoustic} in a spooled fiber, the vibration-sensitivity of the spool is defined as $\Gamma_a \equiv h^{\text{acoustic}}/a^{\text{acoustic}}$. Vibration-induced strains in optical fibers can be suppressed by using low vibration sensitivity fiber spools, a technology designed to reduce frequency noise in fiber delay line (FDL)-stabilized lasers [151]. This technique has been shown to produce ultrastable lasers at room temperature, reaching the thermomechanical noise floor in km-scale fibers at sub-Hz frequencies [143]. Such vibration-insensitive fiber spools have achieved sensitivities $\Gamma_a \lesssim 10^{-11} \left(\text{m/s}^2\right)^{-1}$ to both horizontal and vertical accelerations [152]. Thus, it is expected that acoustic noise induces a strain noise in each fiber on the order of

$$S_{hh}^{\text{acoustic}} = |\Gamma_a|^2 \, S_{aa}^{\text{acoustic}} \lesssim 10^{-31} \, \text{Hz}^{-1}. \tag{5.8}$$

Accounting for the strain-optic effect[11] $\epsilon_{nL,i}$ and differences in optical dispersion $\Delta\epsilon_{n\omega_\mathrm{L}}$,[12] it can be shown that the output phase difference due to strains h_i^{acoustic} in both fibers is (see Appendix B.1)

$$\Delta\Phi_\mathrm{A}^{\mathrm{acoustic}} \approx \omega_{0,\mathrm{L}}\tau_0\left[(1+\epsilon_{nL,\mathrm{A}})\,h_\mathrm{A}^{\mathrm{acoustic}} - (1+\Delta\epsilon_{n\omega_\mathrm{L}}+\epsilon_{nL,\mathrm{B}})\,h_\mathrm{B}^{\mathrm{acoustic}}\right], \tag{5.9}$$

suggesting that acoustic noise can be suppressed by a factor $(\Delta\epsilon_{n\omega_\mathrm{L}} + \Delta\epsilon_{nL}) \approx 10^{-1}$ (see Appendix B.2) in an experiment where the individual fiber strains are correlated and of equal magnitude $h_\mathrm{A}^{\mathrm{acoustic}} = h_\mathrm{B}^{\mathrm{acoustic}}$, so that

$$S_{\Delta\Phi,\mathrm{A}}^{\mathrm{acoustic}} = \left|\omega_{0,\mathrm{L}}\tau_0\,(\Delta\epsilon_{n\omega_\mathrm{L}} + \Delta\epsilon_{nL})\right|^2 S_{hh}^{\mathrm{acoustic}}. \tag{5.10}$$

This can be accomplished by cowinding the fibers on a spool or cylinder, a technique that has been used to observe the thermal noise floor in fiber-based interferometers [141, 142]. By cowinding both fibers on a single spool with $\Gamma_a \lesssim 10^{-11}\left(\mathrm{m/s^2}\right)^{-1}$, acoustic noise at the level predicted by the NHNM can be reduced to a level comparable to that of thermal noise in this experiment, as can be seen in Fig. 5.2.

Note, however, that some locations, particularly urban environments, may be subject to anthropogenic vibrations that exceed the NHNM, in which case additional measures may need to be taken to isolate against vibrations (active or passive vibration isolation platforms). Further suppression of vibration-induced phase noise can also be achieved using the feedforward method [153, 154].

5.2.4 Photon shot noise and optical power

The phase difference $\Delta\Phi$ between the arms of an interferometer is inferred by measuring the output optical power P after the junction where the arms recombine. Assuming that the recombining beams have equal optical power and are maintained at quadrature bias,[13]

[11] $\epsilon_{nL} \equiv \frac{L_0}{n_0}\frac{\partial n}{\partial L}\Big|_{L=L_0}$. Also see Appendix B.2.2 for discussion of the strain-optic effect in fibers.

[12] Differences in the ϵ-coefficients for the fibers are defined as $\Delta\epsilon_{wv} \equiv \epsilon_{wv,\mathrm{A}} - \epsilon_{wv,\mathrm{B}}$.

[13] At quadrature bias, the average phase difference between recombining beams at an interferometer's output is $\langle\Delta\Phi\rangle \bmod 2\pi = \pi/2$.

the PSDs of the phase difference and output optical power fluctuations ΔP are related by $S_{\Delta\Phi} = S_{\Delta P}/\langle P\rangle^2$, where $\langle P\rangle$ is the average output optical power.

Photon shot noise imposes a limit on the sensitivity of interferometric measurements, as small fluctuations in the measured optical power due to shot noise are indistinguishable from small phase fluctuations in an interferometer.[14] The one-sided PSD of the fluctuations in measured optical power due to shot noise is [103]

$$S_{\Delta P}^{\text{shot}} = \frac{2hc}{\lambda_{0,\text{L}}}\langle P\rangle\,. \tag{5.11}$$

For simplicity, it is assumed that the optical power splitting ratio at each fiber junction is adjusted so that the optical power imminent on each photodetector is equal. In this case, it can be shown that the average power on each photodetector is

$$\langle P\rangle = \frac{P_{\text{L}}}{2 + 10^{\gamma_{\text{B}}L_{\text{B}}} + 10^{\gamma_{\text{A}}L_{\text{A}}}}, \tag{5.12}$$

where γ_i is the optical loss of Fiber i and P_{L} is the optical power coming from the laser. The total contribution of shot noise to the differential phase noise of the detector is

$$S_{\Delta\Phi,\text{A}}^{\text{shot}} = \frac{4hc}{\lambda_{0,\text{L}}P_{\text{L}}}\left(2 + 10^{\gamma_{\text{B}}L_{\text{B}}} + 10^{\gamma_{\text{A}}L_{\text{A}}}\right), \tag{5.13}$$

which is simply double the shot noise measured at each detector (see Appendix B.1).

The effects of shot noise can be reduced by increasing the optical power. Figure 5.2 shows that a detector with bare fibers, operating at $T = 10$ mK, achieves a noise floor (combined thermomechanical and acoustic noise) of $\gtrsim 10^{-7}\text{rad}/\sqrt{\text{Hz}}$. Reducing the total shot noise in this experiment to the subdominant level of $\sqrt{S_{\Delta\Phi,\text{A}}^{\text{shot}}} \lesssim 10^{-7}\text{rad}/\sqrt{\text{Hz}}$ requires an average optical power on each photodetector of $\langle P\rangle \gtrsim 50\,\mu\text{W}$.

In order minimize the laser power needed to produce the desired output optical power, it is important to use fibers with minimal optical loss. Recent advances in hollow core fiber technology have yielded hollow core fibers with a propagation loss of 0.17 dB/km (γ =

[14] Optical power fluctuations due to photon shot noise should be distinguished from laser intensity noise, as discussed in Section 5.2.2. The effects of photon shot noise are not reduced by the same methods that would reduce the effects of laser intensity noise, such as heterodyne detection [142] or balanced photodetection [141].

1.7×10^{-5} m^{-1}) at $\lambda_{0,\mathrm{L}} = 1550$ nm [155], reaching the level of low-loss solid core fibers (0.18 dB/km for SMF28 [1]).

In Fig. 5.2, the total shot noise is plotted for a detector with a 10 km solid core and $\sim$ 15 km hollow core fiber, assuming a laser power of $P_{\mathrm{L}} = 1$ mW. To account for optical loss, the optical power being diverted into the solid and hollow core fibers would be 0.25 mW and 0.42 mW, respectively, and the power reaching each photodetector would be $\langle P \rangle = 0.16$ mW.[15]

5.3 Potential of a DM search with optical fibers

5.3.1 Minimum detectable coupling strength

The minimum detectable DM-induced phase difference is approximately

$$\Delta\Phi^{\mathrm{DM}}_{\mathrm{A,min}} \approx \sqrt{2S^{\mathrm{noise}}_{\Delta\Phi,\mathrm{A}}}\left[3{\tau_{\mathrm{int}}}^{-1/2} + (\tau_{\mathrm{DM}}\tau_{\mathrm{int}})^{-1/4}\right], \tag{5.14}$$

where $S^{\mathrm{noise}}_{\Delta\Phi,\mathrm{A}}$ includes contributions from the noise sources discussed in Section 5.2.

The minimum detectable coupling strength $d_{e,\mathrm{min}}$ of the detector is then

$$d_{e,\mathrm{min}} = \frac{\Delta\Phi^{\mathrm{DM}}_{\mathrm{A,min}}}{\omega_{0,\mathrm{L}}\tau_0\epsilon_{n\omega_{\mathrm{L}},\mathrm{silica}}\varphi_{\mathrm{rms}}}. \tag{5.15}$$

Figure 5.4 compares the $d_{e,\mathrm{min}}$ of fiber-based DM detectors with the current constraints on d_e in the frequency range 10^{-3} Hz $\leq f_{\mathrm{DM}} \leq 10^2$ Hz, assuming a measurement time $\tau_{\mathrm{int}} = 1$ year. The solid red represents a room temperature experiment, and is limited by thermal noise. Cryogenic cooling will be necessary to set new constraints on d_e with a single fiber-based detector; purple curves represent a detector operating at 10 mK.

Additionally, fibers with thinner polymer coatings can be utilized reduce thermomechanical noise. As a benchmark, Fig. 5.4 includes the projected $d_{e,\mathrm{min}}$ for detectors where the coatings have been entirely removed (bare) as dashed curves. It is clear from the figure that the benefit of removing the coatings diminishes at lower temperature, where the intrinsic

[15] For a cryogenic experiment, the optical power dissipated in the system sets minimum requirements on the cooling power of the refrigerator. Cooling powers on the order of 1 mW at 10 mK temperature may not be achievable with existing dilution refrigerator systems [156].

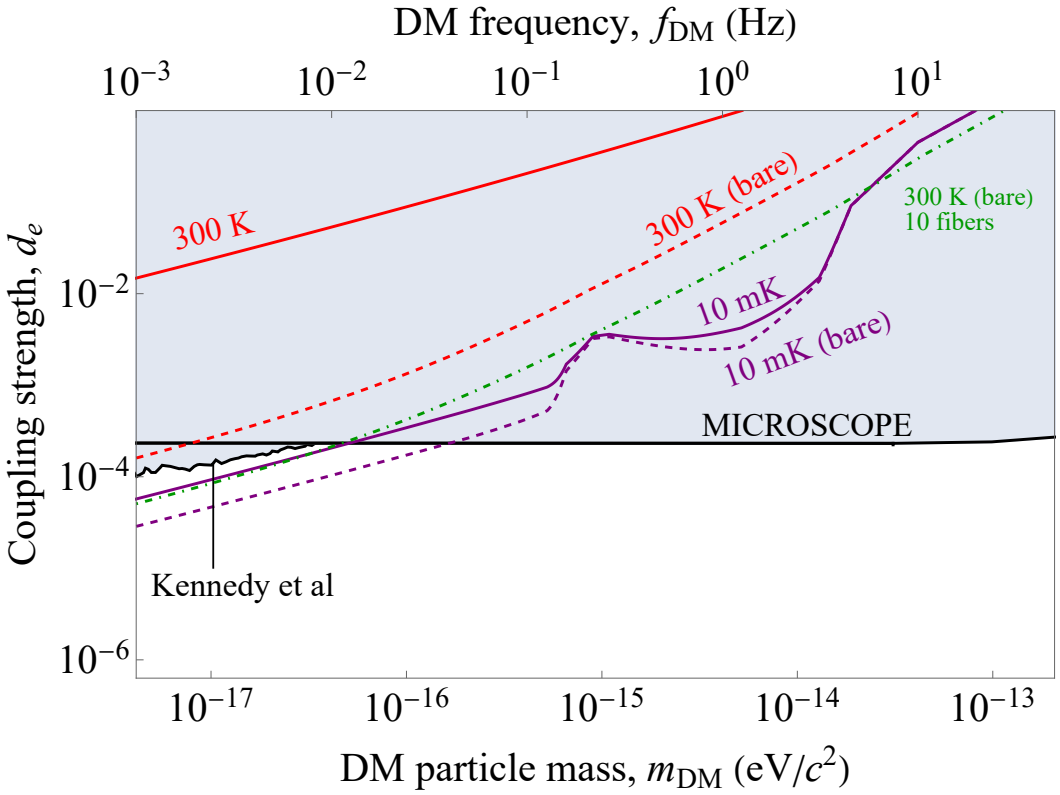

Figure 5.4: Projected constraints on d_e from optical fibers, assuming a Galactic DM halo: The projected constraints from fiber-detectors operating at temperatures of 300 K and 10 mK, with (solid) and without (dashed) polymer coatings, for an integration time $\tau_{\rm int}$ = 1 year. The detectors are primarily limited by thermal noise; cryogenic detectors are limited by acoustic noise at higher frequencies (above $\sim 10^{-1}$ Hz). Also included are projected constraints from an array of 10 detectors, using bare fiber at room temperature. The strongest experimental constraints in this mass range come from MICROSCOPE [6] and Kennedy et al [18]. The fiber-based detectors proposed here can potentially probe new regions of the parameter space below $\sim 10^{-1}$ Hz.

mechanical loss tangent ξ of fused silica increases beyond its room-temperature value. It is also important to note that, while fiber coatings can be made quite thin [138], the fragility of bare optical fibers may present a significant challenge to constructing a detector.

The combined sensitivity of an array of N detectors (subject to uncorrelated noise) generally improves with $N^{-1/2}$ [66]. Also included are the expected constraints from an array of 10 independent detectors with bare fibers in green, which would enable room-temperature

optical fibers to set new constraints on d_e.

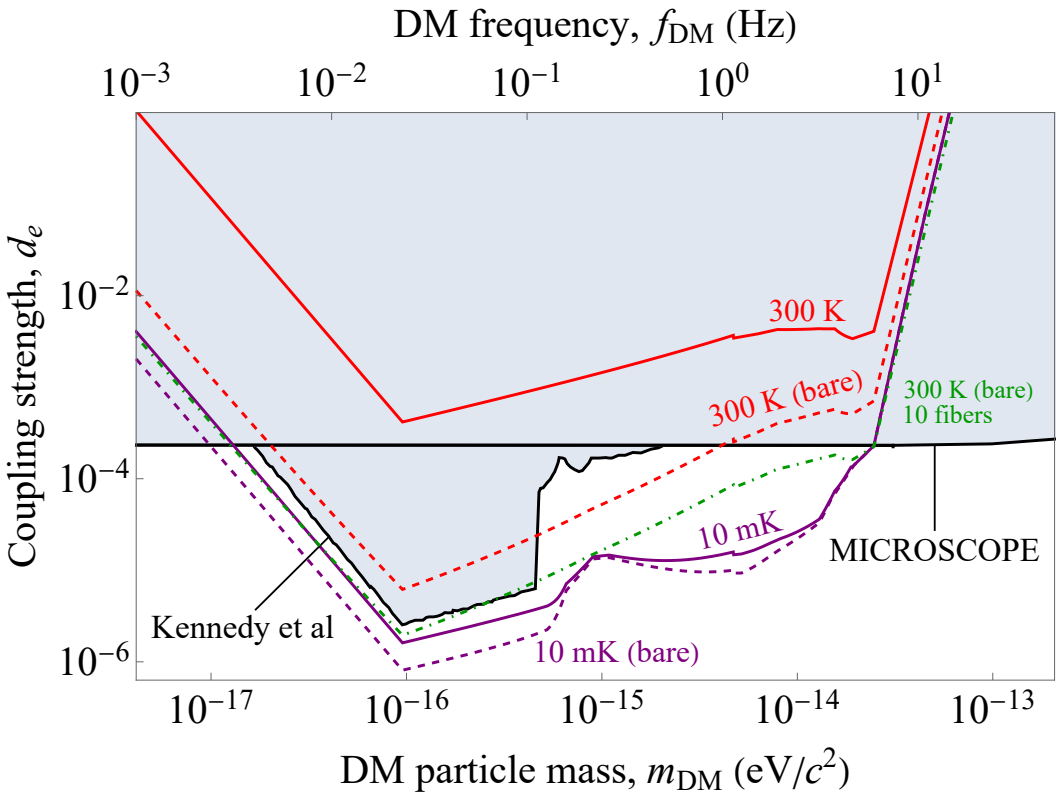

Figure 5.5: Projected constraints on d_e from optical fibers, assuming a Solar DM halo: The projected constraints from fibers, as well as the experimental constraints from Ref. [18], are re-scaled from Fig. 5.4 according to a Solar halo's expected density and coherence time. Constraints from the MICROSCOPE EP test do not depend on the DM energy density $\rho_{\rm DM}$ and are unchanged from Fig. 5.4.

5.3.2 Solar DM halo model

It is worth noting that the optical fiber detectors proposed in this chapter are well-suited to probe an alternative dark matter model where UDM forms a halo centered on the Sun, a well-motivated scenario in the particle mass range $10^{-17}\,\text{eV} \lesssim m_{\rm DM}c^2 \lesssim 10^{-13}$ eV [157].

In Section 1.1, the Standard Halo Model was described for dark matter in the Milky Way, which assumes a density profile that decreases with distance from the center of the Galaxy $\rho_{\rm DM}(r) \propto r^{-2}$ [3]. Throughout this dissertation, it has also been implicitly assumed

that this Galactic halo is smooth, lacking any noticeable substructure. Referred to as the "Galactic halo model," this is the most commonly-used model for DM in direct detection experiments. In the Galactic halo model, the dark matter density and coherence time at Earth take on values determined by the average density and velocity dispersion within the entire Solar Neighborhood (averaged over a few hundred parsecs): $\rho_{\rm DM} \approx 0.4$ GeV/cm^3 [3] and $\tau_{\rm DM} \approx 10^6 \omega_{\rm DM}{}^{-1}$ [4]. However, DM may have a drastically different local substructure that remains consistent with the Standard Halo Model on larger scales.

It is possible that DM forms gravitationally bounded objects, which could potentially form a halo bound to an external gravitational source, such as the Sun or Earth [157]. In this scenario, the local DM halo could have a greater density and coherence time at Earth than in the Galactic halo model, leading to potentially stronger constraints on coupling strength from direct detection experiments. The halo's size and density would generally depend on the mass of the DM particles. Earth halos are well-motivated at particle masses $10^{-13}\,\text{eV} \lesssim m_{\rm DM}c^2 \lesssim 10^{-7}$ eV [157], and several recent experiments have set constraints on the Earth halo model for DM [19, 21, 23, 26, 27].

A fiber-based detector is aptly suited to search for a local DM halo that is gravitationally bound to the Sun, as such Solar halos are well-motivated in the particle mass range $10^{-17}\,\text{eV} \lesssim m_{\rm DM}c^2 \lesssim 10^{-13}$ eV [157]. In this range, a Solar halo could have an energy density up to $\sim 10^5$ times greater than that of a Galactic halo. To recalculate $d_{e,\rm min}$ for a Solar DM halo, $\rho_{\rm DM}$ is re-scaled using Supplementary Figure 2 from Ref. [157] and the coherence time becomes $\tau_{\rm DM} = 10^8 \text{s} \left(\frac{1\text{Hz}}{f_{\rm DM}}\right)^3$ [158]. The projected constraints from optical fibers, using a Solar halo model for DM, are plotted in Fig. 5.5. Constraints on d_e from previous experiments have also been re-scaled accordingly.

5.4 Conclusion

In summary, optical fibers can be used to search for scalar UDM-induced oscillation in the fine-structure constant α via refractive index effects. While terrestrial experiments are often made difficult at low ($\lesssim$ 1 Hz) frequencies by seismic noise, acoustic isolation and

suppression techniques have been demonstrated in km-scale optical fibers, enabling a fiber-based detector to reach a limit set by the thermomechanical noise floor. Thermal noise can be reduced with cryogenic cooling, thinner protective fiber coatings, and detector arrays. These methods enable fibers to perform broadband searches for scalar UDM coupling to photons at sub-Hz frequencies, supplementing the compact mechanical resonators (which operate at $\gtrsim 100$ Hz) from Chapter 4.

Additionally, a fiber-based detector would be particularly well-suited to search for Solar DM halos in the $10^{-17} - 10^{-13}$ eV mass range. In the context of a Solar halo, fibers can be used to set novel constraints over three decades of bandwidth ($\sim 10^{-2} - 10^{1}$ Hz).

Chapter 6

SUMMARY AND FUTURE WORK

6.1 Summary

Dark matter is the dominant form of matter in the Universe, yet its composition is unknown. The uncertainty in dark matter's composition spans 90 orders of magnitude in particle/object mass [60]. Of the many existing theories for dark matter, this work has focused on ultralight dark matter, which is expected to produce weak coherent signals that could be detected by compact, but high-precision, systems. In this dissertation, novel detectors have been presented to search for several vector and scalar UDM candidates, including optomechanical membranes, a variety of compact mechanical resonators, and optical fibers, providing an avenue for small-scale experiments to cover a region of the ultralight dark matter parameter space from $10^{-17} - 10^{-6}$ eV/c^2 particle mass.

Centimeter-scale silicon nitride membranes can be used to perform vector UDM searches in the 1-100 kHz frequency range $\left(10^{-11}\text{-}10^{-10}\ \text{eV}/c^2\right)$. Membranes with high-quality mechanical oscillation modes can resonantly amplify the vector UDM force signal, achieving the best sensitivities over narrow bandwidths near the resonance frequencies. When coupled to an optical cavity for displacement readout, an optomechanical membrane dark matter detector is capable of reaching the thermal noise floor on-resonance. The detector's small size facilitates cryogenic cooling, which will be necessary to exceed the bounds on the vector UDM coupling strength set by previous experiments. Furthermore, the tunability of silicon nitride membranes' mechanical modes enables frequency scan search techniques to effectively increase the detection bandwidth of each mechanical mode.

Similarly, this work has shown that the concept of resonant-mass detection can be applied to laboratory-scale experiments for scalar UDM across the Hz-MHz frequency range

$\left(10^{-12} - 10^{-6}\ \mathrm{eV}/c^2\right)$. Existing and near-term compact mechanical resonators based in high quality materials (superfluid and crystalline solids) naturally achieve high mechanical quality factors for resonant amplification of the UDM signal. Again, cryogenic cooling and cavity optomechanical readout enable on-resonance sensitivities capable of reaching unexplored regions of the scalar UDM parameter space, where detector arrays, frequency scanning, and simultaneous monitoring of higher-order mechanical modes can be used to enhance bandwidth.

To supplement mechanical resonators in the search for scalar UDM, optical fibers can be used to construct a broadband detector at sub-Hz frequencies $\left(10^{-17}\ \text{-}\ 10^{-13}\ \mathrm{eV}/c^2\right)$. The lack of resonant amplification can be compensated for in fibers simply by their long (several kilometers) length. With optical propagation losses below 0.2 dB/km, an optical cavity is not necessary to reduce readout imprecision due to photon shot noise to a subdominant level for $\sim$ mW input laser power. However, optical fibers experience relatively high mechanical loss and are susceptible to vibrations. Therefore, thermomechanical and acoustic noise place stricter limits on the sensitivity of a fiber-based detector than on high-quality mechanical resonators. Nevertheless, relying on cryogenic cooling or fiber detector arrays, a case has been made for optical fibers as next-generation UDM detectors, encouraging further investigation of cryogenically-cooled and acoustically-shielded fibers as DM detectors.

6.2 Suggestions for future work

The process of analyzing experimental data deserves additional consideration, as the minimum detectable signal in an experiment will depend on the data analysis method. The expression for the minimum detectable signal (Eq. 2.55) used in this dissertation is a reasonable approximation for measurement times τ_{int} significantly shorter than or longer than the DM coherence time τ_{DM} [104]. For $\tau_{\mathrm{int}} \ll \tau_{\mathrm{DM}}$, the signal is approximately coherent and entirely contained within a single frequency bin of the discrete Fourier transform. For $\tau_{\mathrm{int}} \gg \tau_{\mathrm{DM}}$, the signal power is spread across many frequency bins, which can be averaged over to effectively increase the signal-to-noise ratio. The exact scaling of the minimum detectable signal with measurement time when $\tau_{\mathrm{int}} \approx \tau_{\mathrm{DM}}$ is unclear, as the signal is spread

unequally across a small number of frequency bins. This detail is important for optimizing a frequency scan, for example, which will likely be necessary for a thorough UDM search using resonant detectors. Furthermore, experimental constraints on coupling strength are typically derived using a Bayesian framework, and it is not yet clear how compatible these two approaches are in the regime $\tau_{\text{int}} \approx \tau_{\text{DM}}$ for UDM, whose stochastic nature has only recently been taken into consideration [65]. Additional data processing details that were not included in this work, such as managing gaps in the data [159] and processing data from detector arrays [160], can likely be borrowed from the fields of astronomy, gravitational wave detection, and axion ultralight dark matter searches [161, 162].

As a superfluid helium detector for scalar UDM is currently being built at the University of Alberta [134], additional theoretical analyses will be required. Specifically, the overlap factor α_i should be recalculated for the exact modes of the detector. The overlap factor will likely differ from the estimate in Chapter 4, as 1) the fully constructed detector is expected to have different acoustic boundary conditions and 2) the modeshapes will not be purely longitudinal. Furthermore, the sensitivity of the superfluid helium resonator to vector UDM is an interesting prospect that has not yet been considered. Assuming fixed acoustic boundaries, the even-ordered acoustic modes are sensitive to strains (scalar UDM), while the odd-ordered modes would be sensitive to accelerations (vector UDM). A search for both vector and scalar UDM can be run simultaneously, although the detector may need modification to gain sensitivity to the material-dependent vector UDM-induced acceleration. In theory, this can be achieved by using a container composed of a material that has a different neutron fraction than the superfluid helium. Alternatively, a relatively large mass of the material could simply be rigidly fixed to the container. A theoretical treatment of the vector UDM-coupling to the detector modes would be required to determine the minimum detectable coupling strength. However, a rough estimate can be given using the detector described in Chapter 4: with an acceleration sensitivity of $\sim 10^{-14}$ m·s^{-2}·Hz$^{-1/2}$, the current constraints on vector $B - L$ UDM (see Section 3.2.1) at $\sim$ 1 kHz can be exceeded in an integration time of seconds, assuming $\Delta_{12} = 0.05$. Therefore, a superfluid helium detector can be used to supplement the vector UDM search using optomechanical membranes that is

currently in preparation at the University of Arizona [117] based on the work presented in this dissertation.

Looking forward, a natural extension of this work is to consider mechanical detectors operating in the quantum regime [163]. The systems discussed in this proposal are predominantly classical in nature; quantum effects have not been considered in detail beyond shot noise in the optical readout. Mechanical oscillators, when cooled such that $k_{\mathrm{B}}T < \hbar\omega_m$, are said to be operating in the "quantum regime," where quantum zero-point fluctuations (described by the Heisenberg uncertainty principle) dominate over thermal fluctuations. Sensors operating in the quantum regime will generally achieve better sensitivities, however the noise analyses presented here will no longer apply. Furthermore, the next-generation of UDM searches may explore additional quantum effects such as entanglement between detectors, as a network of entangled detectors achieves better noise-reduction than can be achieved with a network of independent detectors [164].

Bibliography

[1] Corning. *Corning SMF-28 Ultra Optical Fiber Product Information*, 2014.

[2] Gregory T Jasion, Thomas D Bradley, Kerrianne Harrington, Hesham Sakr, Yong Chen, Eric Numkam Fokoua, Ian A Davidson, Austin Taranta, John R Hayes, David J Richardson, et al. Hollow core nanf with 0.28 db/km attenuation in the c and l bands. In *Optical Fiber Communication Conference*, pages Th4B–4. Optical Society of America, 2020.

[3] Particle Data Group, PA Zyla, RM Barnett, J Beringer, O Dahl, DA Dwyer, DE Groom, C-J Lin, KS Lugovsky, E Pianori, et al. Review of particle physics. *Progress of Theoretical and Experimental Physics*, 2020(8):083C01, 2020.

[4] Andrei Derevianko. Detecting dark-matter waves with a network of precision-measurement tools. *Phys. Rev. A*, 97(4):042506, 2018.

[5] D Antypas, A Banerjee, C Bartram, M Baryakhtar, J Betz, JJ Bollinger, C Boutan, D Bowring, D Budker, D Carney, et al. New horizons: Scalar and vector ultralight dark matter. *arXiv preprint arXiv:2203.14915*, 2022.

[6] Joel Bergé, Philippe Brax, Gilles Métris, Martin Pernot-Borràs, Pierre Touboul, and Jean-Philippe Uzan. Microscope mission: first constraints on the violation of the weak equivalence principle by a light scalar dilaton. *Phys. Rev. Lett.*, 120(14):141101, 2018.

[7] Pierre Touboul, Gilles Métris, Manuel Rodrigues, Yves André, Quentin Baghi, Joël Bergé, Damien Boulanger, Stefanie Bremer, Patrice Carle, Ratana Chhun, et al. Microscope mission: first results of a space test of the equivalence principle. *Phys. Rev. Lett.*, 119(23):231101, 2017.

[8] T. A. Wagner, S. Schlamminger, J. H. Gundlach, and E. G. Adelberger. Torsion-balance tests of the weak equivalence principle. *Class. Quant. Grav.*, 29:184002, 2012.

[9] E. A. Shaw, M. P. Ross, C. A. Hagedorn, E. G. Adelberger, and J. H. Gundlach. Torsion-balance search for ultralow-mass bosonic dark matter. *Phys. Rev. D*, 105(4):042007, 2022.

[10] Soichiro Morisaki, Tomohiro Fujita, Yuta Michimura, Hiromasa Nakatsuka, and Ippei Obata. Improved sensitivity of interferometric gravitational wave detectors to ultralight vector dark matter from the finite light-traveling time. *Phys. Rev. D*, 103(5):L051702, 2021.

[11] R. Abbott et al. Constraints on dark photon dark matter using data from LIGO's and Virgo's third observing run. 5 2021.

[12] G. L. Smith, C. D. Hoyle, J. H. Gundlach, E. G. Adelberger, B. R. Heckel, and H. E. Swanson. Short-range tests of the equivalence principle. *Phys. Rev. D*, 61:022001, Dec 1999.

[13] Stephan Schlamminger, K-Y Choi, Todd A Wagner, Jens H Gundlach, and Eric G Adelberger. Test of the equivalence principle using a rotating torsion balance. *Phys. Rev. Lett.*, 100(4):041101, 2008.

[14] Aurélien Hees, Olivier Minazzoli, Etienne Savalle, Yevgeny V. Stadnik, and Peter Wolf. Violation of the equivalence principle from light scalar dark matter. *Phys. Rev. D*, 98(6):064051, 2018.

[15] Ken Van Tilburg, Nathan Leefer, Lykourgos Bougas, and Dmitry Budker. Search for ultralight scalar dark matter with atomic spectroscopy. *Physical review letters*, 115(1):011802, 2015.

[16] A Hees, J Guéna, Michel Abgrall, S Bize, and P Wolf. Searching for an oscillating massive scalar field as a dark matter candidate using atomic hyperfine frequency comparisons. *Physical review letters*, 117(6):061301, 2016.

[17] Kyle Beloy and Martha I Bodine. Frequency ratio measurements at 18-digit accuracy using an optical clock network. *Nature*, 591(7851), 2021.

[18] Colin J Kennedy, Eric Oelker, John M Robinson, Tobias Bothwell, Dhruv Kedar, William R Milner, G Edward Marti, Andrei Derevianko, and Jun Ye. Precision metrology meets cosmology: improved constraints on ultralight dark matter from atom-cavity frequency comparisons. *Physical Review Letters*, 125(20):201302, 2020.

[19] Shahaf Aharony, Nitzan Akerman, Roee Ozeri, Gilad Perez, Inbar Savoray, and Ravid Shaniv. Constraining rapidly oscillating scalar dark matter using dynamic decoupling. *Physical Review D*, 103(7):075017, 2021.

[20] William M. Campbell, Ben T. McAllister, Maxim Goryachev, Eugene N. Ivanov, and Michael E. Tobar. Searching for scalar dark matter via coupling to fundamental constants with photonic, atomic, and mechanical oscillators. *Phys. Rev. Lett.*, 126:071301, Feb 2021.

[21] D Antypas, O Tretiak, A Garcon, R Ozeri, G Perez, and D Budker. Scalar dark matter in the radio-frequency band: atomic-spectroscopy search results. *Physical Review Letters*, 123(14):141102, 2019.

[22] Oleg Tretiak, Xue Zhang, Nataniel L Figueroa, Dionysios Antypas, Andrea Brogna, Abhishek Banerjee, Gilad Perez, and Dmitry Budker. Improved bounds on ultralight scalar dark matter in the radio-frequency range. *arXiv preprint arXiv:2201.02042*, 2022.

[23] R Oswald, A Nevsky, V Vogt, S Schiller, NL Figueroa, K Zhang, O Tretiak, D Antypas, D Budker, A Banerjee, et al. Search for oscillations of fundamental constants using molecular spectroscopy. *arXiv preprint arXiv:2111.06883*, 2021.

[24] Antonio Branca, Michele Bonaldi, Massimo Cerdonio, Livia Conti, Paolo Falferi, Francesco Marin, Renato Mezzena, Antonello Ortolan, Giovanni A. Prodi, Luca Taffarello, Gabriele Vedovato, Andrea Vinante, Stefano Vitale, and Jean-Pierre Zendri. Search for an ultralight scalar dark matter candidate with the auriga detector. *Phys. Rev. Lett.*, 118:021302, Jan 2017.

[25] Sander M Vermeulen, Philip Relton, Hartmut Grote, Vivien Raymond, Christoph Affeldt, Fabio Bergamin, Aparna Bisht, Marc Brinkmann, Karsten Danzmann, Suresh Doravari, et al. Direct limits for scalar field dark matter from a gravitational-wave detector. *Nature*, 600(7889):424–428, 2021.

[26] Etienne Savalle, Aurélien Hees, Florian Frank, Etienne Cantin, Paul-Eric Pottie, Benjamin M Roberts, Lucie Cros, Ben T McAllister, and Peter Wolf. Searching for dark matter with an optical cavity and an unequal-delay interferometer. *Physical Review Letters*, 126(5):051301, 2021.

[27] Lorenzo Aiello, Jonathan W Richardson, Sander M Vermeulen, Hartmut Grote, Craig Hogan, Ohkyung Kwon, and Chris Stoughton. Constraints on scalar field dark matter from twin co-located power-recycled michelson interferometers. *arXiv e-prints*, pages arXiv–2108, 2021.

[28] G.G. Raffelt. *Stars as Laboratories for Fundamental Physics: The Astrophysics of Neutrinos, Axions, and Other Weakly Interacting Particles*. Theoretical Astrophysics. University of Chicago Press, 1996.

[29] Mahiro Abe, Philip Adamson, Marcel Borcean, Daniela Bortoletto, Kieran Bridges, Samuel P Carman, Swapan Chattopadhyay, Jonathon Coleman, Noah M Curfman, Kenneth DeRose, Tejas Deshpande, Savas Dimopoulos, Christopher J Foot, Josef C Frisch, Benjamin E Garber, Steve Geer, Valerie Gibson, Jonah Glick, Peter W Graham, Steve R Hahn, Roni Harnik, Leonie Hawkins, Sam Hindley, Jason M Hogan, Yijun Jiang, Mark A Kasevich, Ronald J Kellett, Mandy Kiburg, Tim Kovachy, Joseph D Lykken, John March-Russell, Jeremiah Mitchell, Martin Murphy, Megan

Nantel, Lucy E Nobrega, Robert K Plunkett, Surjeet Rajendran, Jan Rudolph, Natasha Sachdeva, Murtaza Safdari, James K Santucci, Ariel G Schwartzman, Ian Shipsey, Hunter Swan, Linda R Valerio, Arvydas Vasonis, Yiping Wang, and Thomas Wilkason. Matter-wave Atomic Gradiometer Interferometric Sensor (MAGIS-100). *Quantum Science and Technology*, 6(4):044003, Jul 2021.

[30] Asimina Arvanitaki, Junwu Huang, and Ken Van Tilburg. Searching for dilaton dark matter with atomic clocks. *Physical Review D*, 91(1):015015, 2015.

[31] Ivan Kozyryev, Zack Lasner, and John M Doyle. Enhanced sensitivity to ultralight bosonic dark matter in the spectra of the linear radical sroh. *Physical Review A*, 103(4):043313, 2021.

[32] Andrew A. Geraci et al. Searching for Ultralight Dark Matter with Optical Cavities. *Phys. Rev. Lett.*, 123(3):031304, 2019.

[33] Jack Manley, Dalziel J Wilson, Russell Stump, Daniel Grin, and Swati Singh. Searching for scalar dark matter with compact mechanical resonators. *Physical Review Letters*, 124(15):151301, 2020.

[34] Asimina Arvanitaki, Savas Dimopoulos, and Ken Van Tilburg. Sound of dark matter: searching for light scalars with resonant-mass detectors. *Physical review letters*, 116(3):031102, 2016.

[35] Katelin Schutz. Subhalo mass function and ultralight bosonic dark matter. *Phys. Rev. D*, 101(12):123026, June 2020.

[36] E. O. Nadler et al. Milky Way Satellite Census. III. Constraints on Dark Matter Properties from Observations of Milky Way Satellite Galaxies. *Phys. Rev. Lett.*, 126:091101, 2021.

[37] Keir K. Rogers and Hiranya V. Peiris. Strong Bound on Canonical Ultralight Axion Dark Matter from the Lyman-Alpha Forest. *Phys. Rev. Lett.*, 126(7):071302, February 2021.

[38] Takeshi Kobayashi et al. Lyman-α constraints on ultralight scalar dark matter: Implications for the early and late universe. *Phys. Rev. D*, 96(12):123514, 2017.

[39] Vid Iršič, Matteo Viel, Martin G. Haehnelt, James S. Bolton, and George D. Becker. First Constraints on Fuzzy Dark Matter from Lyman-α Forest Data and Hydrodynamical Simulations. *Phys. Rev. Lett.*, 119(3):031302, July 2017.

[40] Eric Armengaud et al. Constraining the mass of light bosonic dark matter using sdss lyman-α forest. *MNRAS*, 471(4):4606–4614, 2017.

[41] Alex Drlica-Wagner et al. Probing the Fundamental Nature of Dark Matter with the Large Synoptic Survey Telescope. 2 2019.

[42] Jack Manley, Mitul Dey Chowdhury, Daniel Grin, Swati Singh, and Dalziel J Wilson. Searching for vector dark matter with an optomechanical accelerometer. *Physical Review Letters*, 126(6):061301, 2021.

[43] Huai-Ke Guo, Keith Riles, Feng-Wei Yang, and Yue Zhao. Searching for dark photon dark matter in ligo o1 data. *Commun. Phys.*, 2(1):1–7, 2019.

[44] S Rowan et al. Investigation of mechanical loss factors of some candidate materials for the test masses of gravitational wave detectors. *Phys. Lett. A*, 265(1-2):5–11, 2000.

[45] Maxim Goryachev and Michael E. Tobar. Gravitational Wave Detection with High Frequency Phonon Trapping Acoustic Cavities. *Phys. Rev.*, D90(10):102005, 2014.

[46] Serge Galliou et al. Extremely Low Loss Phonon-Trapping Cryogenic Acoustic Cavities for Future Physical Experiments. *Scientific Reports*, 3:2132, Jul 2013.

[47] S. Dimopoulos and G. F. Giudice. Macroscopic forces from supersymmetry. *Phys. Lett.*, B379:105–114, 1996.

[48] Asimina Arvanitaki et al. Search for light scalar dark matter with atomic gravitational wave detectors. *Phys. Rev.*, D97(7):075020, 2018.

[49] Vera C Rubin and W Kent Ford Jr. Rotation of the andromeda nebula from a spectroscopic survey of emission regions. *The Astrophysical Journal*, 159:379, 1970.

[50] Fritz Zwicky. The redshift of extragalactic nebulae. *Helvetica Physica Acta*, 6:110–127, 1933.

[51] N. Aghanim et al. Planck 2018 results. VI. Cosmological parameters. 2018.

[52] J Anthony Tyson, Greg P Kochanski, and Ian P Dell'Antonio. Detailed mass map of cl 0024+ 1654 from strong lensing. *The Astrophysical Journal Letters*, 498(2):L107, 1998.

[53] Alexandre Refregier. Weak gravitational lensing by large-scale structure. *Annual Review of Astronomy and Astrophysics*, 41(1):645–668, 2003.

[54] Maxim Markevitch et al. Direct constraints on the dark matter self-interaction cross-section from the merging galaxy cluster 1E0657-56. *Astrophys. J.*, 606:819–824, 2004.

[55] Craig J Copi, David N Schramm, and Michael S Turner. Big-bang nucleosynthesis and the baryon density of the universe. *Science*, 267(5195):192–199, 1995.

[56] Anne Green. Dark matter in astrophysics/cosmology. *SciPost Physics Lecture Notes*, page 037, 2022.

[57] Riccardo Catena and Piero Ullio. A novel determination of the local dark matter density. *Journal of Cosmology and Astroparticle Physics*, 2010(08):004, 2010.

[58] N Wyn Evans, Ciaran AJ O'Hare, and Christopher McCabe. Refinement of the standard halo model for dark matter searches in light of the gaia sausage. *Physical Review D*, 99(2):023012, 2019.

[59] Alaina Attanasio, Sunil A Bhave, Carlos Blanco, Daniel Carney, Marcel Demarteau, Bahaa Elshimy, Michael Febbraro, Matthew A Feldman, Sohitri Ghosh, Abby Hickin,

et al. Snowmass 2021 white paper: The windchime project. *arXiv preprint arXiv:2203.07242*, 2022.

[60] Marco Battaglieri, Alberto Belloni, Aaron Chou, Priscilla Cushman, Bertrand Echenard, Rouven Essig, Juan Estrada, Jonathan L Feng, Brenna Flaugher, Patrick J Fox, et al. Us cosmic visions: new ideas in dark matter 2017: community report. *arXiv preprint arXiv:1707.04591*, 2017.

[61] XENON Collaboration, E Aprile, J Aalbers, F Agostini, M Alfonsi, L Althueser, FD Amaro, M Anthony, F Arneodo, L Baudis, et al. Dark matter search results from a one ton-year exposure of xenon1t. *Physical review letters*, 121(11):111302, 2018.

[62] Z Ahmed, DS Akerib, S Arrenberg, MJ Attisha, CN Bailey, L Baudis, DA Bauer, J Beaty, PL Brink, T Bruch, et al. Search for weakly interacting massive particles with the first five-tower data from the cryogenic dark matter search at the soudan underground laboratory. *Physical Review Letters*, 102(1):011301, 2009.

[63] Francesca Chadha-Day, John Ellis, and David JE Marsh. Axion dark matter: What is it and why now? *Science advances*, 8(8):eabj3618, 2022.

[64] D. F. Jackson Kimball and K. van Bibber, editors. *The Search for Ultralight Bosonic Dark Matter*. Springer, New York, 2021.

[65] Gary P Centers, John W Blanchard, Jan Conrad, Nataniel L Figueroa, Antoine Garcon, Alexander V Gramolin, Derek F Jackson Kimball, Matthew Lawson, Bart Pelssers, Joseph A Smiga, et al. Stochastic fluctuations of bosonic dark matter. *Nature communications*, 12(1):1–6, 2021.

[66] Daniel Carney, Anson Hook, Zhen Liu, Jacob M Taylor, and Yue Zhao. Ultralight dark matter detection with mechanical quantum sensors. *New Journal of Physics*, 23(2):023041, 2021.

[67] YV Stadnik and VV Flambaum. Searching for dark matter and variation of fundamental constants with laser and maser interferometry. *Physical review letters*, 114(16):161301, 2015.

[68] Asimina Arvanitaki, Masha Baryakhtar, and Xinlu Huang. Discovering the qcd axion with black holes and gravitational waves. *Physical Review D*, 91(8):084011, 2015.

[69] Peter W Graham, David E Kaplan, Jeremy Mardon, Surjeet Rajendran, William A Terrano, Lutz Trahms, and Thomas Wilkason. Spin precession experiments for light axionic dark matter. *Physical Review D*, 97(5):055006, 2018.

[70] Masha Baryakhtar, Junwu Huang, and Robert Lasenby. Axion and hidden photon dark matter detection with multilayer optical haloscopes. *Physical Review D*, 98(3):035006, 2018.

[71] C Braxmaier, O Pradl, H Müller, A Peters, J Mlynek, V Loriette, and S Schiller. Proposed test of the time independence of the fundamental constants α and m e/m p using monolithic resonators. *Physical Review D*, 64(4):042001, 2001.

[72] Peter W Graham, David E Kaplan, Jeremy Mardon, Surjeet Rajendran, and William A Terrano. Dark matter direct detection with accelerometers. *Physical Review D*, 93(7):075029, 2016.

[73] Denis V Martynov, ED Hall, BP Abbott, R Abbott, TD Abbott, C Adams, RX Adhikari, RA Anderson, SB Anderson, K Arai, et al. Sensitivity of the advanced ligo detectors at the beginning of gravitational wave astronomy. *Physical Review D*, 93(11):112004, 2016.

[74] Fernando Monteiro, Wenqiang Li, Gadi Afek, Chang-ling Li, Michael Mossman, and David C Moore. Force and acceleration sensing with optically levitated nanogram masses at microkelvin temperatures. *Physical Review A*, 101(5):053835, 2020.

[75] Markus Aspelmeyer, Tobias J Kippenberg, and Florian Marquardt. Cavity optomechanics. *Rev. Mod. Phys.*, 86(4):1391, 2014.

[76] Georg Anetsberger, Olivier Arcizet, E Gavartin, QP Unterreithmeier, EM Weig, ML Gorodetsky, JP Kotthaus, and TJ Kippenberg. Optical measurement of nanomechanical motion with an imprecision at the standard quantum limit. In *Quantum Electronics and Laser Science Conference*, page JMA3. Optical Society of America, 2010.

[77] M e Tse, Haocun Yu, Nutsinee Kijbunchoo, A Fernandez-Galiana, P Dupej, L Barsotti, CD Blair, DD Brown, SE Dwyer, A Effler, et al. Quantum-enhanced advanced ligo detectors in the era of gravitational-wave astronomy. *Physical Review Letters*, 123(23):231107, 2019.

[78] Georg Anetsberger, Emanuel Gavartin, Olivier Arcizet, Quirin P Unterreithmeier, Eva Maria Weig, Michael L Gorodetsky, Jörg Peter Kotthaus, and Tobias J Kippenberg. Measuring nanomechanical motion with an imprecision below the standard quantum limit. *Physical Review A*, 82(6):061804, 2010.

[79] Felipe Guzmán Cervantes, Lee Kumanchik, Jon Pratt, and Jacob M Taylor. High sensitivity optomechanical reference accelerometer over 10 khz. *App. Phys. Lett.*, 104(22):221111, 2014.

[80] Alexander G Krause, Martin Winger, Tim D Blasius, Qiang Lin, and Oskar Painter. A high-resolution microchip optomechanical accelerometer. *Nat. Phot.*, 6(11):768, 2012.

[81] Andrea Vinante, Michele Bonaldi, F Marin, and JP Zendri. Dissipative feedback does not improve the optimal resolution of incoherent force detection. *Nature Nanotechnology*, 8(7):470–470, 2013.

[82] B. M. Abraham et al. Sound Propagation in Liquid He-4. *Phys. Rev.*, 181:347–373, 1969.

[83] V Vadakkumbatt, M Hirschel, J Manley, TJ Clark, S Singh, and JP Davis. Prototype superfluid gravitational wave detector. *Physical Review D*, 104(8):082001, 2021.

[84] Raphael St-Gelais, Simon Bernard, Christoph Reinhardt, and Jack C Sankey. Swept-frequency drumhead optomechanical resonators. *ACS Phot.*, 6(2):525–530, 2019.

[85] NE Flowers-Jacobs, SW Hoch, JC Sankey, A Kashkanova, AM Jayich, C Deutsch, J Reichel, and JGE Harris. Fiber-cavity-based optomechanical device. *App. Phys. Lett.*, 101(22):221109, 2012.

[86] Paola Arias, Davide Cadamuro, Mark Goodsell, Joerg Jaeckel, Javier Redondo, and Andreas Ringwald. Wispy cold dark matter. *Journal of Cosmology and Astroparticle Physics*, 2012(06):013, 2012.

[87] Henri Ruegg and Marti Ruiz-Altaba. The stueckelberg field. *International Journal of Modern Physics A*, 19(20):3265–3347, 2004.

[88] Ann E. Nelson and Jakub Scholtz. Dark Light, Dark Matter and the Misalignment Mechanism. *Phys. Rev. D.*, 84:103501, 2011.

[89] Peter W. Graham, Jeremy Mardon, and Surjeet Rajendran. Vector Dark Matter from Inflationary Fluctuations. *Phys. Rev. D*, 93(10):103520, 2016.

[90] J.A.R. Cembranos, A.L. Maroto, and S. J. Núñez Jareño. Perturbations of ultralight vector field dark matter. *JHEP*, 02:064, 2017.

[91] Jeff A Dror, Keisuke Harigaya, and Vijay Narayan. Parametric resonance production of ultralight vector dark matter. *Physical Review D*, 99(3):035036, 2019.

[92] Raymond T. Co, Aaron Pierce, Zhengkang Zhang, and Yue Zhao. Dark Photon Dark Matter Produced by Axion Oscillations. *Phys. Rev. D*, 99(7):075002, 2019.

[93] Mar Bastero-Gil, Jose Santiago, Lorenzo Ubaldi, and Roberto Vega-Morales. Vector dark matter production at the end of inflation. *JCAP*, 04:015, 2019.

[94] Prateek Agrawal, Naoya Kitajima, Matthew Reece, Toyokazu Sekiguchi, and Fuminobu Takahashi. Relic Abundance of Dark Photon Dark Matter. *Phys. Lett. B.*, 801:135136, 2020.

[95] Kazunori Nakayama. Vector Coherent Oscillation Dark Matter. *JCAP*, 10:019, 2019.

[96] Kimihiro Nomura, Asuka Ito, and Jiro Soda. Pulsar timing residual induced by ultralight vector dark matter. *Eur. Phys. J.*, C80(5):419, 2020.

[97] Davide Cadamuro. Cosmological limits on axions and axion-like particles. *arXiv preprint arXiv:1210.3196*, 2012.

[98] David J. E. Marsh. Axion Cosmology. *Phys. Rept.*, 643:1–79, 2016.

[99] Thibault Damour and John F Donoghue. Equivalence principle violations and couplings of a light dilaton. *Physical Review D*, 82(8):084033, 2010.

[100] David Griffiths. *Introduction to elementary particles*. John Wiley & Sons, 2008.

[101] Thibault Damour and Alexander M Polyakov. The string dilation and a least coupling principle. *Nuclear Physics B*, 423(2-3):532–558, 1994.

[102] Lukáš F Pašteka, Yongliang Hao, Anastasia Borschevsky, Victor V Flambaum, and Peter Schwerdtfeger. Material size dependence on fundamental constants. *Physical review letters*, 122(16):160801, 2019.

[103] Aashish A Clerk, Michel H Devoret, Steven M Girvin, Florian Marquardt, and Robert J Schoelkopf. Introduction to quantum noise, measurement, and amplification. *Reviews of Modern Physics*, 82(2):1155, 2010.

[104] Dmitry Budker, Peter W Graham, Micah Ledbetter, Surjeet Rajendran, and Alexander O Sushkov. Proposal for a cosmic axion spin precession experiment (casper). *Phys. Rev. X*, 4(2):021030, 2014.

[105] Aaron Pierce, Keith Riles, and Yue Zhao. Searching for dark photon dark matter with gravitational-wave detectors. *Phys. Rev. Lett.*, 121(6):061102, 2018.

[106] Andrew A Geraci and Andrei Derevianko. Sensitivity of atom interferometry to ultralight scalar field dark matter. *Phys. Rev. Lett.*, 117(26):261301, 2016.

[107] Lee D Feinberg, Mark Clampin, Ritva Keski-Kuha, Charlie Atkinson, Scott Texter, Mark Bergeland, and Benjamin B Gallagher. James webb space telescope optical telescope element mirror development history and results. In *Space Telescopes and Instrumentation 2012: Optical, Infrared, and Millimeter Wave*, volume 8442, pages 822–831. SPIE, 2012.

[108] Fernando Monteiro, Sumita Ghosh, Adam Getzels Fine, and David C Moore. Optical levitation of 10-ng spheres with nano-g acceleration sensitivity. *Phys. Rev. A*, 96(6):063841, 2017.

[109] Ying Lia Li and PF Barker. Characterization and testing of a micro-g whispering gallery mode optomechanical accelerometer. *J. Light. Technol.*, 36(18):3919–3926, 2018.

[110] Yeghishe Tsaturyan, Andreas Barg, Eugene S Polzik, and Albert Schliesser. Ultracoherent nanomechanical resonators via soft clamping and dissipation dilution. *Nat. Nano.*, 12(8):776, 2017.

[111] Amir H Ghadimi, Sergey A Fedorov, Nils J Engelsen, Mohammad J Bereyhi, Ryan Schilling, Dalziel J Wilson, and Tobias J Kippenberg. Elastic strain engineering for ultralow mechanical dissipation. *Science*, 360(6390):764–768, 2018.

[112] Pedram Sadeghi, Manuel Tanzer, Niklas Luhmann, Markus Piller, Miao-Hsuan Chien, and Silvan Schmid. Thermal transport and frequency response of localized modes on low-stress nanomechanical silicon nitride drums featuring a phononic bandgap structure. *arXiv preprint arXiv:2005.10860*, 2020.

[113] Sepideh Naserbakht, Andreas Naesby, and Aurélien Dantan. Stress-controlled frequency tuning and parametric amplification of the vibrations of coupled nanomembranes. *App. Sci.*, 9(22):4845, 2019.

[114] João P Moura, Richard A Norte, Jingkun Guo, Clemens Schäfermeier, and Simon Gröblacher. Centimeter-scale suspended photonic crystal mirrors. *Opt. Exp.*, 26(2):1895–1909, 2018.

[115] Xu Chen, Clément Chardin, Kevin Makles, Charles Caër, Sheon Chua, Rémy Braive, Isabelle Robert-Philip, Tristan Briant, Pierre-François Cohadon, Antoine Heidmann, et al. High-finesse fabry–perot cavities with bidimensional si 3 n 4 photonic-crystal slabs. *Light Sci. Appl.*, 6(1):e16190–e16190, 2017.

[116] Hiromasa Hirakawa, Kazumichi Narihara, and Masa-Katsu Fujimoto. Theory of antennas for gravitational radiation. *Journal of the Physical Society of Japan*, 41(4):1093–1101, 1976.

[117] Dalziel J Wilson, Jack Manley, Mitul Dey Chowdhury, Swati Singh, and Daniel Grin. Searching for dark matter with an optomechanical accelerometer. In *Optical and Quantum Sensing and Precision Metrology II*, page PC120160N. SPIE, 2022.

[118] Christoph Reinhardt, Tina Müller, Alexandre Bourassa, and Jack C Sankey. Ultralow-noise sin trampoline resonators for sensing and optomechanics. *Physical Review X*, 6(2):021001, 2016.

[119] Jingkun Guo, Richard A Norte, and Simon Gröblacher. Integrated optical force sensors using focusing photonic crystal arrays. *Optics Express*, 25(8):9196–9203, 2017.

[120] Joseph Weber. Detection and generation of gravitational waves. *Physical Review*, 117(1):306, 1960.

[121] Hiromasa Hirakawa. Dispersion of gravitational waves. *J. Phys. Soc. Jpn.*, 35(1):295–297, 1973.

[122] L. A. DeLorenzo and K. C. Schwab. Ultra-high Q Acoustic Resonance in Superfluid 4He. *Journal of Low Temperature Physics*, 186:233–240, Feb 2017.

[123] S. Singh, L. A. De Lorenzo, I. Pikovski, and K. C. Schwab. Detecting continuous gravitational waves with superfluid ^{4}He. *New J. Phys.*, 19(7):073023, 2017.

[124] KH S Bagdasar, V B Braginsky, and V P Mitrofanov. Absorption of longitudinal acoustic waves in single crystals of ruby and sapphire. *Sov. Phys. Crystallogr.*, 19(4):549, 1975.

[125] Vladimir Borisovich Braginsky, VP Mitrofanov, and Vladimir Ivanovich Panov. *Systems with small dissipation*. University of Chicago Press, 1985.

[126] Leonhard Neuhaus. *Cooling a macroscopic mechanical oscillator close to its quantum ground state*. PhD thesis, Université Pierre et Marie Curie - Paris VI, 2016.

[127] Leonhard Neuhaus et al. Cooling a macroscopic mechanical oscillator close to its quantum ground state. In *Quantum Information and Measurement*, pages QF2C–3. Optical Society of America, 2017.

[128] Lev Davidovich Landau, Evgenij M Lifšic, Evegnii Mikhailovich Lifshitz, Arnold Markovich Kosevich, and Lev Petrovich Pitaevskii. *Theory of elasticity: volume 7*, volume 7. Elsevier, 1986.

[129] Peter R Saulson. Thermal noise in mechanical experiments. *Phys. Rev. D*, 42(8):2437, 1990.

[130] Garrett D Cole, Wei Zhang, Michael J Martin, Jun Ye, and Markus Aspelmeyer. Tenfold reduction of brownian noise in high-reflectivity optical coatings. *Nature Photonics*, 7(8):644, 2013.

[131] Maxim Goryachev, Eugene N Ivanov, Frank Van Kann, Serge Galliou, and Michael E Tobar. Observation of the fundamental nyquist noise limit in an ultra-high q-factor cryogenic bulk acoustic wave cavity. *Applied Physics Letters*, 105(15):153505, 2014.

[132] Alexander Khalaidovski et al. Evaluation of heat extraction through sapphire fibers for the GW observatory KAGRA. *Class. Quant. Grav.*, 31:105004, 2014.

[133] COMSOL, Inc. COMSOL Multiphysics® v. 5.4. www.comsol.com, 2019.

[134] Marvin Hirschel, Vaisakh Vadakkumbatt, Jack Manley, Swati Singh, and John Davis. Listening to the sound of dark matter with superfluid helium. *Bulletin of the American Physical Society*, 2022.

[135] Hartmut Grote and YV Stadnik. Novel signatures of dark matter in laser-interferometric gravitational-wave detectors. *Physical Review Research*, 1(3):033187, 2019.

[136] Thomas D Bradley, Gregory T Jasion, John R Hayes, Yong Chen, Lucy Hooper, Hesham Sakr, Marcelo Alonso, Austin Taranta, Arsalan Saljoghei, Hans Christian Mulvad, et al. Antiresonant hollow core fibre with 0.65 db/km attenuation across the c and l telecommunication bands. In *45th European Conference on Optical Communication (ECOC 2019)*, pages 1–4. IET, 2019.

[137] Gregory T Jasion, Thomas D Bradley, Kerrianne Harrington, Hesham Sakr, Yong Chen, Eric Numkam Fokoua, Ian A Davidson, Austin Taranta, John R Hayes, David J Richardson, et al. Recent breakthroughs in hollow core fiber technology. In *Optical Fiber Communication Conference*, pages M5E–2. Optical Society of America, 2021.

[138] Bo Shi, Hesham Sakr, John Hayes, Xuhao Wei, Eric Numkam Fokoua, Meng Ding, Zitong Feng, Giuseppe Marra, Francesco Poletti, David J Richardson, et al. Thinly coated hollow core fiber for improved thermal phase-stability performance. *Optics Letters*, 46(20):5177–5180, 2021.

[139] Lingze Duan. General treatment of the thermal noises in optical fibers. *Physical Review A*, 86(2):023817, 2012.

[140] LZ Duan. Intrinsic thermal noise of optical fibres due to mechanical dissipation. *Electronics letters*, 46(22):1515–1516, 2010.

[141] Robert E Bartolo, Alan B Tveten, and Anthony Dandridge. Thermal phase noise measurements in optical fiber interferometers. *IEEE Journal of Quantum Electronics*, 48(5):720–727, 2012.

[142] Jing Dong, Junchao Huang, Tang Li, and Liang Liu. Observation of fundamental thermal noise in optical fibers down to infrasonic frequencies. *Applied Physics Letters*, 108(2):021108, 2016.

[143] Junchao Huang, Lingke Wang, Yifei Duan, Yafeng Huang, Meifeng Ye, Liang Liu, and Tang Li. All-fiber-based laser with 200 mhz linewidth. *Chinese Optics Letters*, 17(7):071407, 2019.

[144] Charles Kittel. Temperature fluctuation: an oxymoron. *Phys. Today*, 41(5):93, 1988.

[145] William H Glenn. Noise in interferometric optical systems: An optical nyquist theorem. *IEEE journal of quantum electronics*, 25(6):1218–1224, 1989.

[146] KH Wanser. Fundamental phase noise limit in optical fibres due to temperature fluctuations. *Electronics letters*, 28(1):53–54, 1992.

[147] Lifei Wu, Yanyi Jiang, Chaoqun Ma, Wen Qi, Hongfu Yu, Zhiyi Bi, and Longsheng Ma. 0.26-hz-linewidth ultrastable lasers at 1557 nm. *Scientific Reports*, 6(1):1–5, 2016.

[148] Jing Dong, Yongqi Hu, Junchao Huang, Meifeng Ye, Qiuzhi Qu, Tang Li, and Liang Liu. Subhertz linewidth laser by locking to a fiber delay line. *Applied optics*, 54(5):1152–1156, 2015.

[149] Jon R Peterson. Observations and modeling of seismic background noise. Technical report, US Geological Survey, 1993.

[150] DB Newell, SJ Richman, PG Nelson, RT Stebbins, PL Bender, JE Faller, and J Mason. An ultra-low-noise, low-frequency, six degrees of freedom active vibration isolator. *Review of scientific instruments*, 68(8):3211–3219, 1997.

[151] T Li, B Argence, A Haboucha, H Jiang, JL Dornaux, D Koné, A Clairon, P Lemonde, G Santarelli, C Nelson, et al. Low vibration sensitivity fiber spools for laser stabilization. In *2011 Joint Conference of the IEEE International Frequency Control and the European Frequency and Time Forum (FCS) Proceedings*, pages 1–3. IEEE, 2011.

[152] Junchao Huang, Lingke Wang, Yifei Duan, Yafeng Huang, Meifeng Ye, Lin Li, Liang Liu, and Tang Li. Vibration-insensitive fiber spool for laser stabilization. *Chinese Optics Letters*, 17(8):081403, 2019.

[153] Michael J Thorpe, David R Leibrandt, Tara M Fortier, and Till Rosenband. Measurement and real-time cancellation of vibration-induced phase noise in a cavity-stabilized laser. *Optics Express*, 18(18):18744–18751, 2010.

[154] David R Leibrandt, James C Bergquist, and Till Rosenband. Cavity-stabilized laser with acceleration sensitivity below 10- 12 g- 1. *Physical Review A*, 87(2):023829, 2013.

[155] Gregory T Jasion, Hesham Sakr, John R Hayes, Seyed Reza Sandoghchi, Lucy Hooper, Eric Numkam Fokoua, Arsalan Saljoghei, Hans Christian Mulvad, Marcelo Alonso, Austin Taranta, et al. 0.174 db/km hollow core double nested antiresonant nodeless fiber (dnanf). In *2022 Optical Fiber Communications Conference and Exhibition (OFC)*, pages 1–3. IEEE, 2022.

[156] H Zu, W Dai, and ATAM de Waele. Development of dilution refrigerators—a review. *Cryogenics*, 121:103390, 2022.

[157] Abhishek Banerjee, Dmitry Budker, Joshua Eby, Hyungjin Kim, and Gilad Perez. Relaxion stars and their detection via atomic physics. *Communications Physics*, 3(1):1–8, 2020.

[158] Abhishek Banerjee, Dmitry Budker, Joshua Eby, Victor V Flambaum, Hyungjin Kim, Oleksii Matsedonskyi, and Gilad Perez. Searching for earth/solar axion halos. *Journal of High Energy Physics*, 2020(9):1–26, 2020.

[159] Jeffrey D Scargle. Studies in astronomical time series analysis. ii-statistical aspects of spectral analysis of unevenly spaced data. *The Astrophysical Journal*, 263:835–853, 1982.

[160] Andrew Matas and Joseph D Romano. Frequentist versus bayesian analyses: Cross-correlation as an approximate sufficient statistic for ligo-virgo stochastic background searches. *Physical Review D*, 103(6):062003, 2021.

[161] Ariel Arza, Michael A Fedderke, Peter W Graham, Derek F Jackson Kimball, and Saarik Kalia. Earth as a transducer for axion dark-matter detection. *Physical Review D*, 105(9):095007, 2022.

[162] Chelsea Bartram, Thomas Braine, Raphael Cervantes, N Crisosto, N Du, Grant Leum, LJ Rosenberg, Gray Rybka, Jihui Yang, D Bowring, et al. Axion dark matter experiment: Run 1b analysis details. *Physical Review D*, 103(3):032002, 2021.

[163] Daniel Carney, Gordan Krnjaic, David C Moore, Cindy A Regal, Gadi Afek, Sunil Bhave, Benjamin Brubaker, Thomas Corbitt, Jonathan Cripe, Nicole Crisosto, et al. Mechanical quantum sensing in the search for dark matter. *Quantum Science and Technology*, 6(2):024002, 2021.

[164] Anthony J Brady, Christina Gao, Roni Harnik, Zhen Liu, Zheshen Zhang, and Quntao Zhuang. Entangled sensor-networks for dark-matter searches. *arXiv preprint arXiv:2203.05375*, 2022.

[165] Bernard Schutz. *A first course in general relativity*. Cambridge university press, 2009.

[166] Walter Greiner. *Relativistic quantum mechanics*, volume 2. Springer, 2000.

[167] Michael Peskin and Daniel Schroeder. *An introduction to quantum field theory*. Perseus Books Publishing, LLC, 1995.

[168] Eugen Merzbacher. *Quantum Mechanics*. John Wiley & Sons, 1998.

[169] Matthew D Schwartz. *Quantum field theory and the standard model*. Cambridge University Press, 2014.

[170] Mark Srednicki. *Quantum field theory*. Cambridge University Press, 2007.

[171] David J Griffiths and Darrell F Schroeter. *Introduction to quantum mechanics*. Cambridge University Press, 2018.

[172] Andrew Zangwill. *Modern electrodynamics*. Cambridge University Press, 2013.

[173] Wolfgang KH Panofsky and Melba Phillips. *Classical electricity and magnetism*. Courier Corporation, 2005.

[174] David J Griffiths. Introduction to electrodynamics, 2005.

[175] Ian H Malitson. Interspecimen comparison of the refractive index of fused silica. *Josa*, 55(10):1205–1209, 1965.

[176] Charles D Butter and GB Hocker. Fiber optics strain gauge. *Applied optics*, 17(18):2867–2869, 1978.

[177] Brad M Beadle and Jacek Jarzynski. Measurement of speed and attenuation of longitudinal elastic waves in optical fibers. *Optical engineering*, 40(10):2115–2119, 2001.

[178] Anja Schroeter, Ronny Nawrodt, Roman Schnabel, Stuart Reid, Iain Martin, Sheila Rowan, Christian Schwarz, Torsten Koettig, Ralf Neubert, Matthias Thürk, et al. On the mechanical quality factors of cryogenic test masses from fused silica and crystalline quartz. *arXiv preprint arXiv:0709.4359*, 2007.

[179] Andri M Gretarsson and Gregory M Harry. Dissipation of mechanical energy in fused silica fibers. *Review of scientific instruments*, 70(10):4081–4087, 1999.

[180] Steven D Penn, Gregory M Harry, Andri M Gretarsson, Scott E Kittelberger, Peter R Saulson, John J Schiller, Joshua R Smith, and Sol O Swords. High quality factor measured in fused silica. *Review of Scientific Instruments*, 72(9):3670–3673, 2001.

[181] Alastair Heptonstall, Mark Barton, Caroline Cantley, Alan Cumming, Geppo Cagnoli, James Hough, Russell Jones, Rahul Kumar, Iain Martin, Sheila Rowan, et al. Investigation of mechanical dissipation in co2 laser-drawn fused silica fibres and welds. *Classical and Quantum Gravity*, 27(3):035013, 2010.

[182] HJ McSkimin. Measurement of elastic constants at low temperatures by means of ultrasonic waves–data for silicon and germanium single crystals, and for fused silica. *Journal of applied physics*, 24(8):988–997, 1953.

[183] Max B Reid and Meric Ozcan. Temperature dependence of fiber optic bragg gratings at low temperatures. *Optical Engineering*, 37(1):237–240, 1998.

[184] Olivier Arcizet, Rémi Rivière, Albert Schliesser, Georg Anetsberger, and Tobias J Kippenberg. Cryogenic properties of optomechanical silica microcavities. *Physical Review A*, 80(2):021803, 2009.

[185] RO Behunin, P Kharel, WH Renninger, and PT Rakich. Engineering dissipation with phononic spectral hole burning. *Nature Materials*, 16(3):315–321, 2017.

[186] Wenwu Zhu, Eric R Numkam Fokoua, Austin A Taranta, Yong Chen, Thomas Bradley, Marco N Petrovich, Francesco Poletti, Mingshan Zhao, David J Richardson, and Radan Slavík. The thermal phase sensitivity of both coated and uncoated standard and hollow core fibers down to cryogenic temperatures. *Journal of Lightwave Technology*, 38(8):2477–2484, 2019.

Appendix A

LAGRANGIAN FORMALISM

This appendix introduces notation and definitions relevant to the phenomenology of vector and scalar fields. In Section A.2, the formalism is applied to electromagnetism as an example. This appendix may be a helpful reference for the material presented in Sections 2.1 and 2.2.

For a more complete treatment of the subjects presented in this appendix, see

- Ref. [165] regarding vector analysis in four-dimensional spacetime,
- Refs. [166, 167] regarding quantum field theory,
- and Refs. [166, 168] for derivations of the Lorentz force in the single particle approximation.

Variable	Definition	SI Base Units
A^μ	Electromagnetic four-potential	$\mathrm{kg{\cdot}m{\cdot}A^{-1}{\cdot}s^{-2}}$
J^μ	four-current density	$\mathrm{A{\cdot}m^{-2}}$
$F^{\mu\nu}$	Faraday Tensor	$\mathrm{kg{\cdot}A^{-1}{\cdot}s^{-2}}$
ψ	fermion field (adjoint $\bar{\psi}$)	$\mathrm{m^{-3/2}}$
$\mathcal{L}$	Lagrangian Density	$\mathrm{kg{\cdot}m^{-1}{\cdot}s^{-2}}$
m_ψ	mass of fermion	kg
q_ψ	electric charge of fermion	$\mathrm{A{\cdot}s}$
ρ_ψ	electric charge density of fermion field	$\mathrm{A{\cdot}s{\cdot}m^{-3}}$
γ^μ	Gamma matrices	-
σ^i	Pauli matrices	-
$\eta^{\mu\nu}$	Minkowski metric	-
$\hat{\mathbf{\Pi}}$	kinetic momentum	$\mathrm{kg{\cdot}m{\cdot}s^{-1}}$
$\boldsymbol{e_i}$	basis vector	-

Table A.1: Some relevant variable definitions for this appendix.

A.1 Four-vector analysis conventions

The metric signature $\begin{pmatrix} + & - & - & - \end{pmatrix}$ will be used. The sign conventions for components of four-vectors and four-derivatives are stated explicitly in Table A.2.

Four-vector/derivative	Components
∂^μ	$\left(\partial^0, \partial^1, \partial^2, \partial^3\right) = \left(\frac{1}{c}\frac{\partial}{\partial t}, -\frac{\partial}{\partial x}, -\frac{\partial}{\partial y}, -\frac{\partial}{\partial z}\right)$
∂_μ	$(\partial_0, \partial_1, \partial_2, \partial_3) = \left(\frac{1}{c}\frac{\partial}{\partial t}, \frac{\partial}{\partial x}, \frac{\partial}{\partial y}, \frac{\partial}{\partial z}\right)$
A^μ	$\left(A^0, A^1, A^2, A^3\right) = \left(\frac{V}{c}, \boldsymbol{A}\right)$
A_μ	$(A_0, A_1, A_2, A_3) = \left(\frac{V}{c}, -\boldsymbol{A}\right)$

Table A.2: Sign conventions for four-vectors and four-derivatives (Cartesian).

The index 0 refers to the time component, $r^0 = ct$. The indices $\{1, 2, 3\}$ refer to the spatial components. For example, in Cartesian coordinates, $\left(r^1, r^2, r^3\right) = (x, y, z)$. Bold variables such as $\boldsymbol{r}$ refer to three-component vectors or operators, often representing the spatial components of a four-component vector or operator.

Indices denoted by Roman letters refer purely to spatial dimensions. For example, $i \in \{1, 2, 3\}$. Indices denoted by Greek letters include all four dimensions. For example, $\mu \in \{0, 1, 2, 3\}$.

Shorthand known as the Einstein summation convention [165] is frequently used throughout this dissertation:

$$A_\mu A^\mu \equiv \sum_{\mu=0}^{3} A_\mu A^\mu = A_0 A^0 + A_1 A^1 + A_2 A^2 + A_3 A^3. \tag{A.1}$$

A.1.1 Pauli and gamma matrices

Gamma matrices γ^μ are 4×4 matrices of the form[100]:

$$\gamma^0 = \begin{pmatrix} 1 & 0 \\ 0 & -1 \end{pmatrix} \tag{A.2}$$

$$\gamma^i = \begin{pmatrix} 0 & \sigma^i \\ -\sigma^i & 0 \end{pmatrix} \tag{A.3}$$

where 0 and 1 are the 2×2 zero and identity matrices, and σ^i are the 2×2 Pauli matrices:

$$\sigma^1 = \begin{pmatrix} 0 & 1 \\ 1 & 0 \end{pmatrix}, \quad \sigma^2 = \begin{pmatrix} 0 & -i \\ i & 0 \end{pmatrix}, \quad \sigma^3 = \begin{pmatrix} 1 & 0 \\ 0 & -1 \end{pmatrix}. \tag{A.4}$$

For example, written out completely, γ^2 is

$$\gamma^2 = \begin{pmatrix} 0 & 0 & 0 & -i \\ 0 & 0 & i & 0 \\ 0 & i & 0 & 0 \\ -i & 0 & 0 & 0 \end{pmatrix}. \tag{A.5}$$

A.2 Example: Electromagnetism

Lagrangian densities are used to describe how particles behave and interact. The Lagrangian densities for several hypothetical particles which could compose dark matter are given in the main text. In this section, it is demonstrated how to interpret these expressions and recover the equations of motion needed to understand the DM signal, taking electromagnetism as an example.

The electromagnetic Lagrangian density will be explained and used to derive classical electromagnetism, given by Maxwell's equations and the Lorentz force.

A.2.1 The electromagnetic Lagrangian density

Electromagnetism (EM) describes the behavior of photons and their interaction with charge-carrying fermions.

Photons are massless, spin-1 particles that couple to electric charge. In the classical limit, the photons are described by a relativistic vector field, the electromagnetic four-potential A^μ. Its time component contains the classical scalar electric potential V, and its spatial components compose the classical vector potential $\boldsymbol{A}$:

$$A^\mu(t, \boldsymbol{r}) = \left\{ \frac{V(t, \boldsymbol{r})}{c}, \boldsymbol{A}(t, \boldsymbol{r}) \right\}. \tag{A.6}$$

For brevity, the arguments $(t, \boldsymbol{r})$ are omitted. The spatial and temporal dependence of the fields is implied.

The electromagnetic field tensor, $F^{\mu\nu}$, is defined as

$$F^{\mu\nu} \equiv \partial^{\mu} A^{\nu} - \partial^{\nu} A^{\mu}. \tag{A.7}$$

In Cartesian coordinates:

$$F^{\mu\nu} = \begin{pmatrix} 0 & -\frac{E_x}{c} & -\frac{E_y}{c} & -\frac{E_z}{c} \\ \frac{E_x}{c} & 0 & -B_z & B_y \\ \frac{E_y}{c} & B_z & 0 & -B_x \\ \frac{E_z}{c} & -B_y & B_x & 0 \end{pmatrix}. \tag{A.8}$$

With these definitions, the Lagrangian density of the free EM field is [100]

$$\mathcal{L}_A = -\frac{c^2 \epsilon_0}{4} F_{\mu\nu} F^{\mu\nu}. \tag{A.9}$$

Charge-carrying fermion (such as electrons and protons) fields can be described with the bispinor ψ its adjoint bispinor $\bar{\psi}$:

$$\psi = \begin{pmatrix} \psi_1 \\ \psi_2 \\ \psi_3 \\ \psi_4 \end{pmatrix}, \quad \bar{\psi} \equiv \psi^{\dagger} \gamma^0 = \begin{pmatrix} \psi_1^* & \psi_2^* & -\psi_3^* & -\psi_4^* \end{pmatrix}. \tag{A.10}$$

The four-current density of the charged fermion field is given by [166]

$$J^{\mu} \equiv c q_{\psi} \bar{\psi} \gamma^{\mu} \psi = \left\{ c\rho_{\psi}, \boldsymbol{v}_{\boldsymbol{\psi}} \rho_{\psi} \right\}. \tag{A.11}$$

The Lagrangian density of a free fermion field, with particle mass m_{ψ} and electric charge q_{ψ}, is

$$\mathcal{L}_{\psi} = i\hbar c \bar{\psi} \gamma^{\mu} \partial_{\mu} \psi - m_{\psi} c^2 \bar{\psi} \psi. \tag{A.12}$$

The electromagnetic interaction between the EM field and charged fermions is described with the interaction Lagrangian density

$$\mathcal{L}_{A\psi} = -J^{\mu} A_{\mu}. \tag{A.13}$$

The full EM Lagrangian density, accounting for photons (A.9), fermions (A.12), and their interaction (A.13), is

$$\mathcal{L}_{\mathrm{EM}} = \mathcal{L}_A + \mathcal{L}_\psi + \mathcal{L}_{A\psi} = -\frac{c^2\epsilon_0}{4} F_{\mu\nu}F^{\mu\nu} + i\hbar c\bar{\psi}\gamma^\mu\partial_\mu\psi - m_\psi c^2\bar{\psi}\psi - cq_\psi\bar{\psi}\gamma^\mu\psi A_\mu. \tag{A.14}$$

A.2.2 Maxwell's equations

The equations of motion for the electromagnetic field A^μ can be obtained from the Lagrangian density using the Euler-Lagrange equations [167]:

$$\partial_\mu\left(\frac{\partial\mathcal{L}_{\mathrm{EM}}}{\partial\left(\partial_\mu A_\nu\right)}\right) = \frac{\partial\mathcal{L}_{\mathrm{EM}}}{\partial A_\nu}. \tag{A.15}$$

On the right side of (A.15), we have:[1]

$$\frac{\partial\mathcal{L}_{\mathrm{EM}}}{\partial A_\nu} = -J^\nu. \tag{A.16}$$

As for the left side of (A.15):

$$\begin{aligned}
\partial_\mu\left(\frac{\partial\mathcal{L}_{\mathrm{EM}}}{\partial\left(\partial_\mu A_\nu\right)}\right) &= -\frac{c^2\epsilon_0}{4}\partial_\mu\left(\frac{\partial}{\partial\left(\partial_\mu A_\nu\right)}\right)F_{\alpha\beta}F^{\alpha\beta} \\
&= -\frac{c^2\epsilon_0}{4}\partial_\mu\left(\frac{\partial}{\partial\left(\partial_\mu A_\nu\right)}\right)\left[\left(\partial_\alpha A_\beta - \partial_\beta A_\alpha\right)\left(\partial^\alpha A^\beta - \partial^\beta A^\alpha\right)\right] \\
&= -\frac{c^2\epsilon_0}{2}\partial_\mu\left(\frac{\partial}{\partial\left(\partial_\mu A_\nu\right)}\right)\left[\partial^\alpha A^\beta\left(\partial_\alpha A_\beta - \partial_\beta A_\alpha\right)\right] \\
&= -\frac{c^2\epsilon_0}{2}\partial_\mu\left[\frac{\partial\left(\partial^\alpha A^\beta\right)}{\partial\left(\partial_\mu A_\nu\right)}\left(\partial_\alpha A_\beta - \partial_\beta A_\alpha\right) + \partial^\alpha A^\beta\left(\frac{\partial\left(\partial_\alpha A_\beta\right)}{\partial\left(\partial_\mu A_\nu\right)} - \frac{\partial\left(\partial_\beta A_\alpha\right)}{\partial\left(\partial_\mu A_\nu\right)}\right)\right] \\
&= -\frac{c^2\epsilon_0}{2}\partial_\mu\left[\eta^{\mu\alpha}\eta^{\nu\beta}\left(\partial_\alpha A_\beta - \partial_\beta A_\alpha\right) + \partial^\alpha A^\beta\left(\eta^\mu_\alpha\eta^\nu_\beta - \eta^\mu_\beta\eta^\nu_\alpha\right)\right] \\
&= -c^2\epsilon_0\partial_\mu\left(\partial^\mu A^\nu - \partial^\nu A^\mu\right)
\end{aligned}$$

[1] Note that $\frac{\partial}{\partial A_\nu}F_{\alpha\beta} = \partial_\alpha\frac{\partial A_\beta}{\partial A_\nu} - \partial_\beta\frac{\partial A_\alpha}{\partial A_\nu} = \partial_\alpha\eta^\nu_\beta - \partial_\beta\eta^\nu_\alpha = 0$, since η^ν_β is a constant. Similar algebra yields $\frac{\partial}{\partial A_\nu}F^{\alpha\beta} = 0$. So $\frac{\partial\mathcal{L}_A}{\partial A_\nu} = 0$ for all ν.

So the result of (A.15) is

$$\partial_\mu \left(\partial^\mu A^\nu - \partial^\nu A^\mu\right) = \frac{J^\nu}{c^2 \epsilon_0}, \tag{A.17}$$

which is the Proca equation for a massless vector field coupled to a fermion current density.

Choosing to define the electric and magnetic fields in terms of the four-potential as

$$\boldsymbol{B} = \nabla \times \boldsymbol{A} \tag{A.18a}$$

$$\boldsymbol{E} = -\nabla V - \frac{\partial \boldsymbol{A}}{\partial t}, \tag{A.18b}$$

(A.17) can be found to yield Maxwell's equations:

$$\nabla \cdot \boldsymbol{E} = \frac{\rho_\psi}{\epsilon_0} \tag{A.19a}$$

$$\nabla \cdot \boldsymbol{B} = 0 \tag{A.19b}$$

$$\nabla \times \boldsymbol{E} = -\frac{\partial \boldsymbol{B}}{\partial t} \tag{A.19c}$$

$$c^2 \nabla \times \boldsymbol{B} = \frac{\boldsymbol{J}}{\epsilon_0} + \frac{\partial \boldsymbol{E}}{\partial t} \tag{A.19d}$$

A.2.3 Energy density of the electromagnetic field

The canonical stress-energy tensor for a vector field is [169]

$$T^{\mu\nu} = \partial^\nu A_\alpha \frac{\partial \mathcal{L}_A}{\partial \left(\partial_\mu A_\alpha\right)} - \eta^{\mu\nu} \mathcal{L}_A. \tag{A.20}$$

$T^{\mu\nu}$ can be symmetrized by adding an additional term [167]:

$$\bar{T}^{\mu\nu} = T^{\mu\nu} + \frac{1}{\mu_0} \partial_\alpha A^\nu F^{\mu\alpha} = c^2 \epsilon_0 \left(-F^{\mu\alpha} F^\nu{}_\alpha + \frac{1}{4} \eta^{\mu\nu} F_{\alpha\beta} F^{\alpha\beta}\right). \tag{A.21}$$

In general relativity, the symmetric tensor $\bar{T}^{\mu\nu}$ is what couples to gravity [170], which will be important in Appendix 2.1.3 where the field amplitude is related to the energy density for vector dark matter.

The 00-component of the symmetric stress-energy tensor $\bar{T}^{\mu\nu}$ is the energy density of the electromagnetic field, which can be shown to be

$$\bar{T}^{00} = \frac{1}{2} \left(\epsilon_0 E^2 + \frac{1}{\mu_0} B^2\right). \tag{A.22}$$

A.2.4 Lorentz force

In classical electrodynamics, photons are treated as a field, while fermions can be treated as individual particles. The classical fermion is localized in space and has its own equation of motion. In this section, the fermion field will be considered in the single particle approximation, where ψ's components are considered wavefunctions instead of operators [168], in order to recover the classical EM force on a charge-carrying particle.

Considering just the ψ-terms ($\mathcal{L}_\psi$ and $\mathcal{L}_{A\psi}$), the Hamiltonian density of the fermion field is [166]

$$\begin{aligned}\mathcal{H} &= \frac{\partial \mathcal{L}}{\partial \dot{\psi}}\dot{\psi} - \mathcal{L} \\ &= i\hbar c\bar{\psi}\gamma^0\partial_0\psi - \left(i\hbar c\bar{\psi}\gamma^\mu\partial_\mu\psi - m_\psi c^2\bar{\psi}\psi - cq_\psi\bar{\psi}\gamma^\mu\psi A_\mu\right) \\ &= -i\hbar c\bar{\psi}\gamma^i\partial_i\psi + m_\psi c^2\bar{\psi}\psi + cq_\psi\bar{\psi}\gamma^\mu\psi A_\mu \\ &= \psi^\dagger\left[c\gamma^0\boldsymbol{\gamma}\cdot\left(\hat{\boldsymbol{p}} - q_\psi\boldsymbol{A}\right) + q_\psi V + \gamma^0 m_\psi c^2\right]\psi \equiv \psi^\dagger\hat{H}\psi\end{aligned}$$

where $\hat{\boldsymbol{p}} = -i\hbar\nabla$ is the momentum operator from non-relativistic quantum mechanics[171] and

$$\hat{H} = c\gamma^0\boldsymbol{\gamma}\cdot\left(\hat{\boldsymbol{p}} - q_\psi\boldsymbol{A}\right) + q_\psi V + \gamma^0 m_\psi c^2 \tag{A.23}$$

is simply the one particle Hamiltonian operator [168].

The Hamiltonian can be used to find the time-derivative of the position operator through the Heisenberg equation of motion:

$$\begin{aligned}\frac{d\hat{\boldsymbol{r}}}{dt} &= \frac{i}{\hbar}\left[\hat{H}, \hat{\boldsymbol{r}}\right] \\ &= \frac{ic}{\hbar}\left[\gamma^0\boldsymbol{\gamma}\cdot\hat{\boldsymbol{p}}, \hat{\boldsymbol{r}}\right] \\ &= c\gamma^0\left[\gamma^i\partial_i, \hat{\boldsymbol{r}}\right],\end{aligned}$$

using the fact that the position operator $\hat{\boldsymbol{r}}$ commutes with γ^μ, $\boldsymbol{A}$, and V.

The velocity operator is defined as[2] [168]

$$\hat{\boldsymbol{v}} \equiv \frac{d\hat{\boldsymbol{r}}}{dt} = c\gamma^0\boldsymbol{\gamma}. \tag{A.24}$$

The momentum of a particle in the classical limit is given by the kinetic momentum [166],

$$\hat{\boldsymbol{\Pi}} = \hat{\boldsymbol{p}} - q_\psi \boldsymbol{A}. \tag{A.25}$$

The force is the time derivative of the kinetic momentum,[3]

$$\begin{aligned}
\frac{d\hat{\boldsymbol{\Pi}}}{dt} &= \frac{i}{\hbar}\left[\hat{H}, \hat{\boldsymbol{\Pi}}\right] + \frac{\partial \hat{\boldsymbol{\Pi}}}{\partial t} \\
&= \frac{i}{\hbar}\Big(c\gamma^0\left[\boldsymbol{\gamma}\cdot\hat{\boldsymbol{p}}, \hat{\boldsymbol{p}}\right] + m_\psi c^2\left[\gamma^0, \hat{\boldsymbol{p}}\right] + {q_\psi}^2 c\gamma^0\left[\boldsymbol{\gamma}\cdot\boldsymbol{A}, \boldsymbol{A}\right] - q_\psi m_\psi c^2\left[\gamma^0, \boldsymbol{A}\right] - {q_\psi}^2\left[V, \boldsymbol{A}\right] \\
&\qquad - q_\psi c\gamma^0\left[\boldsymbol{\gamma}\cdot\boldsymbol{A}, \hat{\boldsymbol{p}}\right] - q_\psi c\gamma^0\left[\boldsymbol{\gamma}\cdot\hat{\boldsymbol{p}}, \boldsymbol{A}\right] + q_\psi\left[V, \hat{\boldsymbol{p}}\right]\Big) - q_\psi\frac{\partial \boldsymbol{A}}{\partial t} \\
&= -q_\psi\nabla V - q_\psi\frac{\partial \boldsymbol{A}}{\partial t} + q_\psi c\gamma^0\boldsymbol{\gamma}\times(\nabla\times\boldsymbol{A}) \\
&= q_\psi\left(\boldsymbol{E} + \boldsymbol{v}\times\boldsymbol{B}\right).
\end{aligned}$$

This is the Lorentz Force.

---

[2]

$$\begin{aligned}
\left[\gamma^i\partial_i, \hat{\boldsymbol{r}}\right]\psi &= \gamma^i\partial_i\left(\hat{\boldsymbol{r}}\psi\right) - \hat{\boldsymbol{r}}\gamma^i\partial_i\psi \\
&= \gamma^i\left(\partial_i r^j \boldsymbol{e}_j\right)\psi \\
&= \gamma^i\boldsymbol{e}_i\psi = \boldsymbol{\gamma}\psi.
\end{aligned}$$

[3] Note that $[A^\mu, A^\nu] = [\gamma^\mu, A^\nu] = [\gamma^\mu, \hat{p}^\nu] = 0$. Also, it can be shown that

$$\begin{aligned}
\left[V, \hat{\boldsymbol{p}}\right] &= i\hbar\nabla V, \text{ and} \\
\left[\boldsymbol{\gamma}\cdot\boldsymbol{A}, \hat{\boldsymbol{p}}\right] + \left[\boldsymbol{\gamma}\cdot\hat{\boldsymbol{p}}, \boldsymbol{A}\right] &= i\hbar\boldsymbol{\gamma}\times(\nabla\times\boldsymbol{A}).
\end{aligned}$$

Appendix B

FIBER-BASED DETECTOR: ADDITIONAL CALCULATIONS

This appendix provides supporting information for Chapter 5. Section B.1 presents a model, with both signal and noise, for the phase difference $\Delta\Phi_{\mathrm{A}}$, which is effectively the output of the fiber-based detector. The analysis includes contributions from each major noise source and is general to both electron-coupled and photon-coupled scalar UDM. Section B.2 explains how the fibers' refractive indices may vary during the experiment, due to both scalar UDM and acoustic noise. Section B.3 provides estimates of properties of optical fibers that are necessary to estimate thermomechanical noise.

B.1 Derivation of output phase difference

In this section an expression for the output phase difference $\Delta\Phi_{\mathrm{A}}$ is derived for the detector displayed in Fig. 5.3 in terms of fluctuations due to both noise and the dark matter signal.

This analysis is general to DM-modulation of both electron mass m_e and the fine-structure constant α; fundamental constants will be generally represented by the variable $x \in \{m_e, \alpha\}$. However, it will be shown in Appendix B.2.1 that the detector is not sensitive to oscillation in m_e.

B.1.1 Definitions and model assumptions

Assumption 1: The analysis is restricted to low frequencies, defined by $f_{\mathrm{DM}} \ll {\tau_{0,i}}^{-1}$; i.e. this derivation holds when the DM Compton frequency is significantly below the inverse time delay of both fibers.

Assumption 2: All fluctuations are small:

$$\left\{\frac{\delta x}{x_0}, \frac{\delta L_i}{L_{0,i}}, \frac{\delta n_i}{n_{0,i}}, \frac{\delta \omega_{\rm L}}{\omega_{0,\rm L}}\right\} \ll 1.$$

Definition of ϵ-coefficients: Consider a quantity $w(v)$ with steady-state value $w_0 \equiv w(v_0)$ determined by the steady-state value of its parameter v_0.[1] Assuming small fluctuations ($\delta v \ll v_0$) in v about v_0, the fractional fluctuations of w can be expressed to first order as

$$\frac{\delta w}{w_0} \approx \epsilon_{wv} \frac{\delta v}{v_0}$$

where

$$\epsilon_{wv} \equiv \frac{v_0}{w_0} \frac{\partial w}{\partial v}\bigg|_{v=v_0}. \tag{B.1}$$

I also define the quantities $\Delta\epsilon_{wv} \equiv \epsilon_{wv,\rm A} - \epsilon_{wv,\rm B}$, which is the difference in ϵ-coefficient between Fiber A and Fiber B.

Effect	Expression
DM-index coupling	$\frac{\delta n_i}{n_{0,i}} = \epsilon_{nx,i} \frac{\delta x}{x_0}$
DM-length coupling	$\frac{\delta L_i}{L_{0,i}} = \epsilon_{Lx,i} \frac{\delta x}{x_0}$
Mechanical vibrations	$\frac{\delta L_i}{L_{0,i}} = h_i^{\rm acoustic}$
Vibrations (strain-optic)	$\frac{\delta n_i}{n_{0,i}} = \epsilon_{nL,i} h_i^{\rm acoustic}$
Optical dispersion	$\frac{\delta n_i}{n_{0,i}} = \epsilon_{n\omega_{\rm L},i} \frac{\delta \omega_{\rm L}}{\omega_{0,\rm L}}$
Fiber thermal noise	$\delta\phi_i = \delta\phi_i^{\rm thermal}$
Shot noise (at detector)	$\delta\phi_i = \delta\phi_i^{\rm shot}$

Table B.1: Summary of fluctuations included in the the derivation of $\Delta\Phi_{\rm A}$, due to both noise and DM. Each effect is expressed as a fluctuation in length, refractive index, or simply optical phase.

B.1.2 Fractional fluctuations of fiber refractive index and length

Fiber i's refractive index $n_i(x, \omega_{\rm L})$ depends on the fundamental constant x, the laser frequency $\omega_{\rm L}$ due to optical dispersion, and vibration-induced strains $h_i^{\rm acoustic}$ via the strain-optic effect:

$$\frac{\delta n_i}{n_{0,i}} = \epsilon_{nx,i} \frac{\delta x}{x_0} + \epsilon_{n\omega_{\rm L},i} \frac{\delta \omega_{\rm L}}{\omega_{0,\rm L}} + \epsilon_{nL,i} h_i^{\rm acoustic}. \tag{B.2}$$

[1] Here, the quantities w and v can represent any of the variables $\{x, L, n, \omega\}$.

Additionally, the fiber lengths depend on fundamental constant x, as the length of a solid is proportional to the Bohr radius, which will be affected by fluctuations in m_e or α ($a_\mathrm{B} \propto \left(m_e\alpha\right)^{-1}$) [67]. Thus, for both fibers $\epsilon_{Lx,i} = -1$.

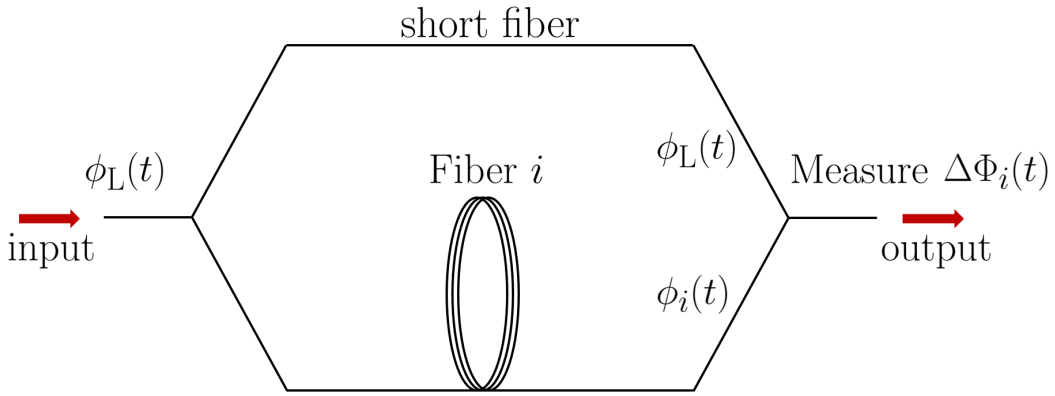

Figure B.1: Illustration of fiber interferometer, with relevant phases marked: The inferred output phase difference $\Delta\Phi_i(t) = \phi_\mathrm{L}(t) - \phi_i(t) + \delta\phi_i^\mathrm{shot}$ is determined by measuring the output optical power.

B.1.3 Optical phase at fiber output

If the phase of light entering a fiber is $\phi_\mathrm{L}(t)$, then the phase of light exiting the fiber will be equal to the input phase at an earlier time $\phi_i(t) = \phi_\mathrm{L}(t - \tau_i(t))$, where τ_i is the time it takes for an optical wavefront to traverse the entire length of the fiber. In the low frequency limit (Assumption 1) the time delay is simply related to the fiber's instantaneous optical path length $\tau_i(t) = n_i(t)L_i(t)/c$, and the output phase is

$$\phi_i(t) = \phi_\mathrm{L}(t) - \omega_\mathrm{L}(t)n_i(t)L_i(t)/c.$$

Including small fluctuations of the optical frequency, fiber index, and fiber length, the output optical phase can be written as

$$\phi_i \approx \phi_\mathrm{L} - \omega_{0,\mathrm{L}}\tau_{0,i}\left(1 + \frac{\delta n_i}{n_{0,i}} + \frac{\delta L_i}{L_{0,i}} + \frac{\delta\omega_\mathrm{L}}{\omega_{0,\mathrm{L}}}\right).$$

The explicit time dependence of each variable (t) has been omitted.

Accounting for both noise and DM-induced effects (Table B.1), the optical phase at the output of Fiber i is

$$\phi_i = \underbrace{\phi_{\mathrm{L}}}_{\substack{\text{input}\\ \text{laser}\\ \text{phase}}} + \underbrace{\delta\phi_i^{\text{thermal}}}_{\substack{\text{fiber thermal}\\ \text{fluctuations}}} - \omega_{0,\mathrm{L}}\tau_{0,i}\left(\underbrace{1}_{\text{DC term}} + \underbrace{\epsilon_{nx,i}\frac{\delta x}{x_0}}_{\substack{\text{DM-index}\\ \text{coupling}}} + \underbrace{\epsilon_{n\omega_{\mathrm{L}},i}\frac{\delta\omega_{\mathrm{L}}}{\omega_{0,\mathrm{L}}}}_{\substack{\text{optical}\\ \text{dispersion}}} + \underbrace{\epsilon_{Lx,i}\frac{\delta x}{x_0}}_{\substack{\text{DM-length}\\ \text{coupling}}} + \underbrace{\left(1+\epsilon_{nL,i}\right)h_i^{\text{acoustic}}}_{\substack{\text{mechanical}\\ \text{vibrations}}} + \underbrace{\frac{\delta\omega_{\mathrm{L}}}{\omega_{0,\mathrm{L}}}}_{\substack{\text{laser}\\ \text{frequency}\\ \text{fluctuations}}}\right) \tag{B.3}$$

B.1.4 Laser stabilized to Fiber B

As illustrated in Fig. 5.3, Fiber B acts as a delay line for stabilizing the laser. The inferred phase difference at Photodetector B is $\Delta\Phi_{\mathrm{B}} = \phi_{\mathrm{L}} - \phi_{\mathrm{B}} + \delta\phi_{\mathrm{B}}^{\text{shot}}$, where $\phi_{\mathrm{B}}^{\text{shot}}$ is the apparent phase imparted by shot noise. Stabilization can be achieved by tuning the laser's frequency using feedback based on the optical power measured by Photodetector B. For example, the laser's frequency can be tuned such that $\Delta\Phi_{\mathrm{B}} \bmod 2\pi = \pi/2$, maintaining quadrature bias between the recombining beams before Photodetector B. At quadrature bias, where the output optical power depends linearly on the phase difference Φ_{B}, it can be shown (using Eq. B.3) that the laser frequency fluctuations will be

$$\frac{\delta\omega_{\mathrm{L}}}{\omega_{0,\mathrm{L}}} = \left(1+\epsilon_{n\omega_{\mathrm{L}},\mathrm{B}}\right)^{-1}\left(\frac{\frac{\pi}{2} + \delta\phi_{\mathrm{B}}^{\text{thermal}} - \delta\phi_{\mathrm{B}}^{\text{shot}}}{\omega_{0,\mathrm{L}}\tau_{0,\mathrm{B}}} - \left(1+\epsilon_{nL,\mathrm{B}}\right)h_{\mathrm{B}}^{\text{acoustic}} - \left(\epsilon_{nx,\mathrm{B}} - 1\right)\frac{\delta x}{x_0}\right). \tag{B.4}$$

B.1.5 Detector output phase difference

The experimental observable in this experiment is the differential phase $\Delta\Phi_{\mathrm{A}}$ between the output of Fiber A and the interferometer's short arm, which is inferred from the measured optical power at Photodetector A. Here it is assumed that quadrature bias is maintained between the recombining beams before Photodetector A, which can be accomplished with a phase modulator that is driven by feedback from the power measured at Photodetector A. The DM signal would then be present in the feedback signal supplied to the modulator.

The phase difference $\Delta\Phi_{\rm A}$ can be calculated using Eqs. (B.3) and (B.4). Ignoring zero-frequency terms, $\Delta\Phi_{\rm A}$ is the sum of individual contributions from DM effects and each noise source

$$\Delta\Phi_{\rm A} = \Delta\Phi_{\rm A}^{\rm DM} + \Delta\Phi_{\rm A}^{\rm thermal} + \Delta\Phi_{\rm A}^{\rm acoustic} + \Delta\Phi_{\rm A}^{\rm shot}.$$

Noting that $\epsilon_{nx} \sim \epsilon_{n\omega_{\rm L}} \approx 10^{-2}$ (see Appendix B.2) and ignoring higher-order terms, it can be shown that

$$\Delta\Phi_{\rm A}^{\rm DM} \approx \omega_{0,{\rm L}}\tau_0 \left(\Delta\epsilon_{nx} + \Delta\epsilon_{n\omega_{\rm L}}\right) \frac{\delta x}{x_0} \tag{B.5}$$

$$\Delta\Phi_{\rm A}^{\rm acoustic} \approx \omega_{0,{\rm L}}\tau_0 \left[\left(1+\epsilon_{nL,{\rm A}}\right) h_{\rm A}^{\rm acoustic} - \left(1+\Delta\epsilon_{n\omega_{\rm L}} + \epsilon_{nL,{\rm B}}\right) h_{\rm B}^{\rm acoustic}\right] \tag{B.6}$$

$$\Delta\Phi_{\rm A}^{\rm thermal} \approx -\delta\phi_{\rm A}^{\rm thermal} + \delta\phi_{\rm B}^{\rm thermal} \tag{B.7}$$

$$\Delta\Phi_{\rm A}^{\rm shot} \approx \delta\phi_{\rm A}^{\rm shot} - \delta\phi_{\rm B}^{\rm shot}, \tag{B.8}$$

where both fibers are assumed to have equal optical path lengths $\tau_{0,i} \equiv \tau_0$ for simplicity.

B.2 Refractive index effects

B.2.1 DM-coupling to refractive index

The dependence of an optical material's refractive index on fundamental constants such as α and m_e can be estimated using a Lorentz model[2] for the atoms/molecules [71, 135].

This analysis primarily follows the treatments in Refs. [71, 173] for the classical Lorentz model. For small oscillations, the binding force of an electron to a molecule can be approximated as harmonic [174]. Given an external electric field $\boldsymbol{E}$, the equation of motion for the electron's displacement $\boldsymbol{z}$ from equilibrium is

$$\ddot{\boldsymbol{z}} + \gamma\dot{\boldsymbol{z}} + {\omega_0}^2\boldsymbol{z} = \frac{e}{m_e}\boldsymbol{E}, \tag{B.9}$$

where a velocity-damping term is assumed [173, 174]. The Fourier transform of the dipole moment $\tilde{\boldsymbol{p}} = e\tilde{\boldsymbol{z}}$ is then related to that of the driving field $\tilde{\boldsymbol{E}}$ as

$$\tilde{\boldsymbol{p}} = \frac{e^2}{m_e}\left({\omega_0}^2 - \omega^2 - i\omega\gamma\right)^{-1}\tilde{\boldsymbol{E}}. \tag{B.10}$$

[2] The Lorentz model approximation loses accuracy for a variety of circumstances, such as for strong optical fields or dielectrics with chemical bonding [172].

Given a volume of atoms/molecules with number density N, the polarization is $\boldsymbol{P} = N\boldsymbol{p}$ [173]. The Fourier transform of the polarization is related to that of the driving electric field as $\tilde{\boldsymbol{P}} = \epsilon_0 \chi \tilde{\boldsymbol{E}}$, where the electric susceptibility is then

$$\chi = \frac{Ne^2}{\epsilon_0 m_e} \left({\omega_0}^2 - \omega^2 - i\omega\gamma \right)^{-1}. \tag{B.11}$$

For a dilute gas, the refractive index n can be simply related to the susceptibility as $n^2 - 1 = \chi$ [173]. However, for a non-dilute medium (such as a solid) the local electric field is not simply equal to the external field $\boldsymbol{E}$ [71, 173], and the relationship between the refractive index n and the susceptibility χ presented in Eq. (B.11) is

$$\frac{n^2 - 1}{n^2 + 2} = \frac{\chi}{3}. \tag{B.12}$$

The analysis can be generalized to account for multiple electron and phonon modes by considering the total electric susceptibility as a sum of the susceptibility of each mode: $\chi \to \sum_k \chi_k$ [71]. Far from the resonances, the damping terms can be neglected [71, 174], such that each mode's susceptibility takes the form

$$\chi_k = \frac{e^2}{\epsilon_0} \frac{N_k}{M_k} \frac{f_k}{{\omega_k}^2 - \omega^2}, \tag{B.13}$$

where N_k is the effective number density, M_k is the reduced effective mass, f_k is the oscillator strength, and ω_k is the resonance frequency [71]. The number density is inversely proportional to the atomic/molecular volume [determined by the Bohr radius $a_\mathrm{B} \propto (\alpha m_e)^{-1}$], such that $N_k \propto (\alpha m_e)^3$. For electron modes, $M_k = m_e$; for phonon modes, M_k is independent of α, m_e, and ω [71]. The oscillator strengths f_k are also approximately independent of α, m_e, and ω [71]. Noting that $e^2/\epsilon_0 = 4\pi\hbar c\alpha$ it can be shown that, for both electron and phonon modes,

$$\chi_k \propto \left(1 - \omega^2 {\omega_k}^{-2} \right)^{-1}. \tag{B.14}$$

The dependence on fundamental constants α and m_e is entirely accounted for by the resonance frequencies ω_k. For phonon modes $\omega_k \propto {m_e}^{3/2}\alpha^2$; for electron modes $\omega_k \propto m_e\alpha^2$ [71].

If the laser frequency is assumed to be in a range where it is reasonable to consider either only phonon modes or only electron modes (i.e. relationship between ω_k and the

fundamental constants is independent of mode number k), it can be shown from Eqs. B.12 and B.14 that

$$\frac{x}{n}\frac{\partial n}{\partial x} = -\left(\frac{x}{\omega_k}\frac{\partial \omega_k}{\partial x}\right)\left(\frac{\omega}{n}\frac{\partial n}{\partial \omega}\right) \tag{B.15}$$

where $x \in \{\alpha, m_e\}$. Equation (B.15) allows one to calculate the response of a material's refractive index to variations of fundamental constants using the material's dispersion, which can be measured experimentally.

For variations in α,

$$\frac{\alpha}{n}\frac{\partial n}{\partial \alpha} = -2\left(\frac{\omega}{n}\frac{\partial n}{\partial \omega}\right), \tag{B.16}$$

regardless of the type of mode. However, the refractive index's dependence on m_e depends on which mode type dominates:

$$\frac{m_e}{n}\frac{\partial n}{\partial m_e} = \begin{cases} -\left(\frac{\omega}{n}\frac{\partial n}{\partial \omega}\right) & \text{electron modes} \\ -\frac{3}{2}\left(\frac{\omega}{n}\frac{\partial n}{\partial \omega}\right) & \text{phonon modes} \end{cases} \tag{B.17}$$

Following Ref. [135], it is assumed that electron modes dominate the dispersion of fused silica, in which case

$$\epsilon_{n\alpha,\text{silica}} = -2\epsilon_{n\omega_\text{L},\text{silica}} \tag{B.18}$$

$$\epsilon_{nm_e,\text{silica}} = -\epsilon_{n\omega_\text{L},\text{silica}}. \tag{B.19}$$

Optical dispersion and, therefore, DM-coupling to the refractive index of air, are significantly less than that of silica, so it is generally assumed that $\{\epsilon_{nx,\text{air}}, \epsilon_{n\omega_\text{L},\text{air}}\} = 0$.

The DM signal (Eq. B.5) is proportional to $\epsilon_{nx,\text{silica}} + \epsilon_{n\omega_\text{L},\text{silica}}$. Evidently, from Eqs. (B.18) and (B.19), the detector is only sensitive to DM-induced oscillations in α, not m_e.[3]

From the three-term Sellmeier equation for fused silica [175], $\epsilon_{n\omega_\text{L},\text{silica}} = 0.013$.

[3] $\epsilon_{nm_e,\text{silica}} + \epsilon_{n\omega_\text{L},\text{silica}} = (-\epsilon_{n\omega_\text{L},\text{silica}}) + \epsilon_{n\omega_\text{L},\text{silica}} = 0$. A more detailed analysis (beyond the simple Lorentz model used here) of the refractive index of silica may affect this result.

Quantity	Variable [Units]	Solid Core	Hollow Core
refractive index	n_0 [-]	1.47 [1]	1
optical loss	γ [m^{-1}]	1.8×10^{-5} [1]	2.8×10^{-5} [2]
optical dispersion	$\epsilon_{n\omega_L}$ [-]	0.013 [175]	0
stress-optic effect	ϵ_{nL} [-]	−0.17 [176]	0
mechanical loss tangent	ξ [-]	10^{-2} [142, 177]	10^{-2}*
diameter of coating	d_{coat} [μm]	242 [1]	302*
diameter of cladding	d_{clad} [μm]	125 [1]	185 [138]
diameter of photonic crystal region	d_{pc} [μm]	0	70 [138]
total cross-sectional area	A [μm^2]	4.6×10^4	6.8×10^4
Young's modulus	E [GPa]	20	25

Table B.2: Parameters used for optical fibers with coatings at room temperature. The solid core fiber is assumed to be SMF28 [1], and the hollow core fiber is assumed to be nested antiresonant nodeless fiber (NANF) [2]. See Appendix B.3 for information on how the parameters are affected by removing the fiber coatings and operating at cryogenic temperatures. *The loss tangent and coating thickness for hollow core fiber is assumed equal to those of SMF28.

B.2.2 Strain-optic effect

Mechanical vibrations will strain the fibers. In the solid core fiber, this will lead to a change in the refractive index via the strain-optic effect

$$\frac{\delta n}{n_0} = \epsilon_{nL} h^{\text{acoustic}}. \tag{B.20}$$

From the analysis in Ref. [176], which considers a linear strain along a single mode fiber, it can be shown that

$$\epsilon_{nL,\text{solid}} \approx -0.17. \tag{B.21}$$

The strain-optic effect then has a greater impact than optical dispersion $\left(\left|\Delta\epsilon_{nL}\right| > \left|\Delta\epsilon_{n\omega_L}\right|\right)$ on the acoustic phase noise given by Eq. (5.10).

B.3 Mechanical properties of fibers

Fiber thermomechanical noise, as discussed in Section 5.2.1, depends on the physical properties of the fibers: the mechanical loss tangent ξ, the effective Young's modulus E, and the cross-sectional area A.

Key parameters for the fibers considered in this work are summarized in Table B.2. While the physical properties ξ and E have not been measured specifically for SMF28 fibers, the estimates found in Table B.2 have been shown to reliably predict thermomechanical noise in SMF28 fibers [142] via Eq. (5.5).

The quoted value for the loss tangent $\xi = 10^{-2}$ comes from measurements of a solid core fiber at kHz frequencies [177]. For simplicity, $\xi = 10^{-2}$ is also assumed for the lower frequencies considered in this work, for both solid and hollow core fibers. Dong et al [142] have characterized thermal noise in SMF28 fibers down to sub-Hz frequencies assuming $\xi = 10^{-2}$, suggesting that this is a reasonable assumption.

The Young's modulus (E) is approximated for a fiber by a weighted average, over cross-sectional area, of the Young's moduli of each material [177]:

$$E \approx \frac{A_{\text{coat}} E_{\text{coat}} + A_{\text{clad}} E_{\text{clad}}}{A}. \tag{B.22}$$

The values $E_{\text{clad}} = 66.1$ GPa for a silica fiber and $E_{\text{coat}} = 3.3$ GPa for the polymer coating (assuming acrylate) are used, based on measurements at kHz frequencies [177]. The Young's moduli are assumed to be frequency-independent. The values for E in Table B.2 are calculated from Eq. (B.22) with the following cross-sectional areas

$$\begin{aligned} A &\approx \frac{\pi}{4}\left({d_{\text{coat}}}^2 - {d_{\text{pc}}}^2\right) \\ A_{\text{coat}} &= \frac{\pi}{4}\left({d_{\text{coat}}}^2 - {d_{\text{clad}}}^2\right) \\ A_{\text{clad}} &\approx \frac{\pi}{4}\left({d_{\text{clad}}}^2 - {d_{\text{pc}}}^2\right), \end{aligned}$$

which approximate the hollow and photonic crystal regions to be empty space.

B.3.1 Bare fibers

The fluctuation-dissipation theorem predicts that thermomechanical noise increases with mechanical dissipation. Thus, decreasing a fiber's mechanical loss tangent ξ will lower the thermomechanical noise floor, improving the experiment's sensitivity.

Much of the mechanical loss in optical fibers likely comes from the polymer coatings. Fibers with thinner coatings will experience less dissipation. Dong et al. [142] have shown

that the thermomechanical noise floor is lower in fibers with thinner coatings. However, the study is insufficient to draw a quantitative relationship between ξ and coating thickness.

It has been shown that fused silica optical fibers with a polymer-coating have a loss tangent $\xi \approx 10^{-2}$ [142, 177]. However, bulk fused silica can potentially achieve $\xi \approx 10^{-8}$ at room temperature [178]. Fused silica fibers are often used as suspension wires for test masses in gravitational wave detectors. In this context, mechanical dissipation in the violin modes (transverse oscillations) of bare fibers at room temperature is typically around $\xi \approx 10^{-7} - 10^{-6}$ [179, 180, 181]. Noting that mechanical loss in a spooled optical fiber will likely differ from that of bulk silica or violin modes in silica suspensions under tension, a value of $\xi = 10^{-6}$ is assumed for bare fibers at room temperature. By setting $d_{\text{coat}} = d_{\text{clad}}$ the fibers' cross-sectional areas and effective Young's moduli are recalculated, with all other parameters in Table B.2 unchanged.

B.3.2 Low-temperature effects

Measurements of the temperature dependence of the Young's modulus of fused silica [182] and the refractive index of fused silica fibers [183] suggest that n_0 and E_{clad} can be assumed constant with respect to temperature without appreciably affecting the estimates in Fig. 5.2. However, the mechanical loss tangent ξ of fused silica at kHz-MHz frequencies has been shown to exhibit a strong temperature dependence, with a maximum of $\xi \sim 10^{-3}$ at around 30-50 K [178, 184] before beginning to decrease with lowering temperature beyond that, although it is unclear how well this translates to fibers. In this work, it is considered to use thinner of fiber coatings as a way to reduce the loss tangent, approaching that of fused silica. It is assumed that $\xi = 10^{-3}$ for cryogenic (10 mK) bare fibers, based on measurements in Ref. [185].

At low temperatures ($\sim$ 200 K), the acrylate coatings transition from a rubbery state to a stiffer, glassy state with a Young's modulus $E_{\text{coat}} \approx 40$ GPa [186], and the effective Young's modulus has been adjusted for coated fibers at 10 mK accordingly with Eq. (B.22). However, due to the absence of data on mechanical dissipation in optical fibers at low temperatures,

$\xi = 10^{-2}$ is assumed for coated fibers at all temperatures, and it should be noted that the loss tangent is likely to decrease as the coatings stiffen at cryogenic temperatures.

Further study of optical fibers at low temperatures and with thinner coatings is necessary to improve upon these estimates of ξ.

Appendix C

PERMISSIONS TO USE COPYRIGHTED MATERIAL

This appendix includes permissions to use copyrighted material.

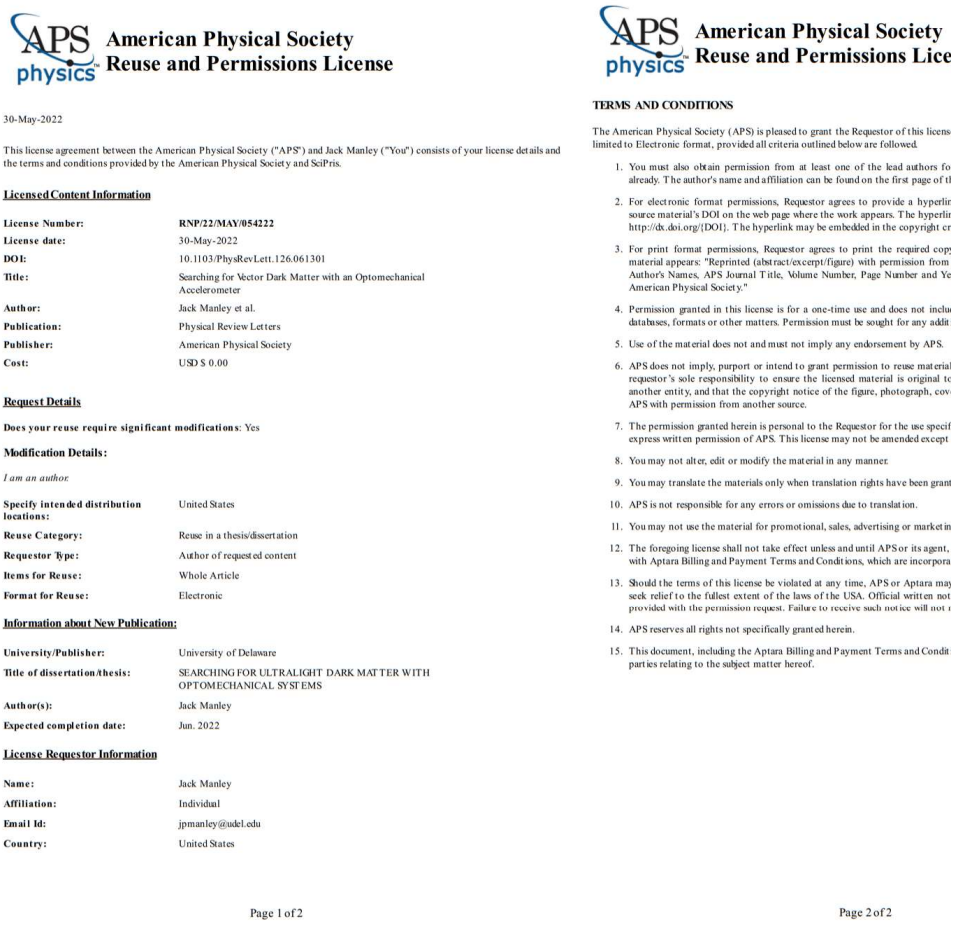

American Physical Society
Reuse and Permissions License

30-May-2022

This license agreement between the American Physical Society ("APS") and Jack Manley ("You") consists of your license details and the terms and conditions provided by the American Physical Society and SciPris.

Licensed Content Information

License Number:	**RNP/22/MAY/054222**
License date:	30-May-2022
DOI:	10.1103/PhysRevLett.126.061301
Title:	Searching for Vector Dark Matter with an Optomechanical Accelerometer
Author:	Jack Manley et al.
Publication:	Physical Review Letters
Publisher:	American Physical Society
Cost:	USD $ 0.00

Request Details

Does your reuse require significant modifications: Yes

Modification Details:

I am an author.

Specify intended distribution locations:	United States
Reuse Category:	Reuse in a thesis/dissertation
Requestor Type:	Author of requested content
Items for Reuse:	Whole Article
Format for Reuse:	Electronic

Information about New Publication:

University/Publisher:	University of Delaware
Title of dissertation/thesis:	SEARCHING FOR ULTRALIGHT DARK MATTER WITH OPTOMECHANICAL SYSTEMS
Author(s):	Jack Manley
Expected completion date:	Jun. 2022

License Requestor Information

Name:	Jack Manley
Affiliation:	Individual
Email Id:	jpmanley@udel.edu
Country:	United States

Page 1 of 2

American Physical Society
Reuse and Permissions Lice

TERMS AND CONDITIONS

The American Physical Society (APS) is pleased to grant the Requestor of this licens limited to Electronic format, provided all criteria outlined below are followed.

1. You must also obtain permission from at least one of the lead authors fo already. The author's name and affiliation can be found on the first page of th
2. For electronic format permissions, Requestor agrees to provide a hyperlir source material's DOI on the web page where the work appears. The hyperlir http://dx.doi.org/{DOI}. The hyperlink may be embedded in the copyright cr
3. For print format permissions, Requestor agrees to print the required copy material appears: "Reprinted (abstract/excerpt/figure) with permission from Author's Names, APS Journal Title, Volume Number, Page Number and Ye American Physical Society."
4. Permission granted in this license is for a one-time use and does not inclu databases, formats or other matters. Permission must be sought for any addit
5. Use of the material does not and must not imply any endorsement by APS.
6. APS does not imply, purport or intend to grant permission to reuse material requestor's sole responsibility to ensure the licensed material is original to another entity, and that the copyright notice of the figure, photograph, cov APS with permission from another source.
7. The permission granted herein is personal to the Requestor for the use specif express written permission of APS. This license may not be amended except
8. You may not alter, edit or modify the material in any manner.
9. You may translate the materials only when translation rights have been grant
10. APS is not responsible for any errors or omissions due to translation.
11. You may not use the material for promotional, sales, advertising or market in
12. The foregoing license shall not take effect unless and until APS or its agent, with Aptara Billing and Payment Terms and Conditions, which are incorpora
13. Should the terms of this license be violated at any time, APS or Aptara may seek relief to the fullest extent of the laws of the USA. Official written not provided with the permission request. Failure to receive such notice will not
14. APS reserves all rights not specifically granted herein.
15. This document, including the Aptara Billing and Payment Terms and Condit parties relating to the subject matter hereof.

Page 2 of 2

Figure C.1: Permission to use material from Ref. [42]. DOI: 10.1103/PhysRevLett.126.061301

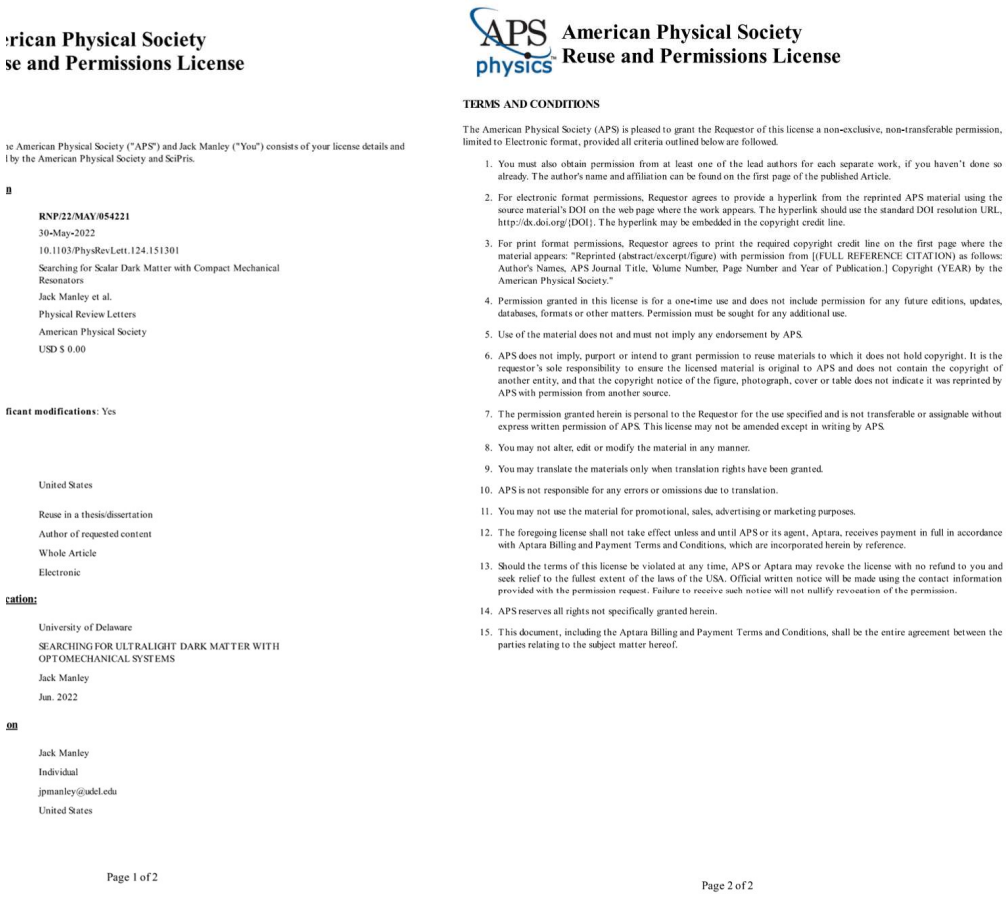

erican Physical Society
se and Permissions License

e American Physical Society ("APS") and Jack Manley ("You") consists of your license details and
l by the American Physical Society and SciPris.

n

RNP/22/MAY/054221
30-May-2022
10.1103/PhysRevLett.124.151301
Searching for Scalar Dark Matter with Compact Mechanical Resonators
Jack Manley et al.
Physical Review Letters
American Physical Society
USD $ 0.00

ficant modifications: Yes

United States
Reuse in a thesis/dissertation
Author of requested content
Whole Article
Electronic

cation:

University of Delaware
SEARCHING FOR ULTRALIGHT DARK MATTER WITH OPTOMECHANICAL SYSTEMS
Jack Manley
Jun. 2022

on

Jack Manley
Individual
jpmanley@udel.edu
United States

Page 1 of 2

American Physical Society
Reuse and Permissions License

TERMS AND CONDITIONS

The American Physical Society (APS) is pleased to grant the Requestor of this license a non-exclusive, non-transferable permission, limited to Electronic format, provided all criteria outlined below are followed.

1. You must also obtain permission from at least one of the lead authors for each separate work, if you haven't done so already. The author's name and affiliation can be found on the first page of the published Article.
2. For electronic format permissions, Requestor agrees to provide a hyperlink from the reprinted APS material using the source material's DOI on the web page where the work appears. The hyperlink should use the standard DOI resolution URL, http://dx.doi.org/{DOI}. The hyperlink may be embedded in the copyright credit line.
3. For print format permissions, Requestor agrees to print the required copyright credit line on the first page where the material appears: "Reprinted (abstract/excerpt/figure) with permission from [(FULL REFERENCE CITATION) as follows: Author's Names, APS Journal Title, Volume Number, Page Number and Year of Publication.] Copyright (YEAR) by the American Physical Society."
4. Permission granted in this license is for a one-time use and does not include permission for any future editions, updates, databases, formats or other matters. Permission must be sought for any additional use.
5. Use of the material does not and must not imply any endorsement by APS.
6. APS does not imply, purport or intend to grant permission to reuse materials to which it does not hold copyright. It is the requestor's sole responsibility to ensure the licensed material is original to APS and does not contain the copyright of another entity, and that the copyright notice of the figure, photograph, cover or table does not indicate it was reprinted by APS with permission from another source.
7. The permission granted herein is personal to the Requestor for the use specified and is not transferable or assignable without express written permission of APS. This license may not be amended except in writing by APS.
8. You may not alter, edit or modify the material in any manner.
9. You may translate the materials only when translation rights have been granted.
10. APS is not responsible for any errors or omissions due to translation.
11. You may not use the material for promotional, sales, advertising or marketing purposes.
12. The foregoing license shall not take effect unless and until APS or its agent, Aptara, receives payment in full in accordance with Aptara Billing and Payment Terms and Conditions, which are incorporated herein by reference.
13. Should the terms of this license be violated at any time, APS or Aptara may revoke the license with no refund to you and seek relief to the fullest extent of the laws of the USA. Official written notice will be made using the contact information provided with the permission request. Failure to receive such notice will not nullify revocation of the permission.
14. APS reserves all rights not specifically granted herein.
15. This document, including the Aptara Billing and Payment Terms and Conditions, shall be the entire agreement between the parties relating to the subject matter hereof.

Page 2 of 2

Figure C.2: Permission to use material from Ref. [33]. DOI: 10.1103/PhysRevLett.124.151301